Vortex-induced Synchronous Pressure Pulsations in the Draft-tubes of Hydraulic Turbines

水力タービンのドラフトチューブにおける渦誘起同期圧力脈動

December 2021

Mohammadhossein KHOZAEIRAVARI

コザエイラバリ　モハンマドホセイン

Vortex-induced Synchronous Pressure Pulsations in the Draft-tubes of Hydraulic Turbines

水力タービンのドラフトチューブにおける渦誘起同期圧力脈動

December 2021

Waseda University
Graduate School of Fundamental Science and Engineering,
Department of Applied Mechanics and Aerospace Engineering,
Research on Fluid Engineering

Mohammadhossein KHOZAEIRAVARI
コザエイラバリ　モハンマドホセイン

From life's school of war:
what does not kill me makes me stronger.

- Friedrich Nietzsche

Acknowledgements

I would first like to acknowledge my beloved wife, Majdeh, who dedicated her life to our family's prosperity. She supported me during the toughest days of my life. My research would have been impossible without her exceptional aid and support.

I would like to thank my supervisor, Professor Kazuyoshi Miyagawa, whose support was invaluable in my career. His insightful feedback pushed me to sharpen my thinking and brought my work to a higher level. I would also like to thank my co-supervisors – Professor Tsujimoto, Professor Ohta, and Professor Sato – for their extensive support to improve this thesis contents.

I would like to acknowledge my colleagues at Waseda University. I would particularly like to appreciate Dr. Arthur Favrel for his precious advice and encouragement during my research. I would thank Mr. Gabriel Taillon who stood beside me as a friend the whole time. I would thank Mr. Tsutaya and Mr. Nakajima, the master students who supported me to conduct my experiments. I would like to express my gratitude to Mr. Masuko, Mr. Watanabe (Meidensha Ltd.) and Mr. Yamaguchi, Mr. Kishor (EAML Engineering Co.) who provided the model Francis turbine for this thesis.

Last but not the least, I would like to thank my parents for their dedication and kindness. I could have never reached to this point without their constant and unwavering support.

M. H. Khozaei

Tokyo, Japan
September 2021

Abstract

In the context of installed capacity of renewable energy sources, the extensive necessity to provide grid flexibility ensued to enormous amount of attention in recent years to develop hydropower plants featuring flexible operating capabilities to provide primary and secondary frequency control to the electrical grid. Francis turbines which roughly represents 60% of the installed hydropower capacity in the world can play an additional role by contributing to the stabilization of the electrical grid. However, this requires an extension of their operating range from very low load to high load to adjust their output power. Operations of Francis turbines in off-design conditions are accompanied with undesirable phenomena, such as cavitation, precessing vortex core (PVC), draft-tube cavitation surge, and so forth, inducing pressure fluctuations either in the machine or in the entire hydraulic system, and power swings. In this context, the current thesis focuses on investigation of physics of three phenomena that induce synchronous pressure pulsations in the draft-tubes of hydraulic turbines and may induce instabilities during off-design operating conditions. It is highlighted in the first chapter of the thesis that synchronous pressure pulsations play an important role in destabilizing the hydraulic system, considering that they can propagate everywhere in the system and induce resonance if their frequencies coincide with one of the natural frequencies of the hydraulic circuits.

In the first part of the thesis (chapter 2) an oscillatory behavior of the vortex breakdown is identified using the results of pressure measurements in a simplified draft-tube. It is observed that the oscillatory behavior of the vortex breakdown generates low-frequency synchronous pressure pulsations which can be observed everywhere in the entire hydraulic system. Numerical simulations are then carried out to understand the flow field behavior near the breakdown location. It is noticed that the vortex breakdown location and the volume of the reverse flow region downstream of the breakdown fluctuate with the same low frequency as the synchronous pressure pulsations. It is confirmed later that a shear layer forms around the vortex center at the location of breakdown which stretches the vortex center in a circumferential direction. This generates intermittent vortical structures downstream of the breakdown location.

Cavitation surge characteristics under different swirl intensities in a simplified draft-tube are studied within the second part of the thesis (chapter 3). Pressure measurements along with high-speed visualization of cavity volume are conducted for a wide range of operating conditions (for a variety of swirl intensities, flowrates, and cavitation numbers). The 1st natural frequency of the draft-tube is identified by using the results of pressure measurements and high-speed visualizations; and it is observed that the 1st natural frequency of the draft-tube decreases with

decreasing the cavitation number. The low-frequency synchronous pressure pulsations due to oscillatory behavior of the vortex breakdown (which is introduced in chapter 2) are identified for all operating conditions. It is observed that cavitation surge starts when the 1st natural frequency of the draft-tube coincides with the frequency of the abovementioned synchronous pressure pulsations. The operating conditions are divided into two stable and unstable modes. A transition between the stable and unstable modes of the draft-tube is identified. Several correlations between the 1st natural frequency of the draft-tube and cavitation number and cavity void fraction are established. A 1D model is employed to predict the wave speed and the 1st natural frequency of the draft-tube. The results of 1D modelling are compared with the results of pressure measurements and high-speed visualizations of the cavity volume at the end.

In the third part of the thesis (chapter 4), another type of synchronous pressure pulsation is identified in an elbow-type draft-tube of a Francis turbine. The model test results of a Francis turbine are used to find the no-swirl operating conditions. A novel methodology based on the definition of the swirl number is introduced to find the iso-swirl lines on the operating Hill chart of the turbine. The part-load operating points of the turbine are divided into three regimes (namely, a. upper part-load, b. part-load, and c. deep part-load) by using the frequency of the pressure pulsations in the draft-tube. Low-frequency synchronous pressure pulsations are identified in the draft-tube of the machine during its deep part-load operation. By using the results of unsteady-state CFD simulations, it is confirmed that generation of a twin vortex rope in the elbow is responsible for generation of the low-frequency pressure pulsations in the draft-tube. It is suggested that the identified synchronous pressure pulsations during deep part-load operation of the turbine may cause cavitation surge instability in presence of cavitation in the draft-tube.

This thesis aims at investigating the flow field in the draft-tube of hydraulic turbines to understand the physics of three phenomena which induce synchronous pressure pulsations in the hydraulic system. In the first part of the thesis, the source of synchronous pressure pulsations in a simplified draft-tube is identified in presence of an axisymmetric vortex. It is later seen that the identified synchronous pressure pulsations act as an excitation source for onset of resonance and cavitation surge instability in the draft-tube. The flow field in an elbow-type draft-tube of a Francis turbine is investigated in the next part of the thesis; and another type of synchronous pressure pulsation is identified in the draft-tube of the Francis turbine during its deep part-load operation which may also induce instabilities in presence of cavitation. The presented results in the current thesis can be further used by design engineers to extend operating range of hydraulic turbines by avoiding the studied instabilities within this thesis in order to achieve a better stabilization in the electrical grids.

Contents

List of figures

List of tables

Nomenclature

Latin Letters

A	Area
a	Wave speed
$a_{equ.}$	Equivalent wave speed
C_c	Cavitation compliance
$C_{equ.}$	Equivalent compliance
C_p	Pressure excess ratio
C_{pipe}	Pipe compliance
R_{RLC}	RLC capacitance
C_{water}	Water compliance
Co.	Courant number
D	Diameter / swirler diameter
D_{throat}	Throat diameter
E	Specific hydraulic energy
f	Frequency
$f_{inst.}$	Instantaneous frequency
f_n	Natural frequency
f_{PVC}	Frequency of precessing vortex core (PVC)
f_{Runner}	Runner frequency
g	Gravitational acceleration
h	Head
i	Number of pressure signals on a certain cross-section
$\mathbf{J}$	Velocity gradient tensor
k	Swirl characteristic parameter
L	Length
L_{RLC}	RLC inductance
n	Rotational speed
n_{ED}	Speed factor
n_{ED}^*	Dimensionless speed factor
P	Pressure / mean pressure
P_{atm}	Atmospheric pressure
P_{throat}	Pressure in the throat
P_v	Vapor pressure
P^*	Pressure coefficient
Q	Flowrate / discharge
Q_{ED}	Discharge factor
Q_{ED}^*	Dimensionless discharge factor
Q_{ED}^0	Discharge factor corresponding to the no-swirl condition
Q_{ED}^{BEP}	Discharge factor corresponding to the BEP
Q_{ED}^{0*}	Dimensionless discharge factor corresponding to the no-swirl condition
r	Radial direction
R	Radius
Re	Reynolds number

R_{RLC}	RLC resistance
R_{throat}	Throat radius
r	Radial location
r^*	Dimensionless radial location
S	Swirl number
$\bar{S}$	Analytical swirl number
$\mathbf{S}$	Strain rate tensor
Str.	Strouhal number
$\text{Str.}_{\text{inst.}}$	Instantaneous Strouhal number
t	Timestep
U	Circumferential velocity
$u_{particle}$	Mean velocity of fluid particles
V_c	Cavity volume
V_m	Meridional component of velocity
$V_{m,th.}$	Mean meridional velocity in the upstream pipe
$V_{m,up.}$	Mean meridional velocity in the throat
V_t	Tangential component of velocity
$\vec{V}$	Velocity vector
x	Location along x-axis
x^*	Dimensionless location along x-axis
y	Location along y-axis
y^*	Dimensionless location along y-axis
z^*	Dimensionless axial location

Greek Letters

β	Cavity void fraction
β_2	Blade angle
Γ_1	Gamma-1 scaler
δ	Eigen value
Δt	Timestep size
$\Delta t_{inst.}$	Period of fluctuations
Δx	Grid-cell size
ΔP^*	Pressure drop coefficient
θ	Angular location
λ	Eigenvalues of $\mathbf{S}^2+\mathbf{\Omega}^2$
μ	Dynamic viscosity
μ_s	Stability criterion of the system
ν	Kinematic viscosity
ρ	Density
σ	Cavitation number
τ	Free-motion time constant
χ	Mass flow gain factor
ω	Angular velocity
$\vec{\omega}$	Vorticity vector
$\mathbf{\Omega}$	Spin tensor

1. Introduction

1.1. Research context

Climate concerns have led to new policies promoting the development of new and renewable energy sources, e.g., wind and solar, that depends on the weather conditions. Their production is therefore intermittent and unpredictable, putting at risk the electricity grid stability. In a context of increasing installed capacity of renewable energy sources, the extensive necessity to provide grid flexibility ensued to enormous amount of attention in recent years to develop hydropower plants featuring flexible operating capabilities to provide primary and secondary frequency control to the electrical grid.

Francis turbines, that roughly represents 60% of the installed hydropower capacity in the world, have been widely used as baseload generating units for the electrical grid. In the new context of increasing electricity production by intermittent sources of renewable energy, Francis turbines can play an additional role by contributing to the stabilization of the electrical grid. However, this requires an extension of their operating range from very low load to high load to adjust their output power. Operations of Francis turbines in off-design conditions are accompanied with undesirable phenomena, such as cavitation, precessing vortex core (PVC), draft-tube cavitation surge, and so forth [1], inducing pressure fluctuations either in the machine or in the entire hydraulic system, and power swings.

Francis turbines are designed for a given operating point, called the Best Efficiency Point (BEP), where they feature highest efficiency and nearly axial flow at the runner outlet. The velocity triangle at runner outlet during BEP is presented in Figure 1.1. In off-design conditions, however, the flow velocity field at the runner outlet features a tangential velocity component in addition to the meridional component, Figure 1.2. As a result, a vortex and an inhomogeneous pressure field are formed at the runner outlet in the draft-tube.

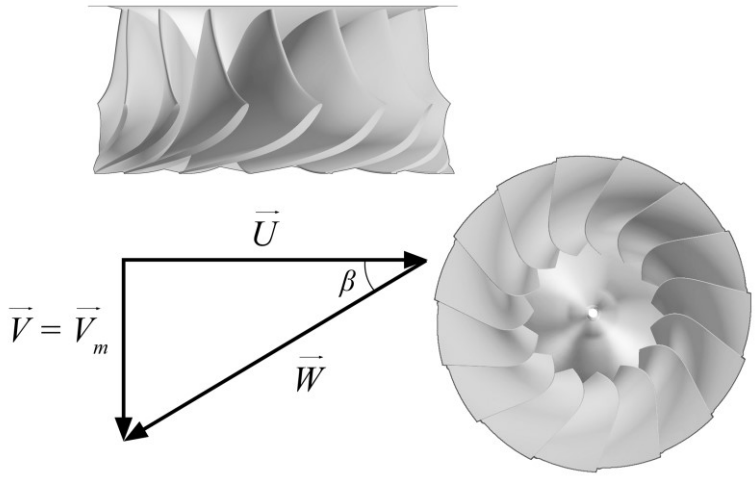

Figure 1.1. Velocity tringle at the outlet of a Francis turbine runner at BEP condition

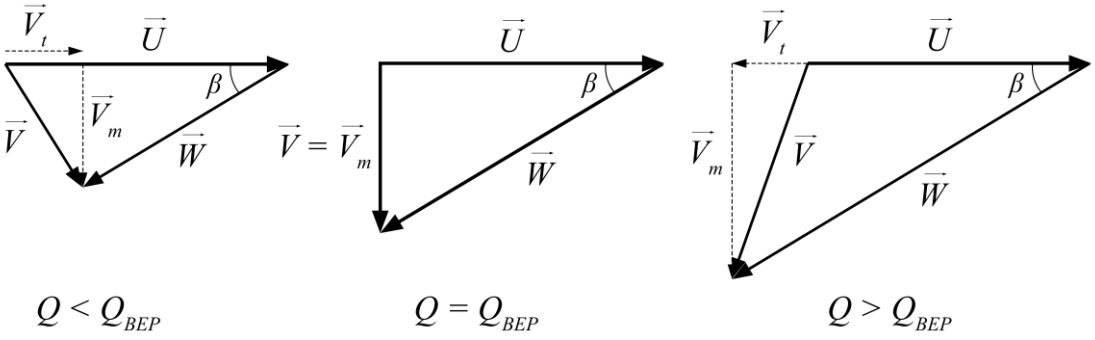

Figure 1.2. Velocity triangles at the runner outlet for a. part-load, b. BEP, and c. high-load conditions

In the case of low-pressure condition in the draft-tube, cavitation appears in the vortex core, forming the so-called cavitation vortex rope. The operating conditions of the machine directly affect the intensity of the residual swirl leaving the runner and therefore the shape and behavior of the cavitation vortex rope.

At high load conditions (i.e., with a flow rate higher than the value at the design point), a nearly axisymmetric vortex rope is formed along the draft-tube. The so-called draft-tube cavitation surge phenomenon, which corresponds to a self-excited behavior of the cavitation vortex rope, may occur and generate high-amplitude pressure oscillations in the entire hydraulic system and power swings [2-7]. Operations at part-load conditions (i.e., with a flow rate lower than the value at the design point) are usually accompanied with the formation of a helical precessing vortex, commonly referred to as precessing vortex core (PVC). The precession of the vortex with a frequency between 0.2 to 0.4 times the runner frequency induces pressure fluctuations in the draft-tube and the whole hydraulic system [8-13]. Cavitating vortex during part-load and high-load conditions are shown in Figure 1.3.

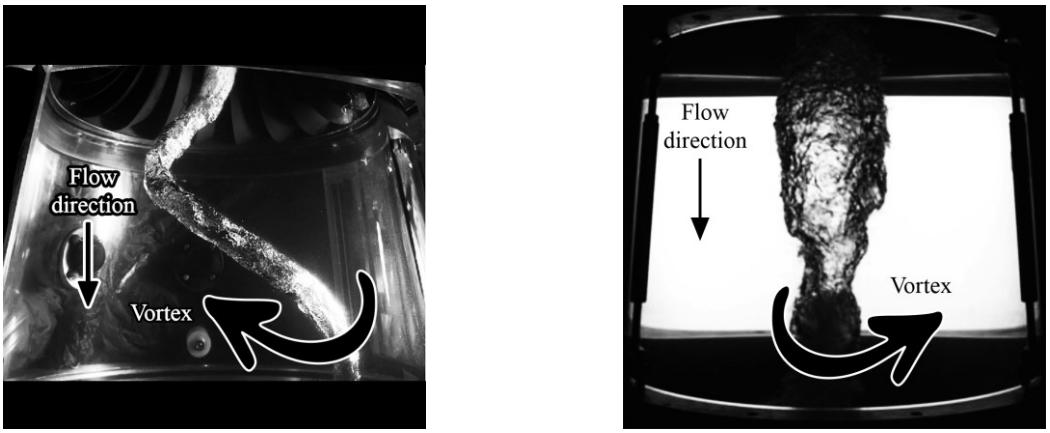

Figure 1.3. Cavitating vortex during a. part-load [14] and b. high-load [5] operating conditions

Presence of a vortical structure in the draft-tube of a hydro-turbine is usually accompanied with generally two types of pressure fluctuations (i.e., convective, and synchronous). While the

pressure fluctuations due to cavitation surge have a synchronous nature, the fluctuations due to the precessing vortex rope can be decomposed into two components occurring at the same frequency, namely the convective and synchronous components [15-19]. The convective component is a local pressure fluctuation observed only in the draft-tube and induced by the rotation of the pressure fields with the vortex core. The synchronous pulsation has equal phase and amplitude in a given section and propagates throughout the complete hydraulic circuit. Hydro-acoustic resonance can occur if the precession frequency coincides with one of the eigen frequencies of the hydraulic circuit [20-24]. According to the literature, the part-load operating range can be divided into three regimes by considering the vortex shape and behavior, i.e., upper part-load, part-load, and deep part-load, with two transitions splitting these regimes from each other [22, 25, 26]. In the first two regimes, the vortex rope features a high coherence and periodicity with the vorticity concentrated in its core. Beyond the transition between part-load and deep part-load regimes, the vortex rope loses its coherence, making the flow field in the draft-tube chaotic and difficult to predict [27, 28]. In addition, the formation of inter-blade vortices can be observed in the runner channel, which has been extensively studied by both experimental and numerical investigations [29-34].

1.2. State of the art

Vortical flow structures may appear with large scales in nature (e.g., tornados and typhoons) and with comparatively smaller scales in industry (as such in hydrodynamics and aeronautics). A vortex is generally generated in a turbulent swirling flow regime when the flow velocity field exhibits an angular momentum term. The vortex breakdown occurs when the flow angular momentum adequately surpasses the linear momentum, i.e., swirl intensity higher than a given threshold. In industry, the vortex breakdown is usually accompanied with undesirable effects (e.g., vortex induced vibrations in hydraulic machines) that reduces both the performance and the lifetime of machines.

Plenty of research works have been published in the literature with respect to the understanding of the vortex breakdown mechanisms. Escudier et al. [35, 36] discussed a two-stage transition scheme for vortex breakdown, where an axisymmetric supercritical vortex experiences its first transition into an intermediate supercritical phase featuring a counterflow zone (stagnation zone) and then the second transition to a subcritical phase. By conducting an experimental parametric study on the development and disappearance of the counterflow zone, they showed that the vortex remains axisymmetric until the onset of an oscillatory instability in vortex structure. Later on, Shtern [37] established the Swirl-Decay Mechanism (SDM) explaining the vortex breakdown mechanism. SDM proposes that the deceleration of the axial gradient of pressure along the axis of a swirling flow generates the counterflow zone as a result of swirl-decay downstream [38, 39]. It explains that the pressure at the rotation axis of the vortex is smaller than pressure at the periphery area due to the balance of the centrifugal force and the radial gradient of pressure. In addition, swirl-decay downstream increases the pressure along the axis; and reverses the flow consequently.

Lucca-Negro et al. [40] classified vortex breakdown types into six categories, among them only two types are observed for turbulent flows as such in hydraulic machines. In turbulent swirling flow fields, a vortex may break down either as a bubble or a spiral type. The bubble breakdown is characterized by a stagnation point located on the axis of an axisymmetric vortex, and a bubble-shape stagnation zone after the breakdown is formed by a counterflow region. The bubble breakdown can be followed by one or some spiral vortices called tails in reference [40]. On the other hand, in case of spiral breakdown, the vortex breaks into one or a twin helical vortex rotating with a certain angular velocity. This type of breakdown is usually reported as a Precessing Vortex Core (PVC) during part-load operation of reaction hydraulic machines such as a Francis turbine.

Vortex breakdown in the case of hydraulic machines usually occurs in the draft-tube during off-design operations. Hydraulic machines (such as Francis turbine) are designed to operate with a maximum efficiency at a given operating point - called the Best Efficiency Point (BEP). However, the current increasing need for electrical grid stabilization requires the extension of hydropower plant operating range from low-load to high-load. Off-design operation of hydraulic machines is accompanied with the development of an intense swirling flow at the runner outlet, leading to a vortex breakdown in the draft-tube [41]. The vortex breakdown induces unfavorable side effects in the hydraulic system emerging in form of severe pressure fluctuations and vibrations. The pressure fluctuations observed in hydraulic machines during off-design operations are characterized by their asynchronous (convective) or/and synchronous nature in the draft-tube cone. The convective pressure fluctuations correspond to the rotation of vortical structures and can induce local vibrations in the system; while the synchronous pressure pulsations, which feature equal phase and amplitude in any given cross-section of the draft-tube, can propagate in the entire hydraulic circuit and cause system resonance. This feature highlights the importance of research on the synchronous pressure pulsations. The synchronous pressure pulsations may be induced by the occurrence of different phenomena in the draft-tube of hydro-turbines, such as:

- Low-frequency oscillations of a vortex: it is frequently reported that a vortex core rotating in a diffuser (as a simplified test-case for draft-tube of hydro-turbines) experiences self-induced oscillations. These oscillations generate synchronous pressure pulsations featuring a lower frequency than the rotating frequency of the vortex. Appearance of low-frequency synchronous pressure pulsations in draft-tubes are very well known as source of hydraulic instabilities in hydro-machines. Several research groups have developed their investigations with respect to swirling flow generated by swirl generators in simplified draft-tubes. Stefan et al. [42, 43] used two different types of stationary-blades swirl generators (namely SG-RO and SG-CZ) to study the flow field in the draft-tube cone. Muntean et al. [44] and Stuparu et al. [45] separately reported that a vortex experiences a self-induced spring-like stretching-compressing behavior that generates low-frequency pressure pulsations in the system. However, the source of this stretching-compressing motion in the vortex filament is not yet clarified [44, 46-50]. In the very first part of the current thesis, dynamic behavior of an axisymmetric vortex is studied in a simplified draft-tube using experimental and numerical techniques.
- Cavitation surge instability: operation of hydraulic turbines at high-load conditions may be accompanied by self-induced cavitation surge phenomenon which generates strong synchronous pressure pulsations in the hydraulic circuit. Cavitation surge occurs in the draft-tube due to unstable oscillations of the cavity volume at one or more eigenfrequencies of the hydraulic

system [3-5, 20]. It is very well known that increase of gas content (or cavity volume) in fluids significantly decreases the wave speed [51]. In addition, decrease of wave speed in fluid flow decreases the natural frequencies of the hydraulic circuit. Meanwhile, excitation of the hydraulic system at one of its natural frequencies can induce resonance (cavitation surge instability) and severe pressure pulsations in the system. Presence of synchronous pressure pulsations in the draft-tube of hydro-turbines during off-design operating conditions may act as the excitation force to introduce cavitation surge with huge cavity volume fluctuations in the hydraulic system [3, 15, 52-54]. Considering the important role of this phenomenon in destabilizing the operation of a hydro-turbine during its off-design condition, many researchers introduced 1-Dimensional simulations to predict cavitation surge in a hydraulic system. In this regard, transfer matrix method is introduced first by Brennen et al. [55, 56] to relate the pressure and flowrate fluctuations at inlet of an inducer to the fluctuations of the outlet parameters. Even though, this method has been widely used by other researchers, there are different hydroacoustic parameters to be considered to predict cavitation surge – such as cavitation compliance, mass flow gain factor, and so forth.

Cavitation compliance which is a dynamic parameter represents the variation of cavity volume with change of pressure. Its value shows the local wave speed in a draft-tube which influences the travelling time of pressure waves. Brennen et al. [55] introduced a theoretical model to calculate cavitation compliance in a turbopump based on blade angle, blade thickness, and cavitation number. Later, Dörfler [57] measured cavitation compliance based on cavitation number for a vortex rope in the draft-tube of a Francis turbine. Couston [58] and Philibert [59] proposed a distributed approach for prediction of cavitation compliance based on wave speed and vortex rope length. Arpe et al. [9] developed this model by defining wave speed as a function of the curvilinear abscissa in the draft tube.

The other parameter which plays an important role at full-load operating condition of a hydro-turbine is mass flow gain factor. Mass flow gain factor represents the variation of cavity volume with change of flowrate in the draft-tube. Some researchers (such as Koutnik et al. [60], and Tsujimoto et al. [61]) used this approach to derive a stability diagram for cavitation surge occurring at full-load condition of a hydraulic turbine. Chen et al. [54] analyzed the influence of swirl intensity and diffuser factor on the system stability by deriving a general model by considering upstream and downstream flowrate and cavity. Muller [5] performed extensive experimental investigations to understand the underlying causes of cavitation surge instability.

In the current thesis, experimental techniques are adopted to understand cavitation surge inception in a simplified draft-tube by taking into account the intensity of swirling flow and cavitation number.

- Precession of a Vortex Core (PVC) in an asymmetric section: the helical vortex formed at runner outlet of hydraulic turbines during part-load operation can experience vortex breakdown in form of a helical vortex rotating with 0.2-0.4 times frequency of the runner rotation (f_{Runner}) in the draft-tube of the machine [8, 62]. The sole rotation of the PVC induces convective pressure fluctuations in the draft-tube, however its rotation in an asymmetric section (as in a draft-tube elbow) generates a forced-induced synchronous pressure pulsations featuring the same frequency as the convective component of pressure fluctuations [12, 13, 16, 63, 64]. In the current research, behavior of PVC is studied during deep part-load operating of a Francis turbine. It is observed that the PVC breaks down into smaller vortices which generate synchronous pressure pulsations with lower frequencies than the PVC. The physical generation mechanism of the low-frequency pressure pulsations in a draft-tube during deep part-load operation of a Franics turbine is studied in the last chapter of this thesis.

The current thesis is defined to study the abovementioned phenomena within three chapters. The structure of the thesis is explained in the next sub-section.

1.3. Thesis structure

The current thesis is dedicated to study the physics of three different phenomena that induces synchronous pressure pulsations in the draft-tube of hydro-turbines. Each chapter of this thesis focuses on a certain phenomenon. The thesis is structured in the following sections:

A. Chapter 2: Low-frequency synchronous pressure pulsations in a simplified draft-tube

The generation mechanisms of a synchronous pressure pulsations in a simplified draft-tube cone are studied using experimental and numerical techniques. The frequency spectrum of pressure pulsations from experiments is used to identify two pressure peaks with different natures (convective and synchronous) in the draft-tube. The convective component of pressure pulsations corresponds to local rotation of the vortical structure in the draft-tube. Unsteady-state numerical analysis is employed to investigate the source of the low-frequency synchronous pressure pulsations.

B. Chapter 3: Cavitation surge characteristics under different swirl intensities

A simplified geometry of draft-tube is used to study the characteristics of cavitation surge under different swirl intensities. Dynamic pressure measurements along with high-speed visualization of cavitation volume are employed to identify the surge characteristics. Natural frequencies of the hydraulic circuits are identified using the frequency spectrum of pressure, cavity volume fluctuations, and a simple 1D prediction. Several correlations are established between the natural frequencies of the hydraulic circuits and cavitation number along with void fraction.

C. Chapter 4: Generation of twin vortex rope in the draft-tube elbow of a Francis turbine during deep part-load operation

The model tests results of a Francis turbine are used to find the zero-swirl operating line of the turbine. A novel methodology is exploited to identify the iso-swirl lines on the Q_{ED}-n_{ED} hill chart. Using the definition of swirl number, the Q_{ED}-n_{ED} hill chart is divided into three regimes: a. upper part-load, b. part-load, and c. deep part-load. Unsteady-state CFD simulations are applied to investigate the source of a low-frequency synchronous pressure pulsations during the deep part-load operation.

2. Low-frequency synchronous pressure pulsations in a simplified draft-tube

2.1. Preface

This chapter focuses on the generation mechanisms of synchronous pressure pulsations featuring a lower frequency than the rotating frequency of a vortex core which are observed in a simplified draft-tube cone through analyzing the results of experiments along with unsteady-state numerical simulations. Unlike the previous works in the literature (mentioned in section 1.2) that proposed the stretching-compressing behavior of a helical vortex as the origin of the low-frequency pressure pulsations, the current research proposes to focus on the dynamics of the vortex breakdown and associated vortex characteristics downstream of the breakdown in order to achieving a different approach to clarify the link between the source of the phenomenon and the vortex breakdown. A stationary-blades swirl generator is designed by the authors to generate a uniform swirling flow downstream; and a Venturi-tube (comprising a converging, a throat, and a diffuser parts) is selected as the test case which resembles a simplified draft-tube geometry of a hydraulic turbine. In the first part of this chapter, the results of pressure measurement from experiments are used to identify the characteristics of the pressure fluctuations in the Venturi cone. Then in the next part, unsteady numerical simulation is conducted to accurately capture the flow field characteristics during the vortex breakdown. The breakdown location is identified later using three different methods. Finally, the dynamic behavior of both the breakdown location and the downstream vortices is analyzed in the last section of the chapter.

2.2. Experiments

2.2.1. Description of the test case

A Venturi-tube with a stationary-blades swirl generator (called swirler hereafter) is employed to reproduce the characteristics of the draft tube flow in hydraulic turbines operating in off-design conditions. The existing test case is used to study the behavior of an axisymmetric vortex which can appear in the draft-tube cone of hydro turbine during its off-design operating points (away from the best efficiency point, BEP). The closed-loop test rig, as shown in Figure 2.1, consists of the upstream and downstream tanks, the upstream and downstream straight pipes, a swirler, and a Venturi. The water is driven from the downstream tank to the upstream tank using a centrifugal pump. The upstream pipe is adequately long (16**D*, where *D* = 105 *mm*) to ensure a uniform flow field upstream of the swirler. The maximum achievable flowrate is 1,100 L/min

using the existing pump. The cavitation number σ, as defined in equation 2.1, can be adjusted in the test section by using a vacuum pump connected to the downstream tank.

$$\sigma = \frac{P - P_v}{\frac{1}{2}\rho V_{m,th.}^2} \qquad \textbf{2.1}$$

where P, P_v, and ρ are the mean pressure in the Venturi throat, the water vapor pressure in the room temperature, and the water density, respectively. The parameter $V_{m,th.}$ is the mean flow velocity in the Venturi throat and is calculated through division of the mean flowrate (m^3/s) by the throat area (0.0017 m^2). The cavitation number in the test section can be reduced to minimum 0.3 at the highest operating flowrate.

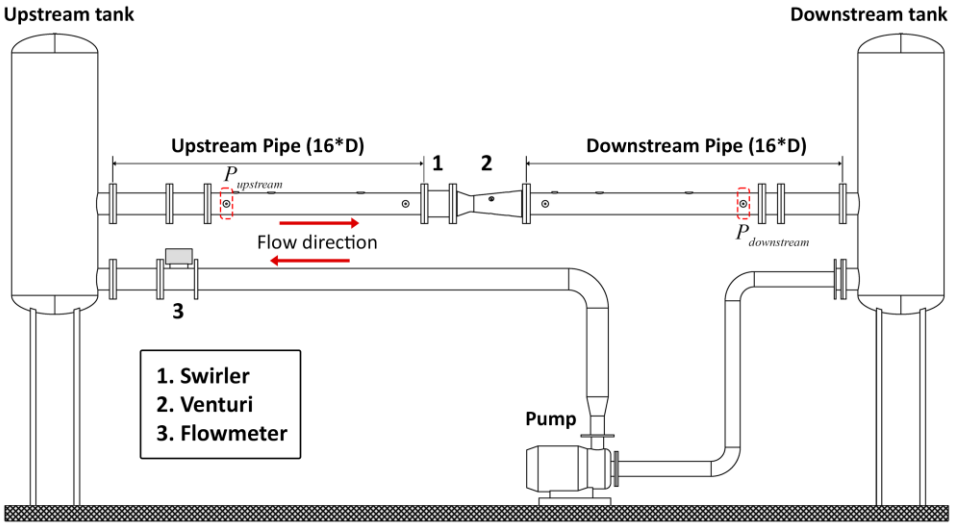

Figure 2.1. General layout of the test rig

The swirler (Figure 2.2), which is located at the upstream of the Venturi, features 9 stationary blades with tip diameter equal to D = 105 mm. It is designed to reproduce a uniform swirling flow with a swirl number approximately equal to S = 0.65 at its outlet. The swirl number S is a dimensionless parameter to characterize the swirl intensity and corresponds to the ratio between the axial flux of the angular momentum and the axial flux of the axial momentum [26, 65], as introduced in equation 2.2:

$$S = \frac{G_\theta}{R.G_z} = \frac{\int_0^R V_m.V_t.r^2.dr}{R.\int_0^R V_m^2.r.dr} \qquad \textbf{2.2}$$

where V_m and V_t are the meridional and tangential velocity components.

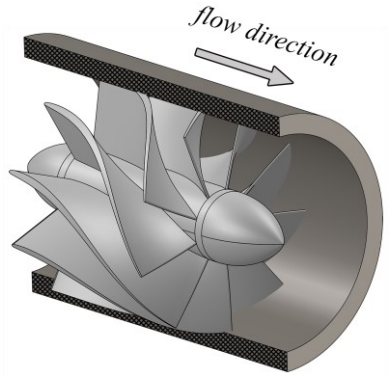

Figure 2.2. 3D geometry of the swirler

The meridional and tangential velocity profiles at runner outlet of hydro-turbines vary from one turbine to another, depending on the turbines' types and characteristics. This importance makes it challenging to set a swirl-configuration similitude between two certain operating conditions associated with two different turbines using the meridional and tangential velocity profiles. However, Favrel et. al [26] showed that using the non-dimensional swirl number is an adequate way to find swirl-configuration similitude between two certain operating conditions in different Francis turbines (e.g., similar swirl number can be obtained with different meridional and tangential velocity distributions from one turbine to another). They proved that the swirl number can be defined as a sole function of discharge (Q_{ED}) and speed (n_{ED}) factors at a certain operating point as presented in equation 2.3:

$$\overline{S} = n_{ED}\frac{\pi^2}{8}\left(\frac{1}{Q_{ED}} - \frac{1}{Q_{ED}^0}\right) \qquad \textbf{2.3}$$

where Q_{ED}^0 corresponds to the discharge factor at the no-swirl condition for a given n_{ED} value.

In the current chapter therefore, the same approach is followed to find a swirl-configuration similitude between the studied conditions in this chapter and the related operating conditions associated with hydro-turbines. The draft-tube flow field of hydro-turbines are frequently divided into four regimes using the swirl number definition (as defined in equations 2.2 and 2.3) with respect to the BEP featuring no-swirl condition ($S \approx 0$). The four draft-tube flow regimes are determined in the literature [3, 5, 26, 63, 66-69] and presented in Table 2.1:

Table 2.1. Draft-tube flow regimes with respect to BEP featuring S ≈ 0

Regime	Swirl number	Direction of rotation	Vortex shape
High load [3, 5, 66]	$S < 0$	Opposite to the runner rotation	Axisymmetric
Upper part-load [12, 63, 66]	$0 < \|S\| < 0.4$	Same as the runner rotation	Helical
Part-load [12, 63, 66]	$0.4 < \|S\| < 1.7$		
Deep part-load [63]	$\|S\| > 1.7$		

It is mentioned above that the swirl number at the swirler outlet is 0.65, however it will be shown later in the chapter that the swirl number S is reduced to approximately $S \approx 0.35$ in the Venturi throat (the similar location as the runner outlet in hydro-turbines). With considering the axisymmetric shape of the vortex in the current research (which will be presented later) along with the value of the swirl number in the throat ($S \approx 0.35$), it is speculated that the studied operating conditions in the present chapter may show similar swirl-configurations with the draft-tube flow field during high-load operating regime (according to Table 2.1).

The acrylic Venturi, as shown in Figure 2.3, features three parts: A. a 19.2-degree converging part, B. a straight throat ($D_{throat} = 47\ mm$), and C. a 6-degree diverging part (hereinafter called the Venturi cone). The converging part concentrates the swirling intensity in the center of the throat in pursuance of developing a uniform axisymmetric vortex core which resemble the vortex shape at the runner outlet of hydro turbines during high-load operating conditions [5].

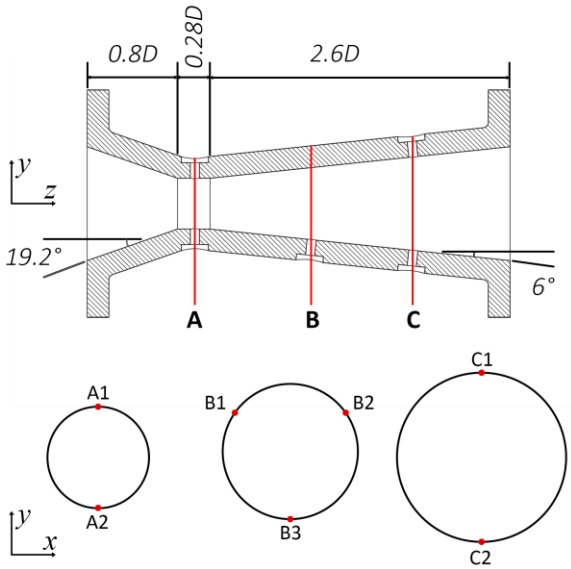

Figure 2.3. Pressure measurement points in the Venturi

Dynamic pressure measurements are carried out at 5 sections between the upstream and downstream tanks using 11 wall flush-mounted pressure sensors (small-sized pressure transducer with measurement range: 0-1 *MPa*, and accuracy: 0.2%). The upstream and downstream pressure sensors are located far upstream and downstream of the Venturi at $P_{upstream}$ and $P_{downstream}$, respectively, as shown in Figure 2.1. The recorded data from pressure sensors located at 3 sections (sections A, B, and C in Figure 2.3) in the Venturi are used to highlight the local behavior of the vortex in the Venturi cone. At sections A and C, two pressure sensors with 180 degrees difference in angular location are located, while three pressure sensors are installed at section B with 120 degrees difference in their angular location. Flowrate is measured using an ultrasonic flowmeter

as shown in Figure 2.1.

2.2.2. Identifying the vortex-induced pressure fluctuations

To identify the frequency and amplitude of the vortex-induced pressure fluctuations for different operating flowrates in the Venturi, a Fast Fourier Transform (FFT) of the recorded pressure signals in sections A, B and C is performed. To do so, pressure measurements are performed for seven different operating flowrates from 300 to 900 *L/min* presented Table 2.2.

Table 2.2. Operating conditions

Flowrate	Re. number	Maximum achievable Cav. No.	Cavitation
[*L/min*]	[-]	[-]	(yes / no)
900	$1.72*10^{+5}$	2.6	yes
800	$1.53*10^{+5}$	2.9	yes
700	$1.34*10^{+5}$	4.0	yes
600	$1.15*10^{+5}$	6.1	yes - intermittent
500	$9.58*10^{+4}$	8.9	no
400	$7.66*10^{+4}$	13.0	no
300	$5.75*10^{+4}$	24.8	no

The Reynolds number presented in Table 2.2 for each operating flowrate is calculated using equation 2.4:

$$\mathrm{Re} = \frac{\rho . V_{m,up.} . D}{\mu} \qquad \textbf{2.4}$$

where μ and $V_{m,up.}$ are the dynamic viscosity of water in room temperature ($Pa.s$) and the upstream mean velocity (m/s), respectively.

Table 2.2 shows that the maximum achievable cavitation number for each operating flowrate is different depending on the mean velocity in the Venturi throat, see equation 2.1. Therefore, for higher flowrates than a certain value (here 600 *L/min*), it is not possible to avoid cavitation during the measurements.

Pressure signals at each operating flowrate are recorded for 100 *sec* of experiments to achieve more accurate FFT calculation. Then the complete 100-sec signals are divided into 49 4-sec windows with 50% overlapping between each, and FFT is calculated over each window. The results of FFT for seven operating flowrates at sections B and C are presented in Figure 2.4. The frequencies (f) and amplitudes ($P_{amp.}$) of pressure fluctuations are normalized as the Strouhal No. (equation 2.5) and the pressure coefficient (equation 2.6), respectively, to generalize the presented results in the current chapter.

$$Str. = \frac{f.D^3}{Q} \quad \textbf{2.5}$$

$$P^* = \frac{P_{amp.}}{\frac{1}{2}\rho V_{m,up.}^2} \quad \textbf{2.6}$$

where Q is the flowrate (m^3/s).

FFT of pressure signals at section A (sensors A1 and A2) shows that pressure fluctuations feature a very small amplitudes in this section which can be misinterpreted with background noises. Thus, the results of FFT for section A are not presented here.

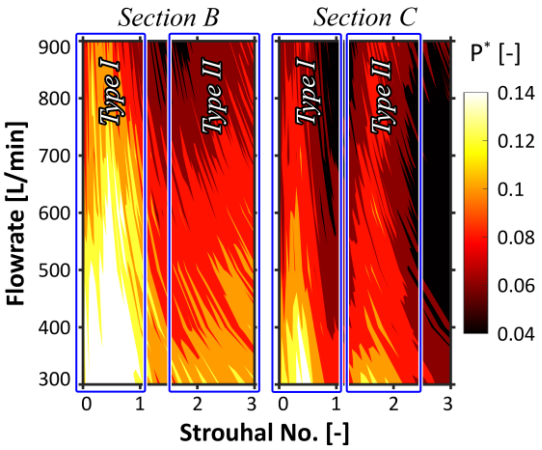

Figure 2.4. FFT of pressure fluctuations in the Venturi cone for seven flowrates

Figure 2.4 shows that pressure fluctuations are observed within different ranges of Strouhal numbers in both sections B and C in the Venturi cone. Two pressure peaks covering wide ranges of Strouhal numbers are identified in both sections B and C, where one peak is located between Strouhal numbers 0 to 1 (type I) and the other covers Strouhal numbers over 1 (type II). The Cross Spectral Density (CSD) between two pressure sensors located in the same cross-sections is then calculated to highlight the nature of pressure fluctuations, i.e. synchronous or convective, via the analysis of the CSD phase. The CSD is calculated between two sensors spaced by $2\pi/3$ *rad* and by π *rad* in angular position in sections B and C, respectively. The pressure fluctuations are purely convective if the phase difference between two signals estimated by CSD is equal to the difference in the angular location of the two sensors ($2\pi/3$ *rad* for section B, and π *rad* for section C); while they have a pure synchronous nature if the phase difference is equal to 0. If the phase difference between two signals has a value other than the abovementioned values for each section, the pressure fluctuations correspond to the superimposition of synchronous and convective components occurring at the same frequency [24].

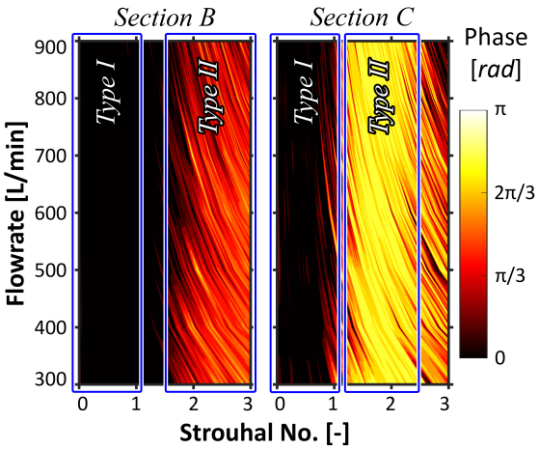

Figure 2.5. Phase difference between two sensors on sections B and C for seven flowrates (the difference in angular locations of two sensors on sections B and C are 2π/3 and π/2, respectively)

Figure 2.5 shows the phase difference between the selected sensors on sections B and C. It presents that the pressure peaks type II corresponding to the Str. numbers 1.6~ on section B and to the Str. numbers 1.1~ on section C have a convective nature and therefore may correspond to rotation of a vortical structure in sections B and C. On the other hand, the pressure peaks type I corresponding to Str. numbers 0 to 1 in both sections B and C feature a synchronous nature. With considering the presented results in Figure 2.4, it is confirmed that both types I and II pressure peaks observed in the Venturi cone cover a wide range of frequencies. This conveys that the phenomena which generate these pressure fluctuations feature an important stochastic component. The nature of pressure fluctuations in the Venturi cone will be explained in more details in the next section (2.2.3).

2.2.3. Nature of pressure fluctuations in the Venturi cone

The presence of a rotating vortical structure in the Venturi is suggested in the previous section (2.2.2) by computing the phase difference between two pressure sensors on cross sections B and C. For better understanding of the nature of the pressure fluctuations occurring in the Venturi, pressure signals at each cross section in the Venturi are decomposed in the time domain into two convective (asynchronous) and synchronous components. The convective component, induced by the local rotation of vortical structures in diffusers (similar to a PVC observed in hydraulic turbines during the part-load operation [12]), features a different phase rather than the difference in the angular location of two pressure sensors located in a given cross-section in the diffuser. While, the synchronous component of pressure fluctuations, which can be generated by one of the phenomena described in the introduction section of the thesis (section 1.2), features

equal phase and amplitude in a given cross-section [6] and can be seen as a pressure wave propagating in the system. The convective component is observed only locally in the diffuser whereas the synchronous pressure pulsations propagate in the complete hydraulic circuit and may cause resonance if their frequency coincides with one of the eigen frequencies of the circuit [23].

Using the raw pressure signals in the Venturi cone, the synchronous and convective components of pressure fluctuations at each section for each sensor can be computed through equations 2.7 and 2.8, respectively [20, 26]:

$$P^{synch.}(t) = \frac{1}{n}\sum_{i=1}^{n} P_i(t) \qquad \textbf{2.7}$$

$$P_i^{conv.}(t) = P_i(t) - P^{synch.}(t) \qquad \textbf{2.8}$$

where n is the number of pressure sensors at each section ($n = 3$ for section B, and $n = 2$ for section C). P_i and $P_i^{conv.}$ represent the raw and the convective components, respectively, for each sensor; and $P^{synch.}$ corresponds to the synchronous component at each section. Figure 2.6 shows an example of pressure signal decomposition into two synchronous and convective components in the time domain (on sections B and C) using equations 2.7 and 2.8.

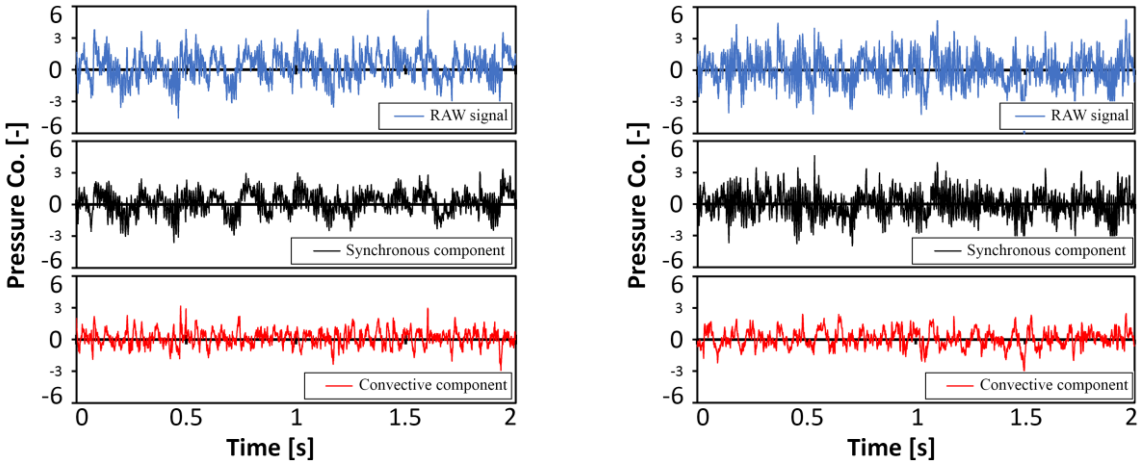

Figure 2.6. Example of pressure signal decomposition into synchronous and convective components in the time domain a. for sensor B1 on section B, and b. for sensor C1 on section C

FFT of the synchronous and convective pressure components for sensors B1 and C1 on cross sections B and C are calculated and plotted in_Figure 2.7. The convective pressure fluctuations in Figure 2.7 (type II) confirms the existence of a rotating vortex in both cross sections B and C which is in agreement with the phase difference results presented in Figure 2.5. Moreover, the low-frequency synchronous pressure peak (type I) is also identified in both sections B and C covering Str. numbers 0 to 1. It is noticed in Figure 2.7 that the pressure fluctuations type I and II feature different frequencies in both sections B and C which suggests that two different phenomena are responsible for their generation. It is confirmed that type II convective pressure

fluctuations are induced by local rotation of vortical structures in the Venturi cone, however, the source of type I synchronous pressure pulsations remains unknown in this section of the chapter.

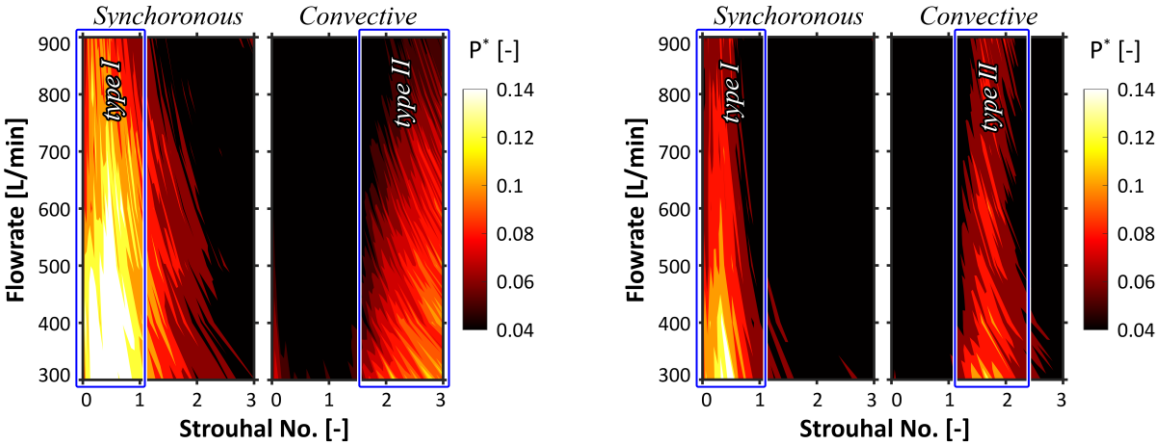

Figure 2.7. FFT of synchronous and convective pressure components for seven flowrates on a. cross section B and b. cross section C

Properties of two types (I and II) pressure peaks in sections B and C are presented in Table 2.3. It is seen that both types pressure peaks cover a wide range of frequencies.

Table 2.3. Properties of pressure peaks I and II in sections B and C

	Type I		Type II	
	Range (Str. No. [-])	Peak (Str. No. [-])	Range (Str. No. [-])	Peak (Str. No. [-])
Section B	0 ~ 1	0.42	1.6 ~ 5.5	3
Section C	0 ~ 1	0.42	1.1 ~ 2.7	1.9

It is also noticed in Table 2.3 that the convective component in section C features a lower frequency than the convective component in section B. This suggests that the vortical structures in the diffuser lose their strength from section B to C. Similar to this, Nishi et al. [70] observed for a deep draft-tube that rotating frequency of a vortex core is decreased from runner outlet to draft-tube elbow.

According to Table 2.2, cavitation appears for the flowrates higher than 600 *L/min* even at their corresponding maximum achievable cavitation number. Appearance of cavitation induces a modification in hydro-acoustic properties of the hydraulic system that affects the vortex behavior. Therefore, to eliminate the influence of cavitation on vortex behavior, the results of experiments for flowrate 500 *L/min* (exhibiting a cavitation-free condition) are selected to study types I and II pressure fluctuations in the Venturi cone. The FFT of the synchronous and convective pressure fluctuations at sections B and C are extracted from Figure 2.7 for flowrate 500 *L/min* and shown in Figure 2.8.

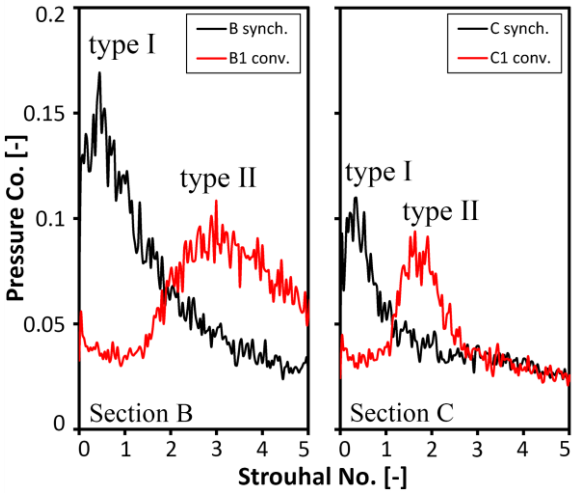

Figure 2.8. FFT of synchronous and convective pressure fluctuations for flowrate 500 *L/min* in sections B and C

Types I and II pressure fluctuations are clearly identified in Figure 2.8. It is also interesting to notice that the type I pressure fluctuations (synchronous) are observed far upstream and downstream of the Venturi. The FFT of the synchronous pressure component which is calculated far upstream and downstream of the Venturi (at locations $P_{upstream}$ and $P_{downstream}$ showed in Figure 2.1) and is plotted in Figure 2.9 confirms this importance.

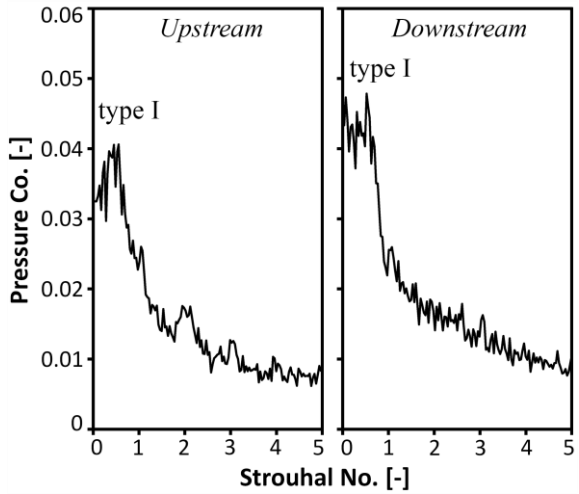

Figure 2.9. FFT of synchronous pressure component at upstream and downstream of the Venturi

By considering the similar reported results in the literature, it can be deduced that the pressure peak type I with synchronous nature (covering Str. numbers between 0 to 1, which can be observed everywhere in the test rig) may correspond to the low-frequency oscillating behavior of the vortex reported by [48, 49, 71].

To catch a roughly accurate image of the vortex shape, the cavitation number at flowrate 500 *L/min* is reduced to a value exhibiting the cavitation appearance in the Venturi (σ = 2.3). By using a high-speed camera, the vortex shape is captured and visualized as shown in Figure 2.10. In Figure 2.10, three states are identified in the vortex shape: a state that exhibit an axisymmetric

vortex generated downstream of the swirler, a state featuring the vortex breakdown, and a third state at which an intermittent helical vortex is developed after the breakdown location. It is important to mention that the helical vortex after the breakdown location shows an intermittent behavior by appearing and disappearing in different shapes and lengths. The appearance of cavitation in the Venturi may slightly affect the vortex characteristics, however, it is assumed that the flow behavior observed in cavitation conditions are qualitatively similar to the one in cavitation-free conditions.

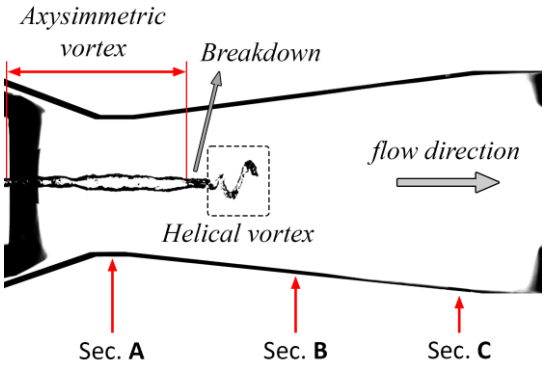

Figure 2.10. Vortex rope development in the Venturi

Stuparu et al. [50] and Muntean et al. [44] explained that a periodic compressing-stretching of the helical vortex generated after the breakdown of the axisymmetric vortex in the Venturi cone induces a synchronous (or plunging) pressure fluctuations in the system. However, the physical mechanism generating this periodic compressing-stretching behavior in the vortex dynamics have not been clearly identified yet. The following sections will elaborate upon the understanding of the dynamics of the vortex in the Venturi cone to determine a comprehensive explanation for the generation of the low-frequency synchronous pressure fluctuations.

2.3. Numerical simulations

The unsteady-state numerical simulations are performed for the previously selected operating condition (flowrate 500 *L/min*) to investigate the vortex development in the current and the next sections of the chapter.

2.3.1. Steady-state CFD simulation setup

Steady-state CFD simulations are first performed to study the mesh dependency of the numerical results and determine the mesh refinement to be used for further unsteady-state CFD

simulations of flow in the Venturi. The flow field is simulated by solving the RANS equations by the commercial CFD code ANSYS CFX 19.0 with incompressible and turbulent flow assumptions. The SSG Reynolds stress turbulence model with default turbulent quantities is adopted to accurately predict the vortex behavior with considering the strong streamlines curvature [72]. Reynolds stress turbulence models (RSM) use separate transport equations to solve each components of the Reynolds Stress tensor and the dissipation rate; they outperform the Eddy-viscosity based models (like k-ε and k-ω models) in predicting the flow behavior with strong anisotropy (such as flows with a strong swirling component) [73-75].

In addition, Reynolds's stress models show better performance than two-equation models, but their increased number of transport equations leads to a reduced numerical robustness [76-78]. Accordingly, their performance is very sensitive to mesh quality especially at the general grid interfaces (GGI) where numerical approximations are made. Therefore, one unified mesh for the whole computational domain is generated without setting up any GGI interfaces between the components of the test rig from the upstream to downstream pipes (see section 2.2.1).

The numerical domain, as shown in Figure 2.11, includes a 5-*D* long upstream pipe, the swirler, the Venturi tube, and a 7-*D* long downstream pipe. The inlet and outlet boundary conditions are set to normal-to-boundary velocity and average static pressure, respectively. The normal velocity at inlet is set to 0.957 *m.sec-1* (corresponding to flowrate 500 *L.min-1*) and the static pressure at outlet is fixed to the same value from experiments at which cavitation does not occur. High resolution advection scheme is applied to the governing equations. The convergence criteria are defined as RMS below 1e-05.

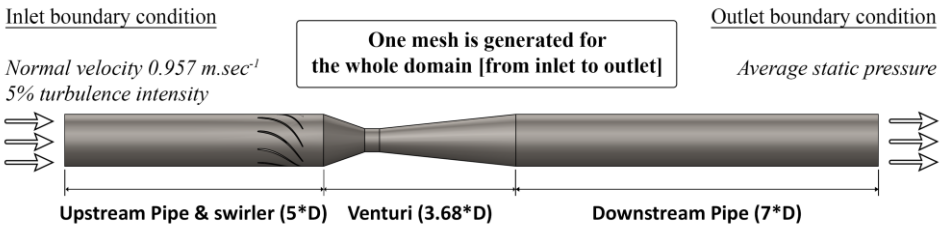

Figure 2.11. Numerical domain

2.3.2. Mesh independency

A mesh independency study is performed using the steady-state CFD simulations to evaluate the dependency of the results to the grid size. To do so, four grids with different densities are generated and steady-state CFD simulations are carried out. The size of all grids is presented

in Table 2.4. Grid No. 04, as described in Table 2.4, is significantly large (10 times larger than grid No. 03) to investigate the difference in accuracy of CFD predictions between a fine (No. 03) and a super fine grid (No. 04).

Table 2.4. Mesh information

Mesh	Mesh type	Nodes
01	Tetrahedral	0.91 M
02		1.28 M
03		2.01 M
04		19.9 M

To investigate the dependency of CFD predictions on grid size, LDV measurements are conducted in the throat of the Venturi and then compared with steady-state CFD results. The comparison of the meridional (V_m) and tangential (V_t) velocity profiles between the steady-state CFD simulations and the time-averaged LDV results are presented in Figure 2.12. CFD results for all grid sizes show a very fair agreement in both V_m and V_t for locations over $r^* > 0.3$ (where $r^* = r/R_{throat}$, and R_{throat} is the throat diameter). In the center of the throat ($0 < r^* < 0.3$), however, the steady-state CFD results show a large deviation with the experiments. High values of standard deviation for the experimental results (LDV) near the center of the throat (Figure 2.12) reveals that the flow becomes extremely unsteady and experiences a wake-like velocity deficit. Consequently, all the steady-state CFD simulations with different grid sizes (incl. the super fine grid No. 04) are unable to predict the flow field accurately in this region. However, it is noticed that the difference between the results obtained from grids No. 3 and No. 4 is negligibly small which means that the CFD predictions are independent of the grid size. Considering the existing computational resources, grid No. 3 is selected for further analysis in the following sections.

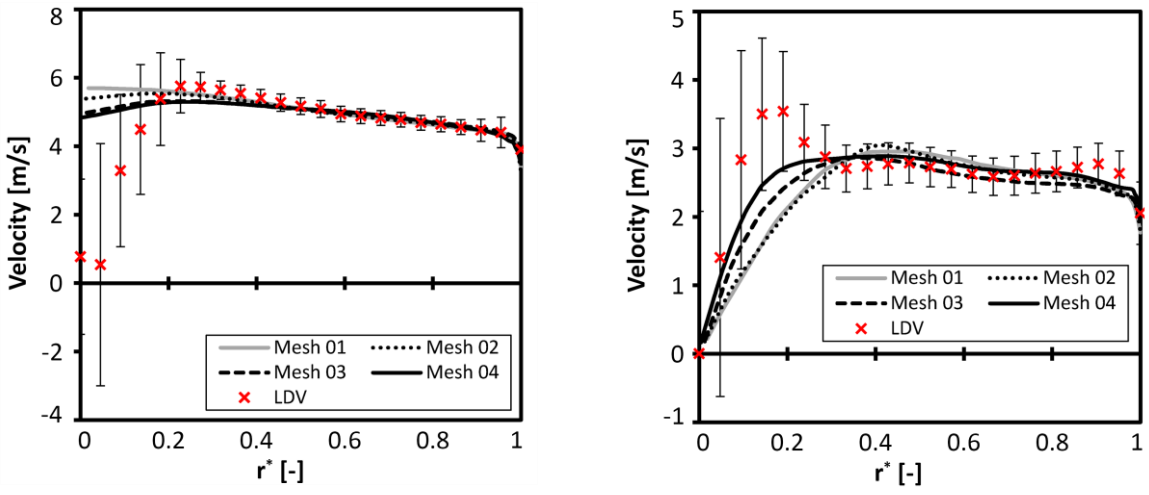

Figure 2.12. a. Meridional and b. tangential velocity profiles in the Venturi throat for different grid sizes

2.3.3. Unsteady-state CFD simulation setup

It is seen in the previous section (2.3.2) that steady-state CFD simulations are unable to accurately capture the velocity profiles in the center of the Venturi throat. Therefore, unsteady CFD simulation is performed to study the source and the mechanism of generating the low-frequency synchronous pressure fluctuations highlighted in section 2.2.3. To do so, the URANS equations are solved using ANSYS CFX 19.0 with SSG RSM turbulence model as discussed in section 2.3.1. The simulation timestep is selected as Δt = 1e-4 sec resulting in an RMS Courant number equal to 0.13. The Courant number, as simply defined in equation 2.9, is a dimensionless value representing the time that a particle of fluid stays in one grid cell.

$$Co. = u_{particle} . \frac{\Delta t}{\Delta x} \qquad \textbf{2.9}$$

where $u_{particle}$, Δt, and Δx are the velocity magnitude of the fluid particles, the timestep size, and the size of grid cells, respectively. The Courant number should be less than 1 and ideally less than 0.7 to assure that the movement of any fluid particles is computed at least for two timesteps in each grid cell. Therefore, the achieved Courant number equal to 0.13 is adequately small to achieve accurate predictions. The convergence criteria are defined as RMS below 1e-05, same as for the steady-state simulations. The pressure data are recorded for 10 sec by using monitoring points placed at the same locations as the pressure sensors during experimental tests, see in Figure 2.3. Moreover, for further investigations of the vortex behavior in the next section, the transient result files including the velocity and pressure data in the complete computational domain are exported for 6 *sec* with 0.01 *sec* time intervals. The computation time for the unsteady simulation is 2.8e+7 CPU-seconds using 8 CPU cores.

2.3.4. Validation of unsteady-state CFD results

The main objective of the unsteady-state CFD simulation is to study the vortex behavior in the diffuser part of the Venturi; it is therefore necessary to validate the obtained results from the unsteady-state CFD simulation against the experimental results measured in the Venturi cone. Due to experimental limitations, it is only feasible to perform the LDV measurements in the Venturi throat. Thus, the meridional (V_m) and tangential (V_t) velocity profiles are first compared between CFD and experiments in the Venturi throat area. Moreover, the pressure fluctuations in two sections in the Venturi cone (sections B and C) are compared to assure validity of the unsteady-state CFD results.

Figure 13 shows the comparison of the meridional and tangential velocity profiles in the Venturi throat between the results obtained from the unsteady-stated CFD simulation and the experiments. It is seen that the unsteady-state CFD simulation, unlike the steady-state CFD, can accurately predict the wake-like velocity deficit in the center of the throat (Figure 2.13.a). The average differences in V_m and V_t profiles presented in Figure 2.13 are 6.43% and 3.71%, respectively, which shows an acceptable agreement between the results of unsteady-state CFD simulation and experiments [79, 80]. It is also of interest to mention that the velocity profiles presented in Figure 2.13 are similar to those reported by Stefan et al. [42] for their SG-RO test-case.

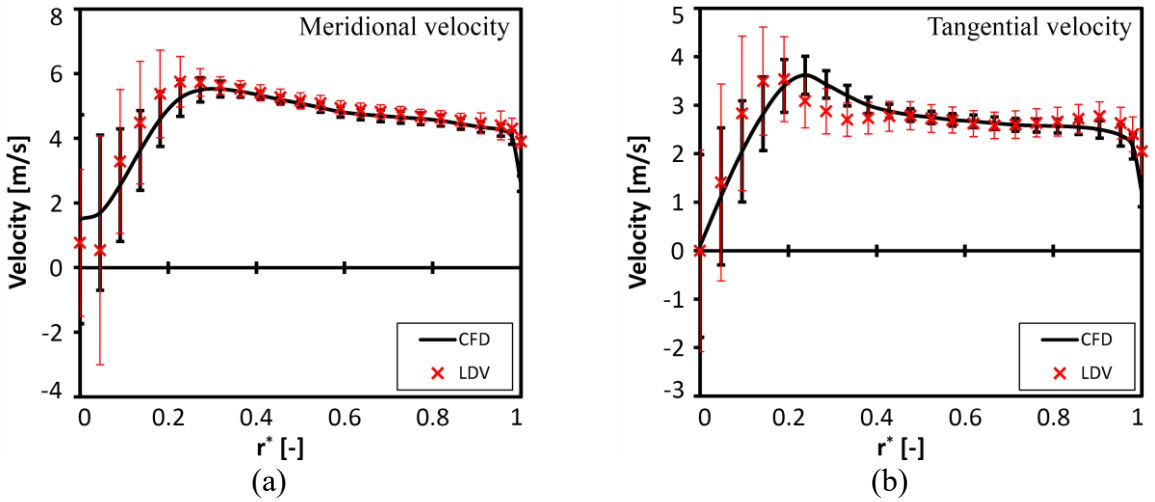

Figure 2.13. Comparison of a. meridional and b. tangential velocity profiles between unsteady-state CFD simulation and experiments

Furthermore, to validate the unsteady-state CFD results in the Venturi cone, FFT of the pressure fluctuations in sections B and C are compared with experiments. The simulated pressure data at the monitoring points are decomposed into synchronous and convective components by using equations 2.7 and 2.8 (as explained before in section 2.2.3), and FFT of the synchronous and convective pressure fluctuations are computed. Figure 2.14 shows the comparison of FFT analysis at two sections in the Venturi cone (sections B and C). It is seen that CFD predicts the frequencies of both synchronous and convective pressure pulsations sufficiently accurate, with considering the very short time of CFD simulations (10 *sec*) in comparison with longer pressure measurements in experiments (100 *sec*). However, CFD overestimated the amplitudes of pulsations for the convective component on section B (B.II) and the synchronous component on section C (C.I). Similar to experiments, CFD shows that both the synchronous and convective frequency peaks cover a wide range of frequencies (from Str. number 0 to 1 for the synchronous component) which conveys that the phenomenon responsible for these fluctuations features an important stochastic nature.

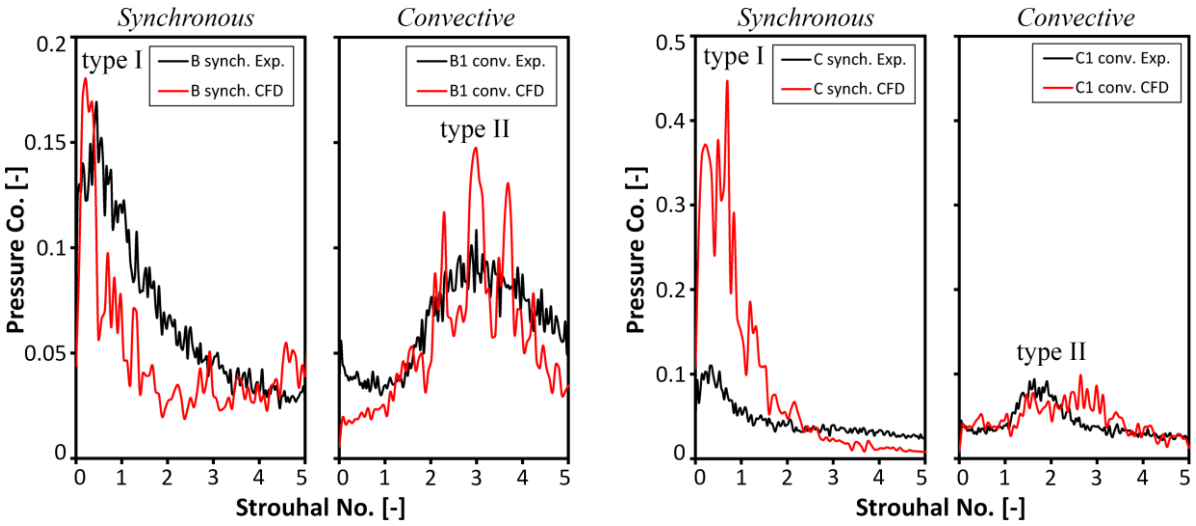

Figure 2.14. Comparison of pressure fluctuations between CFD and experiments at a. section B and b. section C

In cases that the flow field has somewhat a stochastic behavior, it is necessary to perform FFT analysis over a large set of recorded data to achieve accurate results for the amplitude of pulsations. Accordingly, the pressure data are recorded for 100 *sec* during experiments. However, due to lack of computational resources, it was not possible to maintain unsteady-state simulations over 10 sec. This may explain the reason why such discrepancies between experiments and CFD is observed for the amplitudes of peaks B.II and C.I.

In the following, the results of unsteady-state CFD simulations are analyzed in more details in both time and frequency domains to understand the physical mechanism behind the generation of the low-frequency synchronous pressure component.

2.4. Results and discussion

Analysis of the visualizations of the Venturi flow in cavitation conditions (mentioned briefly in section 2.2.3) showed that the location of vortex breakdown may vary over time at a low frequency. This suggests that there may be a link between the fluctuations of the vortex breakdown location and the low-frequency synchronous pressure fluctuations observed in the experiments. Therefore, this section of the chapter is allotted to study the Venturi-tube flow dynamics under two subsections: the first subsection (2.4.1) is dedicated to find the generation mechanism of the low-frequency synchronous pressure fluctuations by analyzing the location of the axisymmetric vortex breakdown over time in the Venturi cone; and in the second section (2.4.2), the dynamic

behavior of flow near the vortex breakdown location and associated vortical structures are discussed thoroughly.

2.4.1. Origin of the low-frequency synchronous pressure pulsations

2.4.1.1. Identification of the time-averaged location of the vortex breakdown

Different techniques are adopted to identify the time-averaged location of vortex breakdown, and the results of each are compared to evaluate the accuracy of the CFD results. Sarpkaya [81] proposed that the vortex breakdown occurs where the pressure excess ratio C_p along the axis of a pipe (or a diffuser) reaches a local maximum. Pressure excess ratio C_p, as defined in equation 2.10 with reference to the inlet section of the Venturi cone (throat outlet section), expresses essentially the axial pressure gradient along the Venturi cone. It is shown that after the breakdown point at the C_p local maximum, a slight drop in C_p (negative pressure gradient) occurs and is then followed by a pressure recovery phase.

$$C_P = \frac{P - P_{throat}}{\frac{1}{2}\rho V_{m,th}^2} \qquad \textbf{2.10}$$

where P and $V_{m,th}$ are pressure and meridional velocity, respectively.

Figure 2.15 shows the time-averaged C_p values along the Venturi axis (z-direction) where $z^* = 1$ ($z^* = z/D$ is the dimensionless axial location) corresponds to the throat outlet (the reference plane). The C_p reaches a local maximum and deviates from its parabolic trendline with a slight drop around z* = 1.8 - 1.9. This conveys that the breakdown may occur around this location in the Venturi cone. Due to the diffuser effect, the C_p-drop after the breakdown point is comparatively small in comparison with a pipe flow [81]. It is further noticed in Figure 2.15 that after the breakdown point the standard deviation of C_p is significantly increased which reveals that the flow has entered to an unstable mode.

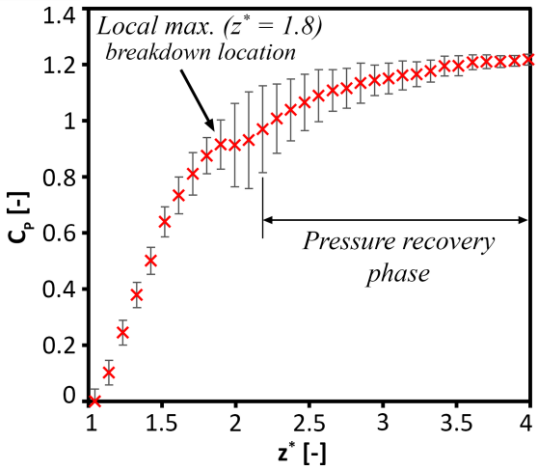

Figure 2.15. Evolution of the time-averaged pressure excess coefficient C_p along the Venturi diffuser (z-direction)

Furthermore, from the wave phenomena point of view, Squire [82] and Benjamin [83] separately developed the concept of critical state to estimate the breakdown location for an axisymmetric vortex. By considering the swirling strength of an axisymmetric vortex, the concept of critical state suggests that the vortex breakdown occurs at a critical phase which is located between a supercritical and a subcritical phase. An axisymmetric vortex in its supercritical phase shows a stable behavior. At the subcritical stage, it is assumed that the vortex has lost its coherence after breaking down and dissipates in smaller scale turbulent vortices.

The limits of the above-mentioned phases are derived from the Quasi-Cylindrical Approximation (QCA) which is initially proposed by Gartshore et al. [84]. The QCA suggests that the axial derivatives in the viscous terms of the momentum equations are neglected and the radial momentum equation reduces to a balance between the pressure force and the radial acceleration because of the swirl. The QCA assumption enables to numerically calculate the development of swirling flows along the axis. However, by considering the viscous effect, the QCA fails to compute the swirl intensity at a certain location (singularity point) since the radial velocity components of flow separately tends to positive and negative infinity. Later, Shi et al. [85] showed that this singularity in QCA assumption corresponds to the same critical phase of a vortex characterized by Squire [82] and Benjamin [83]. By considering this observation, they computed the limits of the supercritical, critical, and subcritical phases in the concept of critical state for an axisymmetric vortex as shown in Figure 2.16.

To quantify the critical region, the characteristic parameter k is defined as the ratio of the maximum time-averaged tangential velocity (V_t) to the mean time-averaged meridional velocity (V_m) at each cross section in the Venturi cone. The parameter k increases in the streamwise direction due to viscosity and geometry effects. For a swirling flow exhibiting an axisymmetric vortex core, therefore, the flow upstream of the breakdown location is considered supercritical.

The parameter k is then decreased when moving streamwise from the upstream while its value is approaching to the critical region. Figure 2.16 shows that the swirling flow reaches the critical limit at $z^* = 1.8$ and enters completely into the critical phase at $z^* = 1.9$. As described above with the concept of critical state, the vortex breaks down near $z^* = 1.8$ which is perfectly in agreement with the abovementioned pressure excess ratio analysis presented in Figure 2.15.

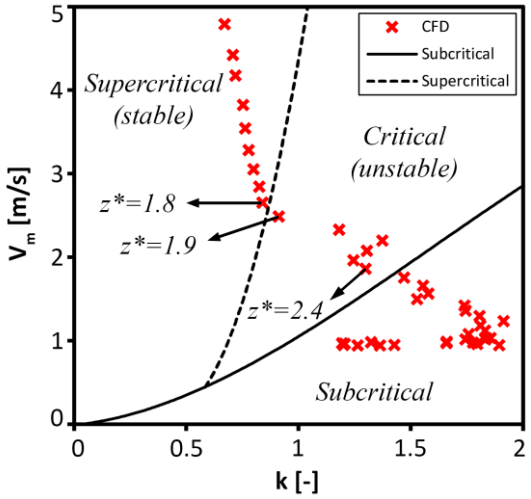

Figure 2.16. Vortex development in accordance with the concept of critical state

Moreover, it is noticed in Figure 2.16 that locations between $z^* = 1.8$ to 2.4 take place in the critical phase which intrinsically suggests that the vortex breakdown occurs frequently at different locations in this range ($z^* = 1.8$ to 2.4) through time. This statement will be comprehensively discussed in the next subsection (section 2.4.1.2). The locations after $z^* = 2.4$ fall in the subcritical state where the vortex dissipates in turbulent vortices.

The evolution of the time-averaged swirl number along z-axis is calculated using equation 2.2 and plotted in Figure 2.17. It is observed that the swirl number is decreased gradually after leaving the swirler and reaches its minimum value in the throat.

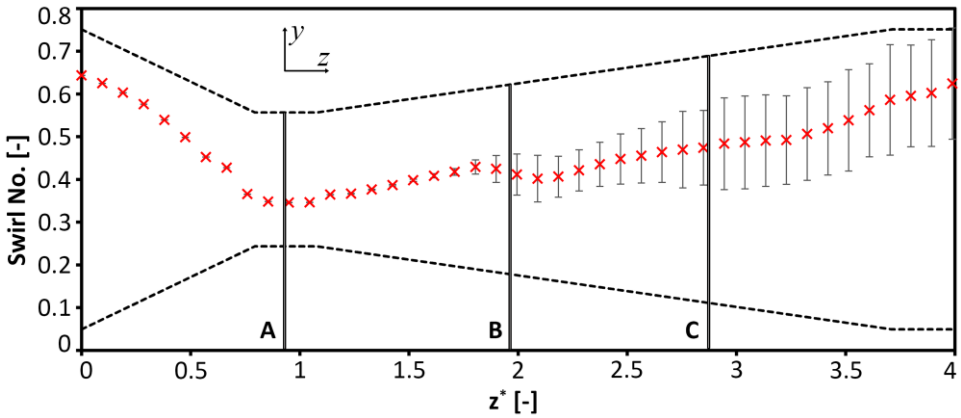

Figure 2.17. Evolution of time-averaged swirl number along the Venturi (z-direction)

It is also noticed that the swirl number experiences a local drop near $z^* = 1.8$. Moreover, the standard deviation of the swirl number in the converging part, the throat and the beginning of

the diffuser is significantly low (near zero) which shows that the flow exhibits a stable behavior. It is observed, however, that the standard deviation at a certain location (around $z^* = 1.8$) increases rapidly which reveals that the flow has entered an unstable mode. The local drop in swirl number along with the increase in the standard deviation conveys that the vortex loses its coherence at this certain location around $z^* = 1.8$. Considering this statement with the beforementioned results presented in Figure 2.15 and Figure 2.16 confirms the time-averaged location of vortex breakdown around $z^* = 1.8$.

It is reported frequently for swirling flows in diffusers that the tangential velocity develops as a function of r^{-1} while the axial velocity develops as function of r^{-2} (representing the cross-section area of the diffuser). Evolution of mean meridional velocity (V_m) and tangential velocity (V_t) in the diffuser is presented against normalized radius (r^*) in Figure 2.18.

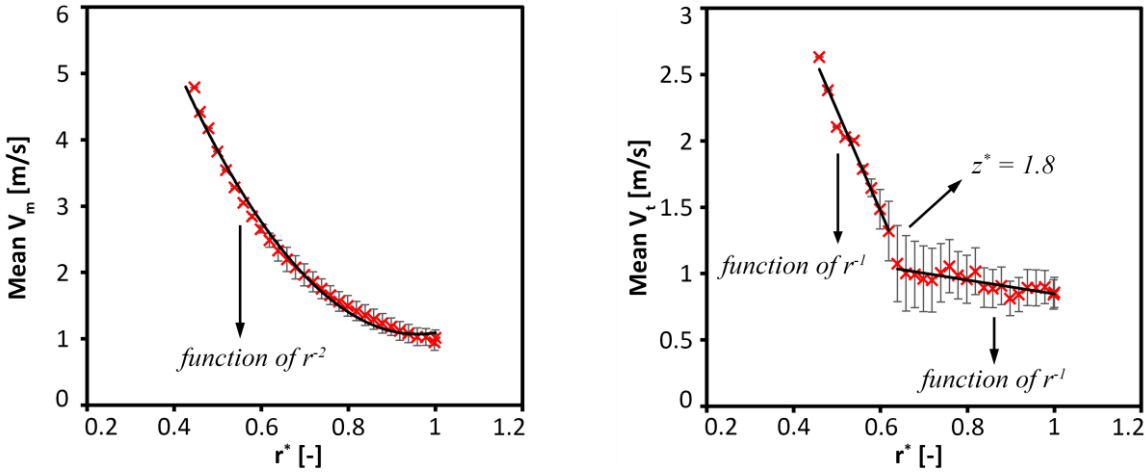

Figure 2.18. Evolution of a. mean meridional (V_m) and b. tangential (V_t) velocities with radius in the diffuser

It is confirmed in Figure 2.18.a that the mean meridional velocity (V_m) decreases in the diffuser with r^{-2}. In addition, the mean tangential velocity (V_t) presented in Figure 2.18.b follows a linear correlation with r^{-1} up to the breakdown location ($z^* = 1.8$), however, it follows another linear trendline with r^{-1} downstream of the breakdown location. It is also observed that the standard deviation of the mean tangential velocity in the diffuser increases extremely downstream of the breakdown location which shows that the swirling flow becomes severely unstable in that region.

In this section, the time-averaged location of the vortex breakdown is estimated by using different techniques based on time-averaged pressure and velocity components. All analyses estimate that the vortex breakdown occurs at $z^* = 1.8$. In addition, these results are in quite good agreement with the experimental results, including pressure fluctuations and high-speed visualization of the vortex shape: the axisymmetric vortex develops downstream of the swirler

and breaks down in the Venturi cone (Figure 2.10) into intermittent helical vortices. In addition, the rotation of these helical vortices generates convective pressure fluctuations in the Venturi cone as discussed in section 2.2.3 (Figure 2.7).

After estimating the time-averaged location of the vortex breakdown in this section, the dynamic behavior of flow near the breakdown location will be fully investigated in the following sections by focusing on cross section B as a reference plane.

2.4.1.2. Axial fluctuation of the vortex breakdown location

It is noticed in the previous section (Figure 2.16) that the vortex falls in the critical phase between z^* = 1.8 to 2.4 and flow shows an unstable behavior in this region, which suggests that the vortex breakdown location may oscillate over time along z^* = 1.8 to 2.4. In this regard, this section focuses on the investigation of the evolution over time of the vortex breakdown location and its possible relation with the development of the low-frequency synchronous pressure pulsations. To identify the accurate time-transient location of the vortex breakdown, the λ_2 criterion is first adopted to analyze the CFD results at different timesteps. Jeong et al. [86] suggested λ_2 criterion as a simple identifying method for vortex core. They decomposed the velocity gradient tensor **J** to its symmetric and antisymmetric parts (the strain-rate tensor **S** and the spin tensor **Ω**, respectively), as in equations 2.11 and 2.12:

$$\mathbf{S} = \frac{\mathbf{J} + \mathbf{J}^{\mathbf{T}}}{\mathbf{2}} \qquad \textbf{2.11}$$

$$\Omega = \frac{\mathbf{J} - \mathbf{J}^{\mathbf{T}}}{\mathbf{2}} \qquad \textbf{2.12}$$

Accordingly, the vortex core is considered as the connected region between two negative eigenvalues of $\mathbf{S^2} + \mathbf{\Omega^2}$ where the eigenvalues are such that $\lambda_1 > \lambda_2 > \lambda_3$. Therefore, a point with a negative λ^2 belongs to the vortex core region. It is however seen in the literature [87, 88] that, for a fully turbulent swirling flow, the near-zero negative values of λ_2 can be associated with turbulent vortices rather than the main vortical structures. Therefore, when using the λ_2 criterion for identifying the vortex core region, it is of great importance to find a valid λ_2 value (low enough to filter the turbulent vortices) by considering the turbulence intensity of the flow field. In the current research, it is confirmed that using an iso-surface of λ_2 = -10,000 [s^{-2}] leads to an estimation of the breakdown location conformed with the presented results in the previous section (time-averaged

breakdown location around $z^* = 1.8$). Thus, iso-surface of $\lambda_2 = -10{,}000$ [s^{-2}] is selected to display the 3D shape of the vortex in Figure 2.19.a. The general configuration of the vortex structure shown in Figure 2.19.a (from CFD) is in agreement with the experimental visualization of the vortex shape presented in Figure 2.10: both figures display three states for the vortex in which an axisymmetric vortex in the Venturi throat breaks down into intermittent helical vortices downstream of the throat.

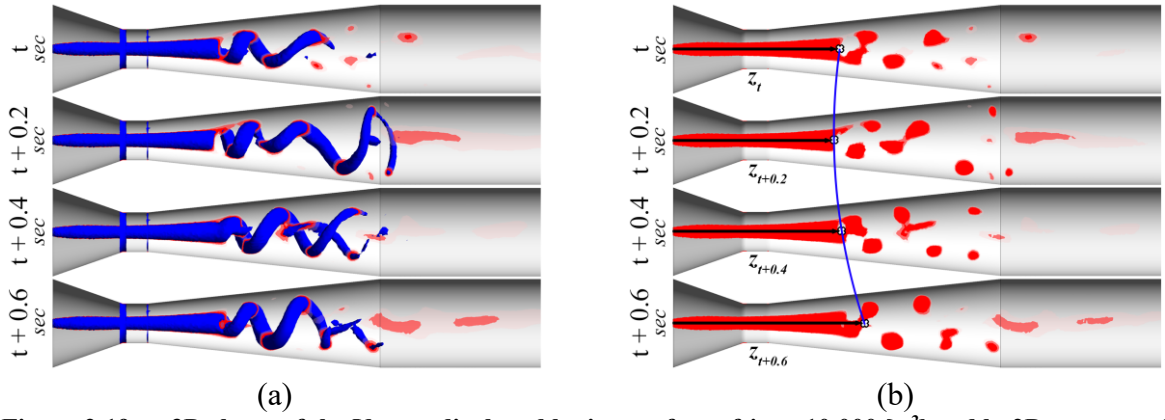

(a) (b)

Figure 2.19. a. 3D shape of the Vortex displayed by iso-surface of $\lambda_2 = -10{,}000$ [s^{-2}] and b. 2D contour of $\lambda_2 = -10{,}000$ [s^{-2}] in the *yz*-plane displaying the breakdown location

To determine the breakdown location on the z-axis at each timestep of CFD simulation, the 2D contour representing $\lambda_2 = -10{,}000$ [s^{-2}] on *yz*-plane (the red region) is used (Figure 2.19.b). The instantaneous location of vortex breakdown is identified as the axial location which is placed on the boundary of the axisymmetric red contour with the white area in Figure 2.19.b. The vortex breakdown locations for different timesteps are connected by the blue curved line in Figure 2.19.b.

This methodology is applied to all CFD simulation timesteps (incl. 600 timesteps for 6 *sec* of simulation) to find the evolution of the breakdown axial location over time as presented in Figure 2.20.a. The FFT of the axial locations of the vortex breakdown is plotted and compared with the FFT of synchronous pressure pulsations at cross section B (near the time-averaged vortex breakdown location) in Figure 2.20.b. This figure presents that the axial location of the vortex breakdown fluctuates with the same range of frequencies as the synchronous pressure component at this cross section in the Venturi cone. This observation suggests that the low-frequency synchronous pressure fluctuations are induced by the unsteady oscillations of the vortex breakdown location in the Venturi cone. The FFT peak corresponding to the fluctuation of the breakdown location covers a range of frequencies (Strouhal numbers between 0 to 1), similar to the experimental results presented in section 2.2.3.

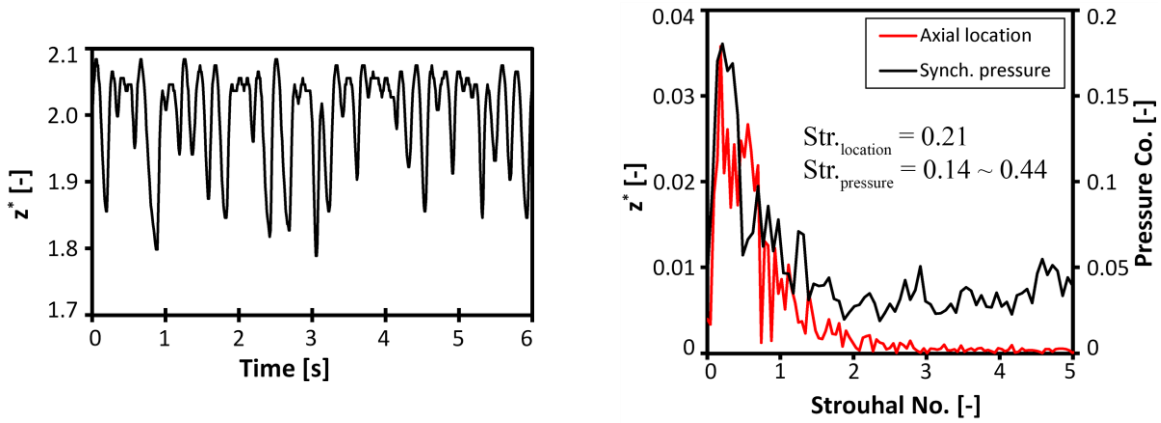

(a) (b)

Figure 2.20. a. Axial location of the vortex breakdown and b. FFT of the breakdown location

Gelfgat et al. [89] numerically investigated the stability of a confined swirling flow (in a cylinder) and showed that the oscillatory instability of the vortex is not a result of the vortex breakdown. They proved that the oscillatory instability starts when the local Reynolds number reaches a critical value determined based on the aspect ratio (height/radius) of the cylinder. Unfortunately, the aspect ratio and the Reynolds number in the present test case are far above their studied values, thus it is not possible to compare the presented results in the current chapter with their methodology. A linear stability analysis of the average flow field in the Venturi cone may be used in future studies to determine the origin of this self-excited oscillatory instability [90-92].

2.4.1.3. Volumetric fluctuations of the stagnation region

The swirl-decay mechanism which is explained in the introduction section (1.2) proposes that the vortex breakdown is accompanied with the formation of a counterflow downstream of the breakdown location. This counterflow is surrounded by a stagnation region, i.e., the axial velocity on the boundaries of the counterflow is zero forming a stagnation region ($V_m = 0$). The breakdown location usually shows a coupling with the stagnation point at the vortex axis. Therefore, in case of unsteady breakdown location, both the breakdown location and the stagnation point should clearly fluctuate together with the same frequency. The relation between the volume of the stagnation region and the breakdown location however has not been clarified yet. This section investigates the fluctuations of the stagnation region volume over time. Using the unsteady CFD results, the stagnation region is displayed in Figure 2.21.a for three selected time instances. Volume of the stagnation region is extracted and shown in Figure 2.21.b for all the timesteps

during 6 seconds of unsteady CFD simulation. The values of volume presented in Figure 2.21 are normalized by the volume of the Venturi diffuser (0.0013 m^3).

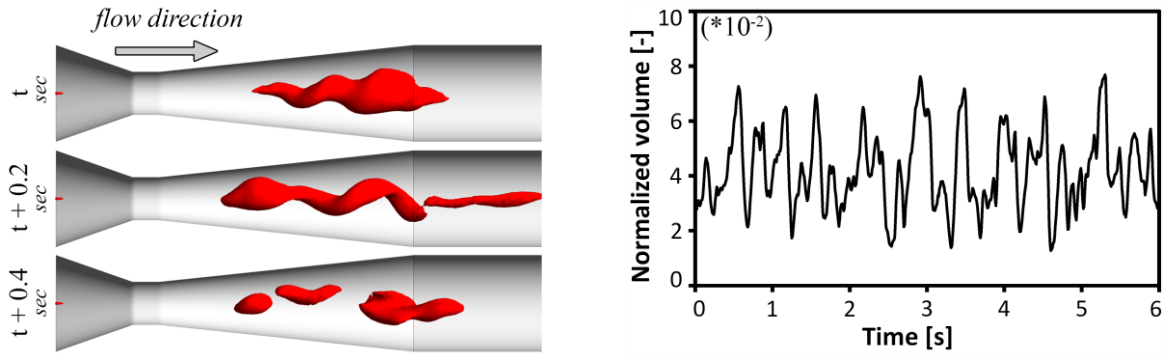

(a) (b)

Figure 2.21. a. Stagnation regions at 3 time-instances (displayed by iso-surface $V_m = 0$) and b. volumetric fluctuation of the stagnation region through time

Figure 2.21.b shows that the volume of the stagnation region oscillates through time. FFT of the stagnation volume is calculated and compared with the FFT of the synchronous pressure pulsations at cross section B in Figure 2.22.

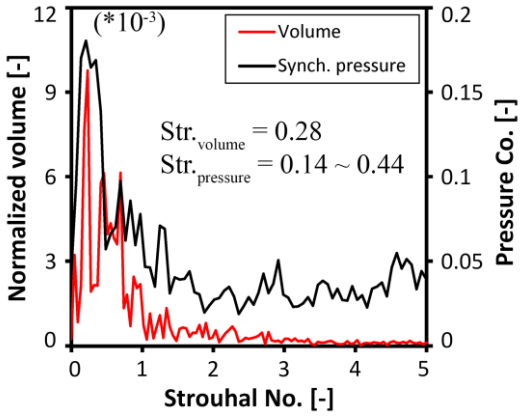

Figure 2.22. FFT of stagnation region volume

Figure 2.22 conveys that the volume of the stagnation region fluctuates with the same frequency as the synchronous pressure pulsations in the Venturi cone. By comparing Figure 2.22 with the results presented in Figure 2.20.b, it can be deduced that the synchronous pressure pulsations are generated by both the axial fluctuation of the breakdown location along with the volumetric fluctuation of the stagnation region. Although, it is seen that there is a strong coupling between the oscillation of the breakdown axial location and the volume of the stagnation region; it is not possible, with the existing results, to determine what instability causes the other.

2.4.1.4. Instantaneous frequency of the breakdown location fluctuation

Considering the fluctuation of the vortex breakdown location presented in Figure 2.20.a, it is noticed that the breakdown location fluctuations feature 24 periods over 6 sec of CFD simulation corresponding to a Strouhal number of 0.556. However, the FFT results plotted in Figure 2.20.b shows that the fluctuations of the breakdown location cover a range of Strouhal numbers between 0 to 1. To investigate the reason for this difference, the instantaneous Strouhal number of fluctuations is calculated using equation 2.13:

$$Str._{inst.} = \frac{f_{inst.}.D^3}{Q} \qquad \textbf{2.13}$$

where the instantaneous frequency $f_{inst.}$ of fluctuations is defined in equation 2.14:

$$f_{inst.} = \frac{1}{\Delta t_{inst.}} \qquad \textbf{2.14}$$

and $\Delta_{tinst.}$ is the period of each fluctuation. The instantaneous Strouhal number of breakdown location fluctuations is presented in Figure 2.23.

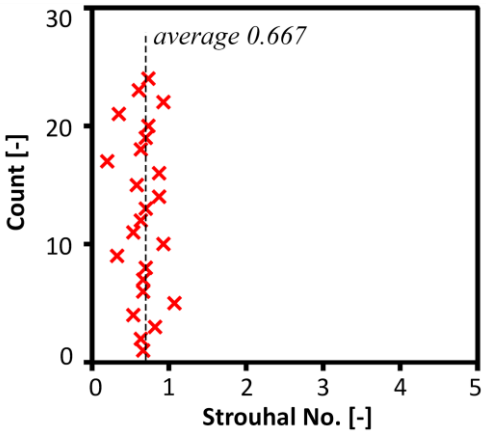

Figure 2.23. Instantaneous Strouhal number of breakdown location fluctuations

Figure 2.23 shows that the fluctuations of the breakdown axial location occur with a variation of the instantaneous Strouhal numbers ranging from 0 to 1 with an average value of 0.667 featuring a standard deviation of 0.194. This result explains the stochastic nature of the vortex breakdown and is in agreement with the beforementioned statements in section 2.3 that the low-frequency synchronous component of the pressure pulsations covers a wide range of Strouhal numbers (Figure 2.8).

2.4.2. Dynamic behavior of flow near the vortex breakdown location and associated vortex characteristics

This section is dedicated to the investigation of the dynamic behavior of the flow close to the vortex breakdown location to understand the mechanisms leading to the formation of the convective pressure component over a wide range of frequencies as shown in Figure 2.7 and Figure 2.8. These results may indicate a stochastic component in the vortex behavior after the breakdown location, which will be confirmed in the following by further analyses of the results in cross section B of the Venturi cone which is located near the breakdown location (at $z^* \approx 2$).

2.4.2.1. Identification of the vortex center

To highlight the vortex breakdown dynamic behavior, the location of its center is estimated by applying the methodology based on the calculation of the Γ_1 function. The dimensionless Γ_1 scaler is a non-Galilean invariant proposed by Graftieaux et al. [93] to accurately identify the vortex center based only on topology of the velocity field. The Γ_1 function, as described in equation 2.15, characterizes the rotation rate of the flow around a certain point by representing the sine of the angle (θ_M) between the velocity vector $\overrightarrow{PM}$ and the radius vector $\overrightarrow{U_M}$:

$$\Gamma_1(p) = \frac{1}{N}\sum_S \frac{(\overrightarrow{PM} \times \overrightarrow{U_M}).\vec{z}}{\left\|\overrightarrow{PM}\right\|.\left\|\overrightarrow{U_M}\right\|} = \frac{1}{N}\sum_S \sin(\theta_M) \qquad \textbf{2.15}$$

where S is a fixed size two-dimensional rectangular zone surrounding the point P (a 5*5 grid is used in this chapter). N is the number of points M which lie in the zone S. Vectors $\overrightarrow{PM}$, $\overrightarrow{U_M}$, and $\vec{z}$ stand for the spatial vector between P and M, the velocity vector at M, and the unit vector normal to the measurement cross section. The Γ_1 reaches to its bound equal to 1 at the location of the vortex center.

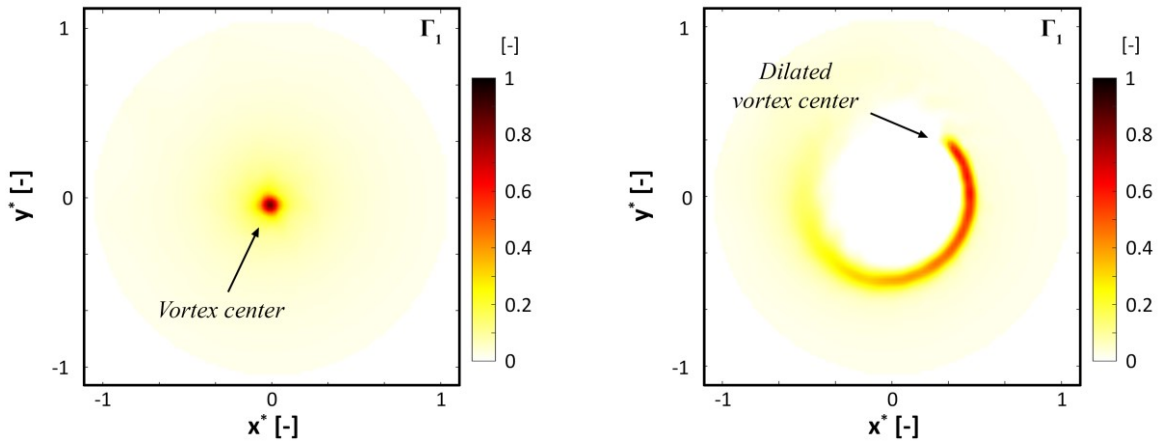

Figure 2.24. Γ_1 function calculated at cross section B for arbitrary timesteps a. *t* and b. *t+Δt*

As presented before in Figure 2.20.a, the vortex breakdown occurs at different locations in time, at upstream and downstream of section B (at $z^* \approx 2$). Therefore, different states of the flow (the axisymmetric vortex, the breakdown, and the helical vortices downstream the breakdown location) can be observed at the fixed cross section B, which is located nearly at the mean location of fluctuations. Figure 2.24 shows examples of Γ1 distribution in section B indicating the vortex centers for two timesteps *t* and *t+Δt* corresponding to the axisymmetric vortex and the breakdown states, respectively.

Figure 2.24.a (timestep *t*) shows that the vortex center is located in the center of the Venturi constituting a structure of an axisymmetric vortex. However, it is noticed in Figure 2.24.b (timestep *t+Δt*) that the vortex center is stretched along the perpendicular plane to its axis near the breakdown location.

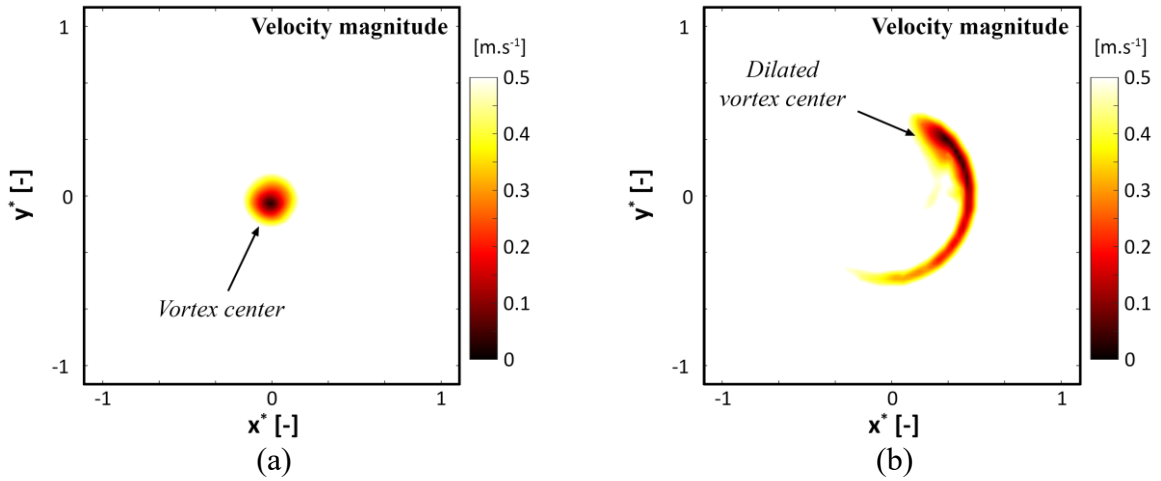

Figure 2.25. Distribution of velocity magnitude at cross section B for arbitrary timesteps a. *t* and b. *t+Δt*

Distribution of the 2D velocity magnitude (*xy*-components) at cross section B is presented in Figure 2.25 for two timesteps *t* and *t+Δt*. It is also interesting to mention that the vortex in both conditions exhibits a zero-velocity magnitude in its center.

2.4.2.2. Spatial stretching (dilatation) of the vortex center

In the previous section, it is showed that the center of the vortex experiences a spatial stretching during its breakdown. This section examines the reasons for this vortex stretching by considering the vorticity transport equation. By taking the curl of the Navier-Stokes equations for a viscous incompressible flow, the vorticity transport equation, which describes the local rotation of flow, is derived as in equation 2.16 [94, 95]:

$$\underbrace{\frac{\partial \vec{\omega}}{\partial t}}_{\text{Temporal change of vorticity per unit volume}} + \underbrace{(\vec{V}.\nabla)\vec{\omega}}_{\text{Spatial change of vorticity (dilatation term) per unit volume}} = \underbrace{(\vec{\omega}.\nabla)\vec{V}}_{\text{Vortex stretching term per unit volume}} + \underbrace{\nu\nabla^2\vec{\omega}}_{\text{Diffusion of vorticity per unit volume}} \qquad \textbf{2.16}$$

Where $\vec{\omega}$, $\vec{V}$, and ν are the vorticity vector, velocity vector, and kinematic viscosity of fluid, respectively.

The vortex stretching term in the right-hand side of equation 2.16 indicates the stretch of a vortex filament along its axis (vortex line) due to velocity gradients, while the dilatation term in the left-hand side describes the spatial stretching (dilatation) of a vortex in a planar direction perpendicular to the vortex axis [49, 96]. The dilatation term is usually induced by fluid compressibility; however, it is probable that for incompressible fluid flows the dilatation term appears due to the high rate of shear strain (usually observed in shear layer swirling flows). In a rotating shear layer flow, high shear strain rate deforms the fluid elements exhibiting a distortion in the flow field. The dilatation terms for two timesteps t and $t+\Delta t$ (the same timesteps as in Figure 2.24) are displayed in Figure 2.26.

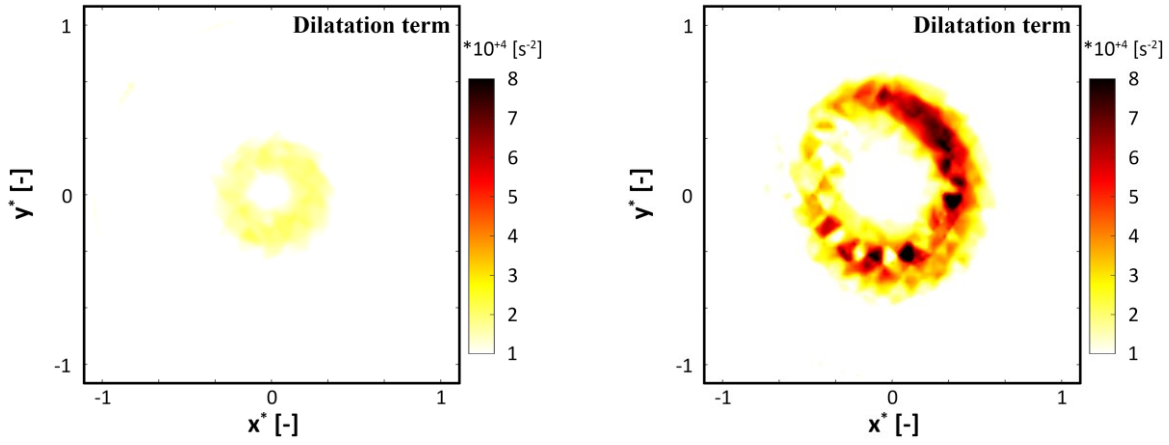

Figure 2.26. The vortex dilatation term at cross section B for arbitrary timesteps a. *t* and b. *t+Δt*

Figure 2.26 reveals that the dilatation term experiences a high increase at timestep $t+\Delta t$ exhibiting the breakdown state of the vortex. Since the Mach number during experiments is 0.0064 < 0.3, the flow can be considered incompressible. Therefore, this increase in the dilatation term should be generated by the shear strain rate. The shear strain rate (at the same timesteps as in

Figure 2.24 and Figure 2.26) is presented in Figure 2.27 confirming that the flow field endures a significantly high increase in the rate of shear strain at the location of breakdown. Consequently, a shear layer is formed around the center of the Venturi that vigorously dilates the vortex center along this layer.

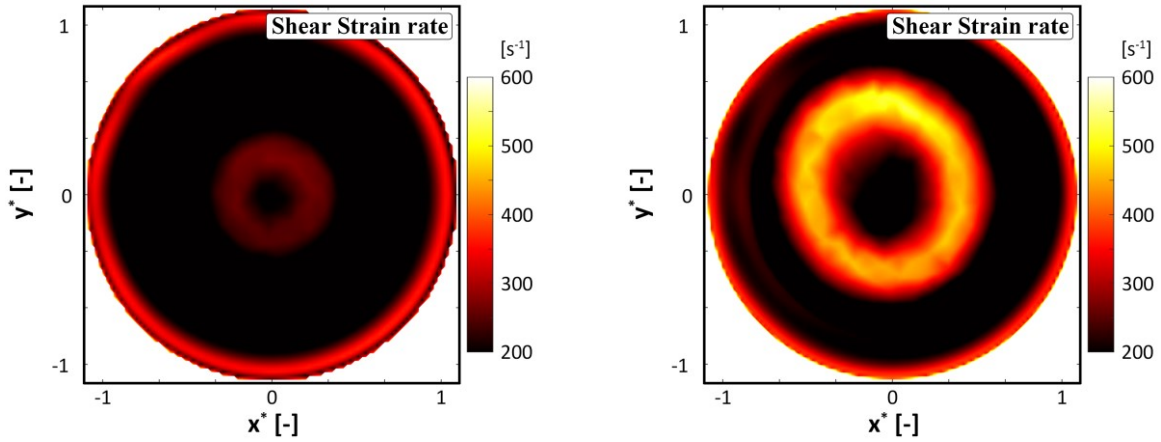

(a) (b)

Figure 2.27. Shear strain rate at cross section B for arbitrary timesteps a. *t* and b. *t+Δt*

2.4.2.3. Vortex dynamic behavior over one cycle of breakdown location fluctuation

In the previous two sections (2.4.2.1 and 2.4.2.2), it is discussed that the flow field at the location of breakdown suffers a shearing deformation that dilates the vortex center in the normal plane to its axis. In this section, the unsteady behavior of the vortex is investigated by analyzing the flow field parameters over one cycle of the breakdown location fluctuation. One fluctuation cycle of the vortex breakdown location and the volume of the stagnation region (selected from Figure 2.20.a, and Figure 2.21.b) is plotted over time in Figure 2.28. The period of the selected cycle is 0.22 sec corresponding to the instantaneous Strouhal number of 0.631 (roughly equal to the average value in Figure 2.23). It is noticed in Figure 2.28 that the vortex breakdown location moves in an opposite phase with the volume of the stagnation region. This confirms the existing coupling between the fluctuation of the breakdown location with the volume of the stagnation region.

To capture the evolution of the vortex breakdown (from an axisymmetric vortex state to fully broken vortex state), five timesteps shown in Figure 2.28 are selected such that t_0 and t_4 correspond to the axisymmetric vortex (upstream the breakdown), t_1 and t_3 belong to the states very close to the breakdown location, and t_2 is located downstream of the breakdown. To improve the image of the selected timesteps (t_0 to t_4), the breakdown location with respect to cross section

B is schematically shown in Figure 2.29. The breakdown location is indicated by purple cross signs in Figure 2.29. It is important to mention that the demonstrated vortex structure in Figure 2.29 is simplified. The reader may refer to Figure 2.30.e to see the original vortex structure from CFD results.

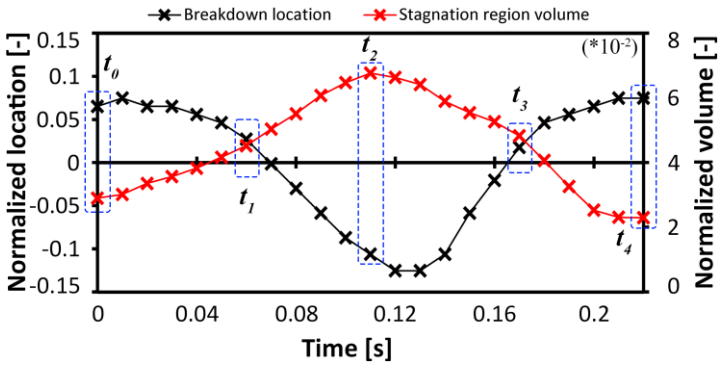

Figure 2.28. Variation of the breakdown location and stagnation region volume for one period of vortex breakdown

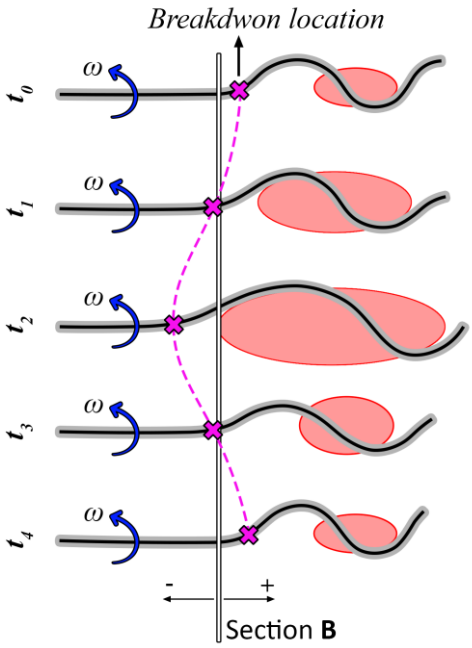

Figure 2.29. Schematic location of the vortex breakdown with respect to section B

The flow field characteristics at cross section B (for the selected timesteps corresponding to different states of the vortex as demonstrated in Figure 2.29) are presented in Figure 2.30. The results shown in Figure 2.30 include (a) the Γ_1 distribution, (b) distribution of the dilatation term,

(c) distribution of the shear strain rate, (d) meridional velocity V_m distribution, and (e) 3D shape of the vortex (blue) along with the stagnation region (red).

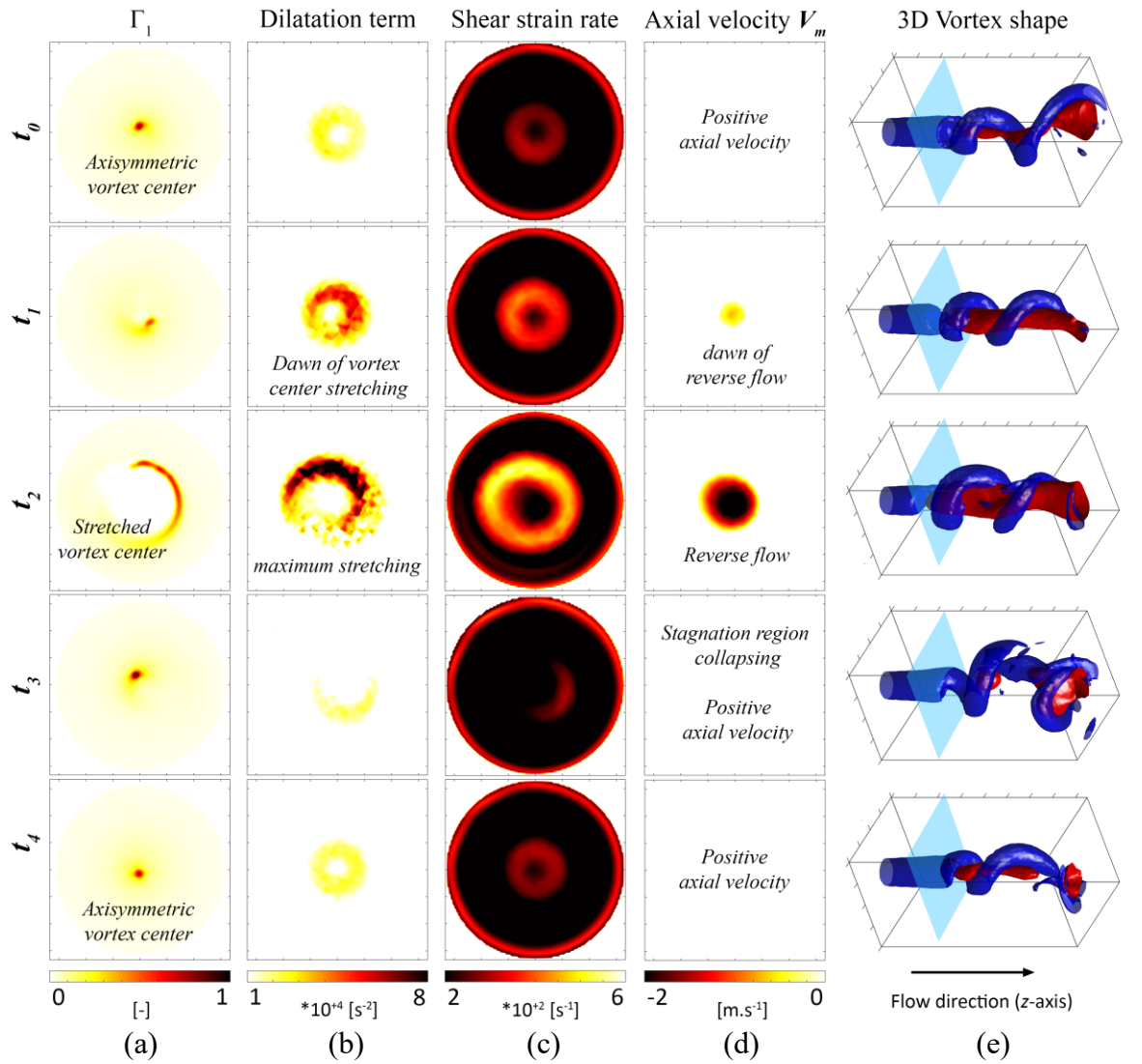

Figure 2.30. a. Γ_1 distribution, b. distribution of the dilatation term, c. distribution of the shear strain rate, d. meridional velocity V_m distribution, e. 3D shape of the vortex displayed by iso-surface of λ_2 = -10,000 [s^{-2}] (blue) and the stagnation region (red) for five timesteps during one cycle of the vortex breakdown displayed on cross section B.

Distributions of Γ_1, dilatation term and shear strain rate at cross section B shown in Figure 2.30.a, b, and c, respectively, confirms the statement in section 2.4.2.2 that the vortex center deforms from a very axisymmetric shape upstream of the breakdown (t_0) to a dilated shape downstream of the breakdown (t_2). By comparing this with the distribution of the meridional velocity (V_m) in Figure 2.30.d, it is seen that the onset of this deformation occurs at t_1 where the stagnation region moves axially-backward in section B. The volume of the stagnation region reaches to its maximum level at t_2 (see Figure 2.28 and Figure 2.30.d) where the maximum deformation in shape of the vortex center is observed (Figure 2.30.a). It suggests that the growth of the stagnation region at t_1 and t_2 pushes the vortex center outward the Venturi center. This

severe condition significantly increases the shear strain rate and forms a shear layer over the stagnation region. The fluid elements in the shear layer suffers a distortion causing the dilatation in the vortex center.

In addition, it is observed that while the breakdown location is moving downstream of section B (at t_3) the stagnation region vanishes and causes a sudden decrease in the dilatation term which forces the breakdown location to move back downstream of section B at t_4. The sudden retreat of the stagnation region conveys that the stagnation region collapses at t_3. This abrupt collapse of the stagnation region provokes disturbances in the flow field just downstream of the breakdown location (for example see Figure 2.30.e at t_3). Figure 2.30.e also shows that the vortex structure is wrapped on the stagnation zone which is in agreement by the vortex configuration proposed by Nishi et al. [97, 98]. Investigating the flow field after the collapse of the stagnation region reveals that the downstream disturbances are accompanied with appearance and disappearance of small vortical structures which rotate with stochastically different frequencies in the Venturi. The random behavior of these small vortices confirms the stochastic nature of the swirling flow after the breakdown location, which may explain the wide range of frequencies observed for the convective component of pressure fluctuations presented in Figure 2.8 (type II in cross sections B and C).

In the current research, a pure periodic rotation of a helical vortex is not identified after the breakdown. Therefore, it is not possible neither to confirm nor to question the influence of the stretching-compressing behavior of the helical vortex on generation of the low-frequency synchronous pressure pulsations (as introduced in the previous works mentioned in the introduction, section 1.2). However, this explanation and the one proposed in this chapter are not conflictive. It can be speculated that the fluctuations of the vortex breakdown location may induce a spring-like stretching-compressing movement along the rotating helical vortices generated downstream the breakdown.

2.5. Summary

This chapter aims at investigating the generation mechanisms of a low-frequency synchronous pressure pulsations in a simplified draft-tube geometry (a Venturi and a swirl generator installed at the upstream). In particular, the relation between the self-induced oscillation of the vortex breakdown location and the low-frequency synchronous pressure pulsations

observed in experiments is investigated in detail by analyzing the experimental and unsteady-state CFD results.

Calculation of FFT over results of experimental pressure measurements at different operating flowrates demonstrates two pressure peaks covering different ranges of frequencies. The CSD analysis of the pressure fluctuations shows that the pressure fluctuations with lower frequencies feature a synchronous nature and propagate in the complete test rig; however, the high-frequency pressure fluctuations show a convective nature and are only identified in the Venturi cone. This reveals that two different phenomena are responsible for the generation of these two types of pressure fluctuations.

High-speed visualization of the vortex in cavitation condition shows that the vortex shape is composed of three distinct states, including: 1. an axisymmetric vortex, 2. vortex breakdown, and 3. intermittent generation of helical vortices downstream of the breakdown location. It is noticed that the location of the vortex breakdown fluctuates axially over time which suggests that the axial fluctuation of the breakdown location may be responsible for the generation of the low-frequency synchronous pressure pulsations in the system.

One operating point in cavitation-free condition is selected for unsteady-state CFD simulations. Based on CFD results, the time-averaged location of the vortex breakdown is estimated using three different analytical methods. All three methods predict the same time-averaged location for vortex breakdown. The time-transient location of the breakdown along with the volume of the stagnation region induced by the counterflow downstream of the breakdown are then extracted from CFD results. FFT analysis of the results shows that both the breakdown location and the volume of the stagnation region fluctuate with the same frequency as the low-frequency pressure pulsations. It implies that the fluctuations of the breakdown location which shows a strong coupling with volumetric fluctuation of the stagnation zone are responsible for the generation of the low-frequency pressure pulsations in the system. Investigation of the instantaneous frequency of breakdown location fluctuations shows that the breakdown location fluctuates within a range of low frequencies (corresponding to Strouhal numbers 0 to 1) revealing the stochastic nature of the phenomenon.

Further analysis of the CFD results shows that the volume of the stagnation region fluctuates in an opposite phase with the breakdown location. It is shown that the stagnation region advances toward the breakdown location while its volume is increasing, then it collapses when the breakdown location moves to downstream. Periodic occurrence of this fact increases the shear strain rate at the location of breakdown. The high rate of shear strain at the breakdown location stretches the vortex center along the perpendicular plane to its axis. Sudden collapse of the

stagnation region in each period generates one or several helical structure(s) downstream of the breakdown location. The stochastic rotation of these helical structure(s) induces convective pressure fluctuations in the diffuser which cover a wide range of frequencies.

The low-frequency oscillations of a vortex generating synchronous pressure pulsations in the hydraulic system are frequently reported in the literature as an important type of vortex-induced instabilities in the draft-tube of hydro-turbines. The current chapter proposes that an unstable breakdown of the vortex may induce this type of vortex oscillations. The presented results in this chapter can be integrated with the previous reports in the literature to hypothesize the generation mechanism of this phenomena: the observed unsteady fluctuations of the vortex breakdown location may induce a stretching-compressing evolution of the rotating helical vortices developed downstream of the breakdown, and thus generation of the low-frequency pressure pulsations in the diffuser as a consequence.

3. Cavitation surge characteristics under different swirl intensities

3.1. Preface

This chapter focuses on cavitation surge characteristics under different swirl intensities using experimental results. Three stationary-blades swirl generators are designed by the authors to generate uniform swirling flows downstream; and a Venturi-tube (comprising a converging, a throat, and a diffuser parts) is selected as the test case which resembles a simplified draft-tube geometry of a hydraulic turbine. The experiments are conducted for four swirl configurations with different swirl numbers conforming with the flow field in the draft-tube during high-load operation of a hydraulic turbine. Dynamic pressure measurements are conducted to identify the frequency spectrum of pressure fluctuations in the draft-tube. The 1st natural frequency of the draft-tube and a transition from stable to unstable modes of pressure fluctuations in the draft-tube are identified. The transition mechanism from stable to unstable modes is elucidated. High-speed visualization of cavitation is performed to capture the cavity volume and its fluctuations in time domain. Several correlations between the natural frequencies of the hydraulic circuits and other parameters (cavitation number, void fraction, etc.) are established. 1D modelling is conducted to predict the wave speed and 1st natural frequency of the draft-tube. The results of 1D modelling are compared with the results of pressure measurements and cavity visual processing.

3.2. Description of the test case

The same test rig as in the previous chapter is employed to study the cavitation surge characteristics. The test rig, which is explained in section 2.2.1 and Figure 2.1, consists of the upstream and downstream tanks, the upstream and downstream straight pipes, a swirler, and a Venturi. The diffuser part of the Venturi-tube resembles the draft-tube of hydraulic turbines (Figure 2.3). The cavitation number, as defined in equation 2.1, can be adjusted in the draft-tube by using a vacuum pump connected to the downstream tank.

3.2.1. Swirl generators

The experiments are conducted using four swirl intensities, amongst them, one condition features no-swirl condition. A uniform axisymmetric swirl is generated for the other three conditions by using three swirlers shown in Figure 3.1.

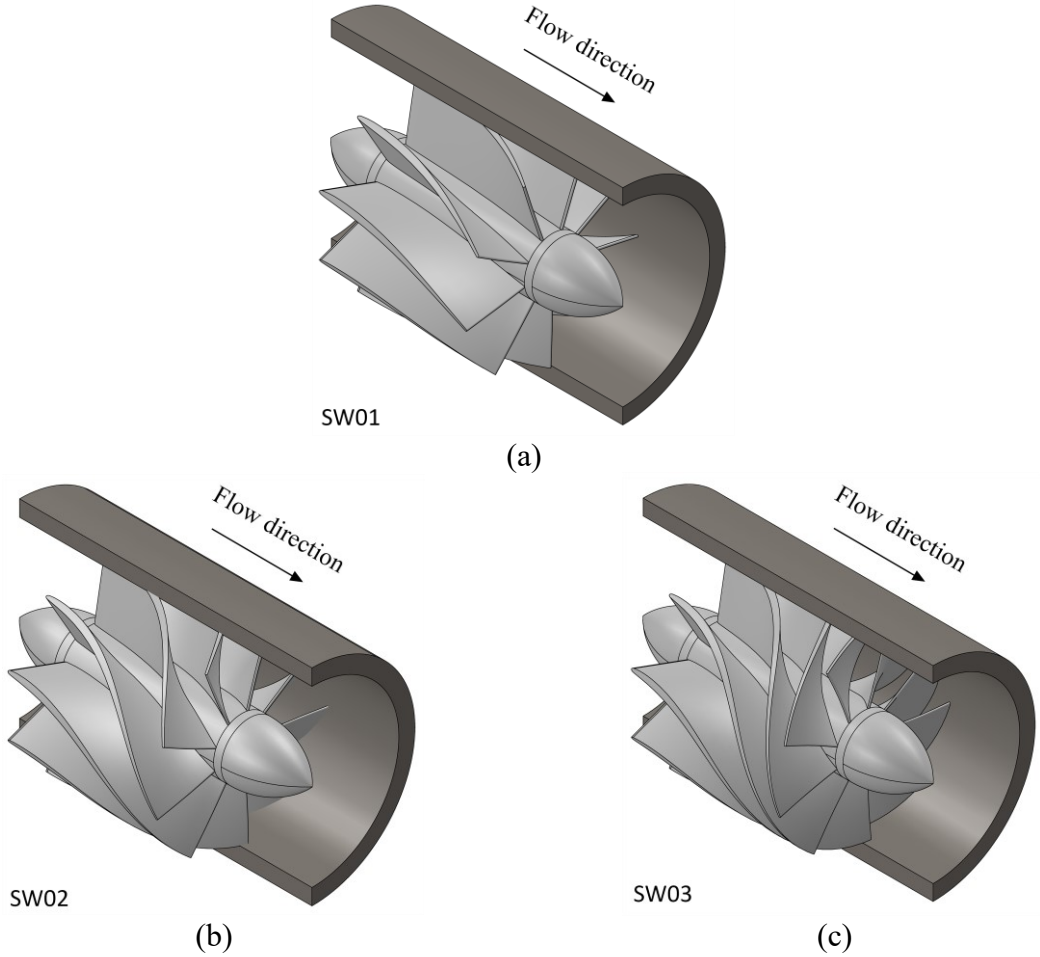

Figure 3.1. 3D geometry of three swirlers

LDV measurements are performed in the throat of the Venturi (upstream of the draft-tube) to measure the swirl intensities at the draft-tube inlet. The meridional and tangential velocity profiles obtained for each swirler is presented in Figure 3.2.

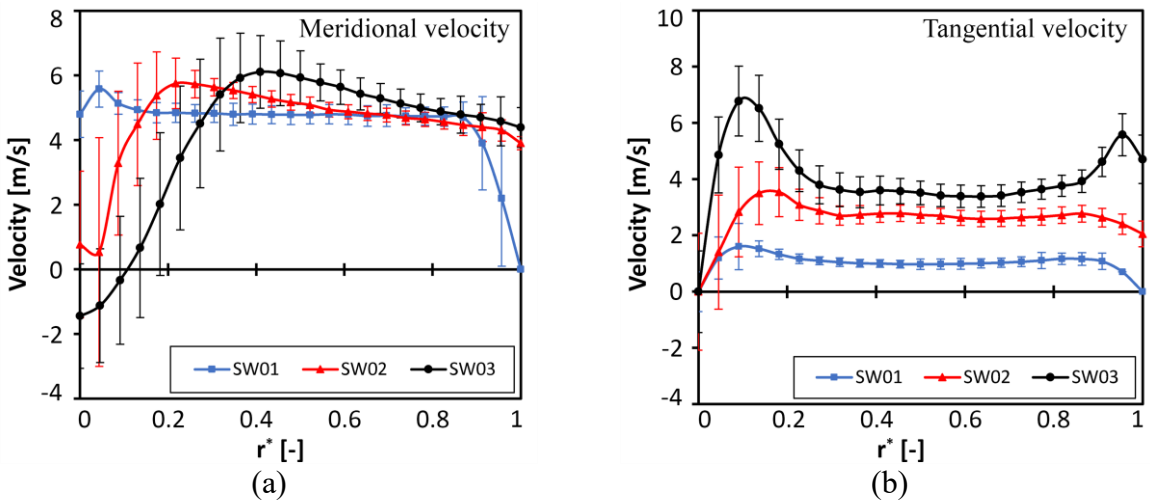

Figure 3.2. Comparison of a. meridional and b. tangential velocity profiles for three swirlers (LDV measurements)

Figure 3.2 shows that each swirler generate a different level of swirl intensity in the draft-tube. Swirl number for each swirler is calculated using equation 2.2 in section 2.2.1 [26, 65], and presented in Table 3.1. Swirlers are named from SW00 to SW03 featuring no-swirl to high swirl intensities. With considering the axisymmetric shape of the generated vortices and their swirl intensities (Table 3.1), it can be speculated that the swirl configurations during the current experiments correspond to the flow field during high-load operation of hydraulic turbines (see Table 2.1).

Table 3.1. Swirl number calculated for each swirler

Swirler	Swirling level	Swirl No. in the throat [-]
SW00	No-swirl	0
SW01	Low swirl	0.14
SW02	Medium swirl	0.35
SW03	High swirl	0.52

3.2.2. Pressure measurements

Dynamic pressure measurements are carried out at 7 sections from the upstream tanks to the downstream tank using 11 wall flush-mounted pressure sensors (similar to the previous chapter). The upstream and downstream pressure sensors are located far upstream and downstream of the Venturi at $P_{upstream}$ and $P_{downstream}$, respectively, as shown in Figure 2.1. Three sections are located in the Venturi to observe the local behavior of the vortex (shown in Figure 2.3). The pressure fluctuations are recorded for 100 seconds of operation to obtain accurate results for calculation of frequency spectrum. The experiments are conducted for all swirlers (presented in Table 3.1) for over 600 operating points (with variation of flowrate and cavitation number). The operating flowrates for all swirlers are from 300 to 1,000 *L/min* with 100 *L/min* intervals (8 flowrates). The cavitation numbers for each operating flowrate varies from the maximum achievable cavitation number to the minimum achievable values. The operating points are shown in Figure 3.3. The maximum achievable cavitation number is shown by black-dashed line. And the limit of cavitation onset for each swirler is shown in colored dot-lines.

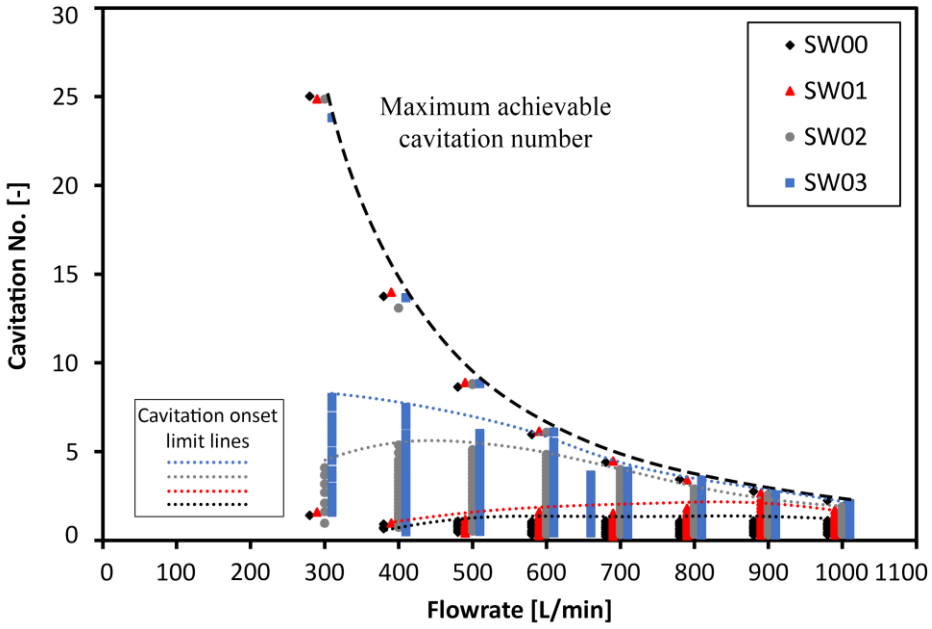

Figure 3.3. Operating conditions

3.2.3. Influence of Dissolved Oxygen (DO) level on pressure measurements

It is reported frequently in the literature that the level of air content in water affects the cavitation characteristics thus the hydroacoustic characteristics of the hydraulic system [99-103]. The air content in water is proportional to level of Dissolved Oxygen (DO), therefore DO level is usually used to introduce the air content in water. Before conducting the experiments, implementing a proper deaeration process is necessary to decrease the influence of DO level on cavitation characteristics. In the current research, deaeration is performed with two flowrates, for $Q = 400$ and 700 *L/min*. For both flowrates, the test rig is operated for a long period of 120 *min* at the minimum cavitation number ($\sigma \approx 0.3$) while the vacuum pump continuously works to remove air from the downstream tank for the whole period. Water samples are taken from the downstream tank in 15-*min*, or 30-*min* intervals; and the DO level is measured using a Hanna edge HI-764080 digital polarographic DO meter (range: 0.00 to 45.00 *ppm*, resolution: 0.01 *ppm*, and accuracy: ±0.01 *ppm*). Variation of DO level with time is shown in Figure 3.4 for both operating flowrates.

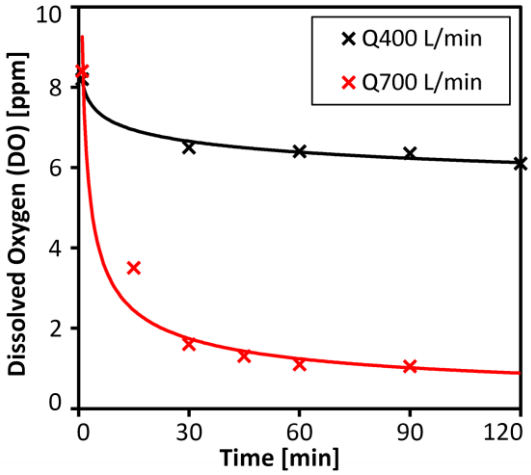

Figure 3.4. Reduction of Dissolved Oxygen (DO) level by time

Figure 3.4 shows for both flowrates that the DO level is decreased exponentially in time and reaches a constant asymptotic level after ≈30 minutes. However, DO level at the asymptotic line for each flowrate is different, 6.3 *ppm* for $Q = 400$ *L/min* and 1.2 *ppm* for $Q = 700$ *L/min*.

To understand the influence of DO level on vortex-induced pressure fluctuations, FFT of pressure fluctuations in cross-section B is computed and presented in Figure 3.5. The amplitudes of FFT are normalized as pressure coefficient as defined in equation 2.6.

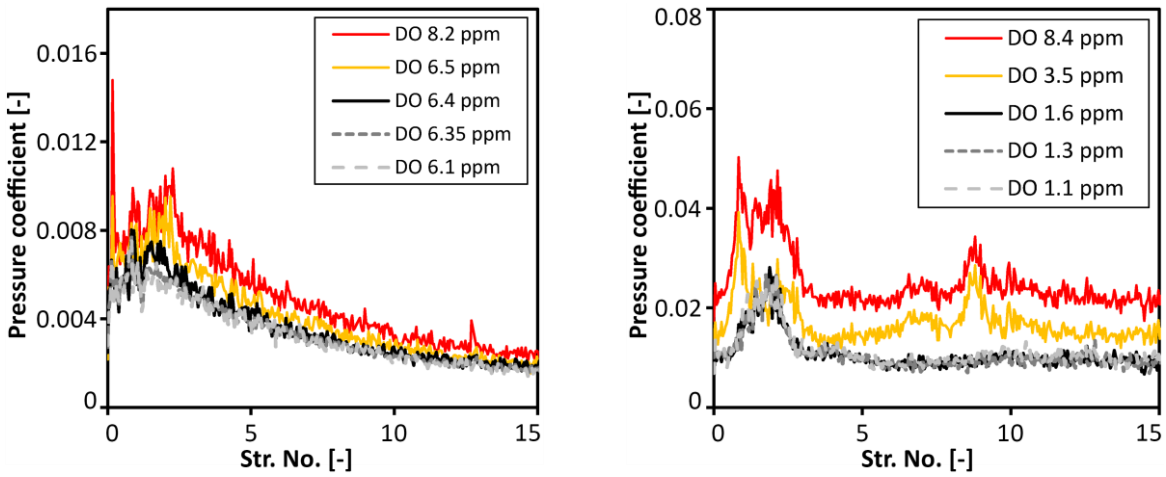

Figure 3.5. FFT of pressure fluctuations in cross-section B for different DO levels for a. $Q = 400$ *L/min*, and b. $Q = 700$ *L/min*

It is noticed in Figure 3.5 that the frequency spectrum from FFT converges to the same results when the DO level reaches close to the constant asymptotic level (≈6.4 *ppm* and ≈1.6 *ppm* for $Q = 400$ and 700 *L/min*, respectively).

With considering the results presented in Figure 3.4 and Figure 3.5, it is assumed that the cavitation characteristics are independent from dissolved oxygen for DO values less than 2 *ppm*. Therefore, it is tried to keep the DO level below 2 *ppm* (in most of cases around 1.2 *ppm*) for the whole range of operating conditions.

3.2.4. Visualization of cavitation volume

A high-speed camera (Photron FASTCAM mini AX-series) with a 50-*mm* lens is used to capture cavitation for further computation of the average volume of cavity and its fluctuations at each operating condition. Arrangement of the high-speed camera with respect to the Venturi is shown in Figure 3.6. A white LED panel is placed behind the Venturi while the camera is installed in front of the Venturi facing to the LED panel.

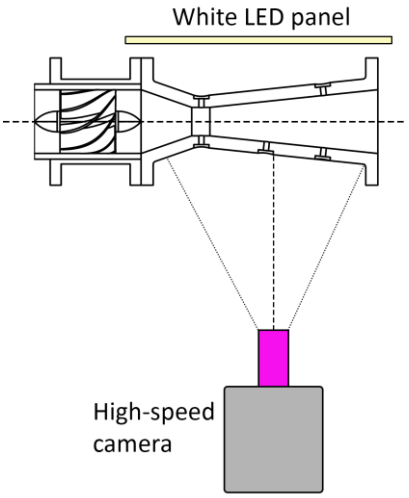

Figure 3.6. Arrangement of the high-speed camera

By adopting the configuration presented in Figure 3.6, the cavity volume can be clearly captured as black shadows showed in Figure 3.7. The cavity fluctuations for each operating condition are captured for 6 seconds (1,000 *fps*) with 1024*512 pixels resolution.

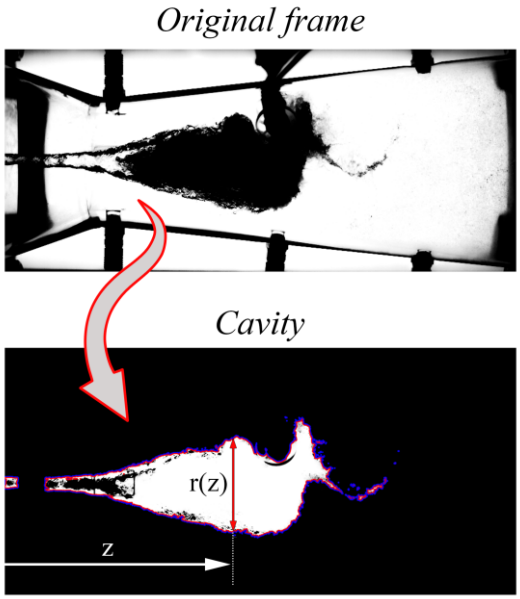

Figure 3.7. Visual processing of the original video frames to extract the cavity volume (SW02, Q=900 *L/min.*, σ=1)

All videos are processed to catch an unobstructed vision on the cavitation volume. A binary filter is applied to all the video frames to convert the cavity volume into white. For each time frame, cavity radius $r(z)$ is computed as a function of the axial location (z). With assuming an axisymmetric shape for the cavity (it is assumed that the cavity at each of its cross-sections have a circular shape), cavity volume is computed for each time frame using equation 3.1:

$$Volume_{cavity} = \int_{0}^{1024} \pi . r(z)^2 . dz \qquad \textbf{3.1}$$

where dz is the actual length of each pixel in the image. The integration in equation 3.1 is done for the limit of 0 to 1024 which corresponds to the number of pixels in the axial direction of each frame.

This formulation for calculating the cavity volume may have some errors since the cavity shape is not perfectly axisymmetric in practice. To capture the cavity volume more accurately, it is necessary to employ two high-speed cameras facing to the Venturi with 90 degrees difference in their direction of view. However, doing so is not feasible with the current state of the test rig which is used for this research.

To generalize the results, the cavity volume is normalized as the void fraction (β) by using equation 3.2:

$$\beta = \frac{Volume_{cavity}}{Volume_{draft-tube}} * 100 \qquad \textbf{3.2}$$

where draft-tube volume is 0.0013 m^3. For instance, evolution of cavity void fraction fluctuations and its mean value is obtained from visual processing and shown in Figure 3.8 for 6 *sec* of operation (swirler SW02 and operating point at Q = 900 *L/min*., σ = 1).

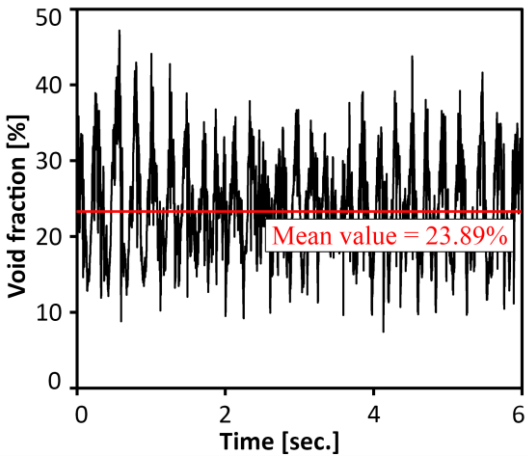

Figure 3.8. Evolution of cavity void fraction in time (SW02, Q = 900 *L/min.*, σ = 1)

The cavity void fraction is calculated for all the operating conditions with four swirlers. The results of which will be presented in the next section (3.3).

It is very well known that cavity volume should be increased by decreasing the cavitation number. Evolution of cavity shape and volume by decreasing cavitation number is presented in Figure 3.9 for SW02 and Q = 900 *L/min* from no-cavitation condition to minimum achievable cavitation number. It is seen in Figure 3.9 that cavitation appears at a certain cavitation number called cavitation onset transition (here $\sigma \approx 2.6$). Then the cavity volume increases by decreasing cavitation number until it experiences a second transition into full-cavitation condition at $\sigma \approx 1.4$. The second transition into full-cavitation condition can be identified by observation of severe noises and vibrations in the hydraulic system. It is also noticed that the cavity preserves its axisymmetric shape for all the cavitation numbers. The same behavior and transitions from no-cavitation to full-cavitation condition is observed for all operating flowrates with all swirlers.

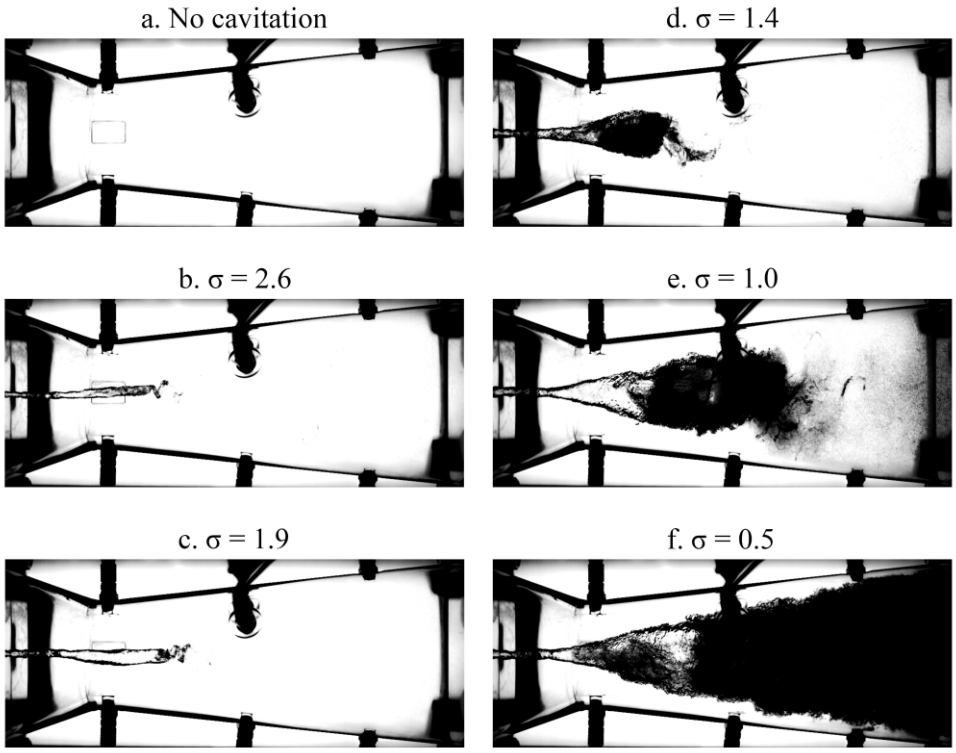

Figure 3.9. Evolution of cavity shape and volume by decreasing cavitation number (SW02, *Q*=900 *L/min*)

3.3. Results and discussions

Using the explained methods in the previous section (3.2), cavitation surge characteristics will be investigated in the current section.

3.3.1. Correlation of pressure drop with cavitation number

First of all, pressure drop in the hydraulic system from upstream tank to the downstream one will be studied in this sub-section. The pressure drop coefficient is calculated by equation 3.3:

$$\Delta P^* = \frac{P_{upstream} - P_{downstream}}{\frac{1}{2}\rho V_{m,up.}^2} \qquad \textbf{3.3}$$

where $P_{upstream}$ and $P_{downstream}$ are mean pressure at upstream and downstream pipes, respectively, as shown in Figure 2.1. And ρ and $V_{m,up.}$ are water density and meridional velocity in upstream pipe, respectively.

Pressure drop coefficient is plotted for all swirlers in Figure 3.10. It is seen for each swirler that the pressure drop coefficient follows the same trend for all flowrates. This conveys that pressure drop coefficient in the hydraulic system does not depend on flowrate.

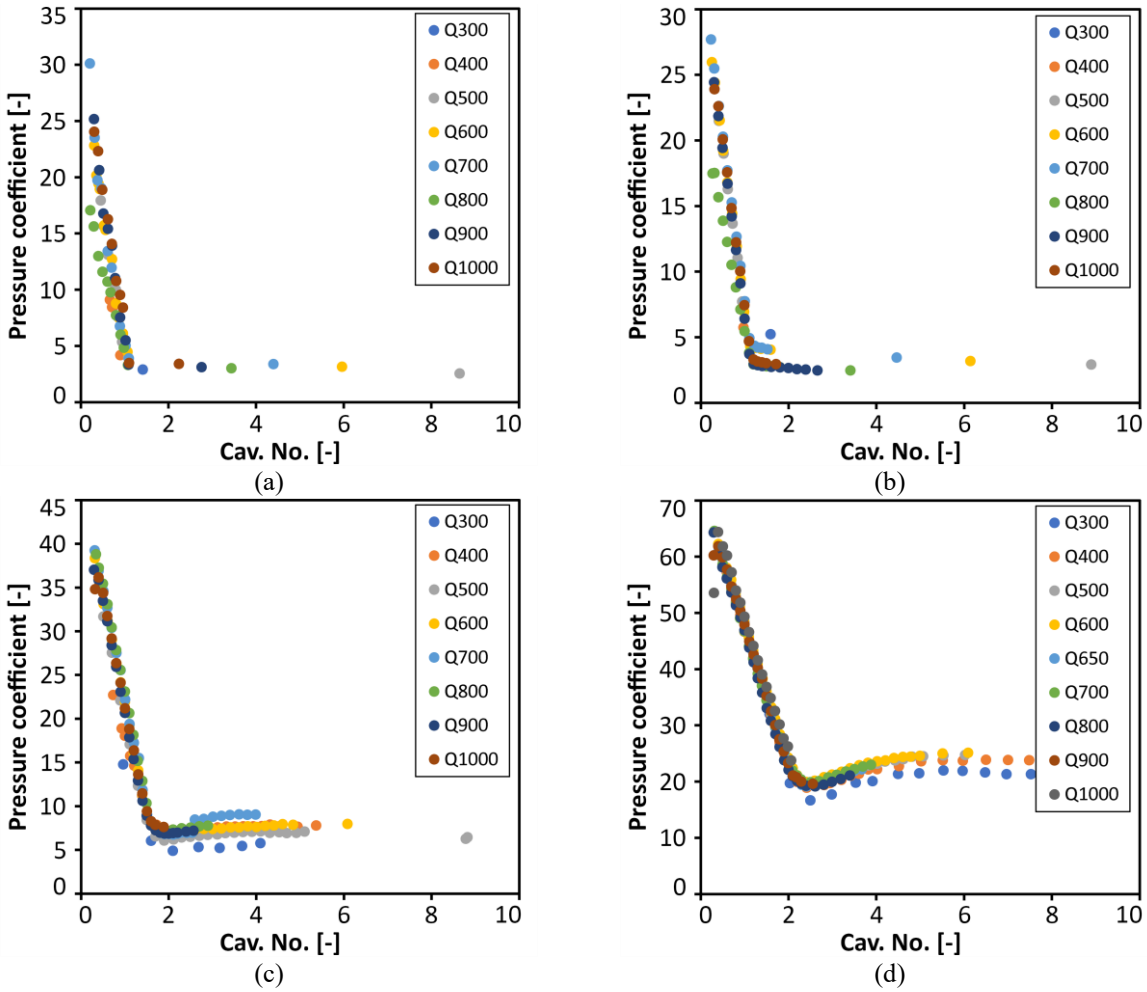

Figure 3.10. Pressure drop coefficient for different flowrates for a. SW00, b. SW01, c. SW02, and d. SW03

Pressure drop coefficient is compared for all swirlers in Figure 3.11.a. It is noticed in Figure 3.11.a that pressure drop coefficient for each swirler feature three stages: a. a constant stage for no-cavitation conditions, b. a non-linear stage for the operating points featuring intermittent

cavitation rope, and c. a linear stage for the full-cavitating conditions. Two transitions as shown in Figure 3.9 are plotted in black lines in Figure 3.11.a During the third stage (full-cavitation condition), the pressure drop coefficients follow a linear trendline as shown in Figure 3.11.b.

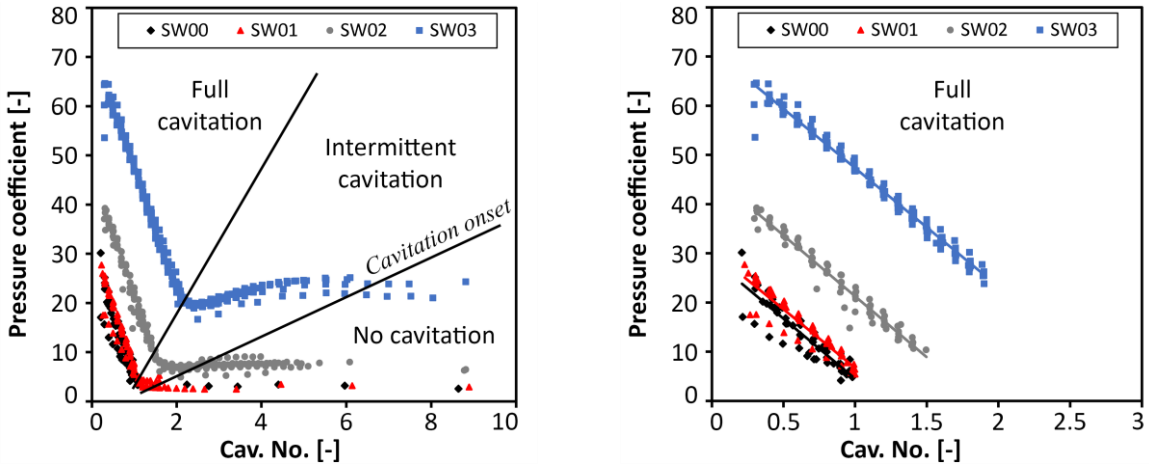

Figure 3.11. Correlation of pressure drop coefficient with cavitation number a. whole range from no-cavitation to full cavitation, and b. full cavitation

Four linear correlations between pressure drop coefficient and cavitation number is established for four swirlers and presented in Table 3.2. It is noticed that the pressure drop coefficient for all swirlers follow the same slope (average slope of -24.29) with however different *y*-intercepts. Higher *y*-intercept for SW02 reveals that pressure drop increases by increasing swirl intensity of flow.

Table 3.2. Linear correlations between pressure drop coefficient and cavitation number for different swirlers

Swirler	Linear correlation	Slope	R^2	*y*-intercept
SW00	$\Delta P^* = -24.44\sigma + 28.953$	-24.44	0.82	28.953
SW01	$\Delta P^* = -23.80\sigma + 30.534$	-23.80	0.87	30.534
SW02	$\Delta P^* = -24.82\sigma + 46.077$	-24.82	0.96	46.077
SW03	$\Delta P^* = -24.01\sigma + 71.402$	-24.10	0.98	71.402

The *y*-intercept is plotted against swirl number in Figure 3.12. Figure 3.12 shows that *y*-intercept increases with swirl number in a 2nd order parabolic function. It shows that the pressure drop coefficient during full-cavitating operating conditions can be simply computed using a linear correlation (as in Table 3.2) and a parabolic function for prediction of the *y*-intercept based on swirl number (similar to Figure 3.12).

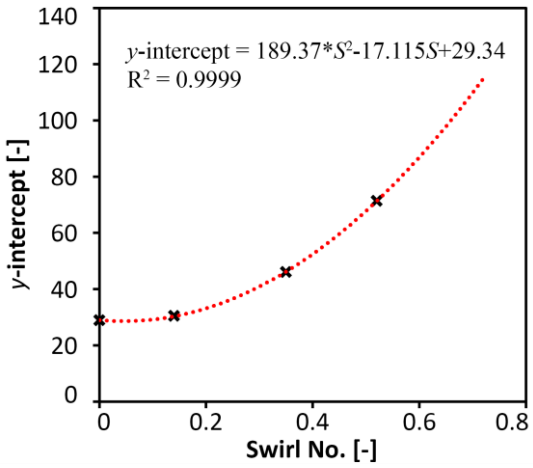

Figure 3.12. Correlation of *y*-intercept (for prediction of pressure drop coefficient) with swirl number

3.3.2. Development of mean cavity volume with cavitation number

Mean cavitation volume is obtained by using the visualization method explained in section 3.2.4. The corresponding void fraction for each operating condition is computed by equation 3.2 and plotted against cavitation number in Figure 3.13. It is noticed in Figure 3.13 that for each swirler the void fraction values for all flowrates fall in the same trendline (similar to what is observed in Figure 3.10 for pressure drop coefficient). Figure 3.13 conveys that the cavity volume can be characterized based only on cavitation number and swirl intensity in the draft-tube inlet.

It is also seen in Figure 3.13 that the void fraction remains zero (or near zero) for high cavitation numbers. However, at a certain cavitation number, for each swirler, void fraction starts increasing exponentially with decreasing the cavitation number.

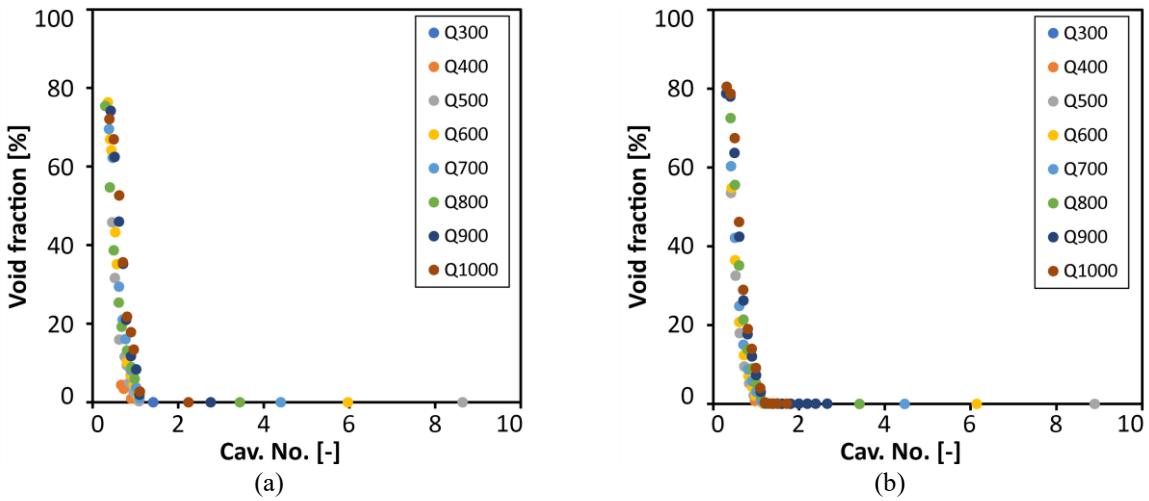

(a) (b)

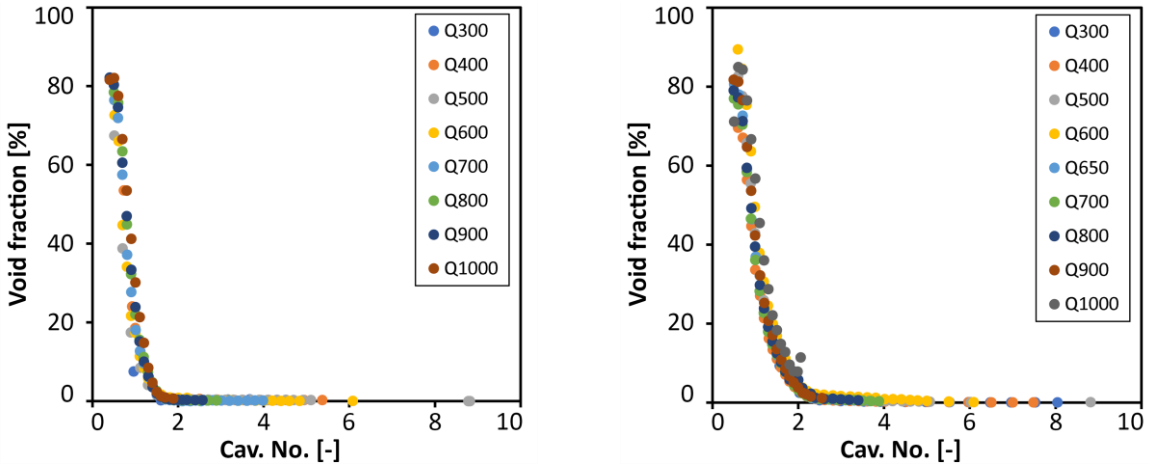

Figure 3.13. Development of void fraction in the draft-tube with cavitation number for a. SW00, b. SW01, c. SW02, and d. SW03

To compare the evolution of void fraction with cavitation number, the values presented in Figure 3.13.a, b, c, and d for different swirlers are plotted altogether in Figure 3.14.a. It is seen in Figure 3.14.a that the void fraction for a certain cavitation number features higher values for higher swirl intensities. Two flow regimes are roughly identified in Figure 3.14.a where regime I corresponds to the operating conditions featuring no/intermittent cavitation ($\beta \approx 0$), and regime II corresponds to full-cavitating conditions ($\beta >> 0$). A methodology will be used in the next sub-section (3.3.3) to establish a limit between regimes I and II. The cavity void fraction in regime II grows exponentially with decreasing cavitation number. Exponential regression for each swirler is plotted in Figure 3.14.b.

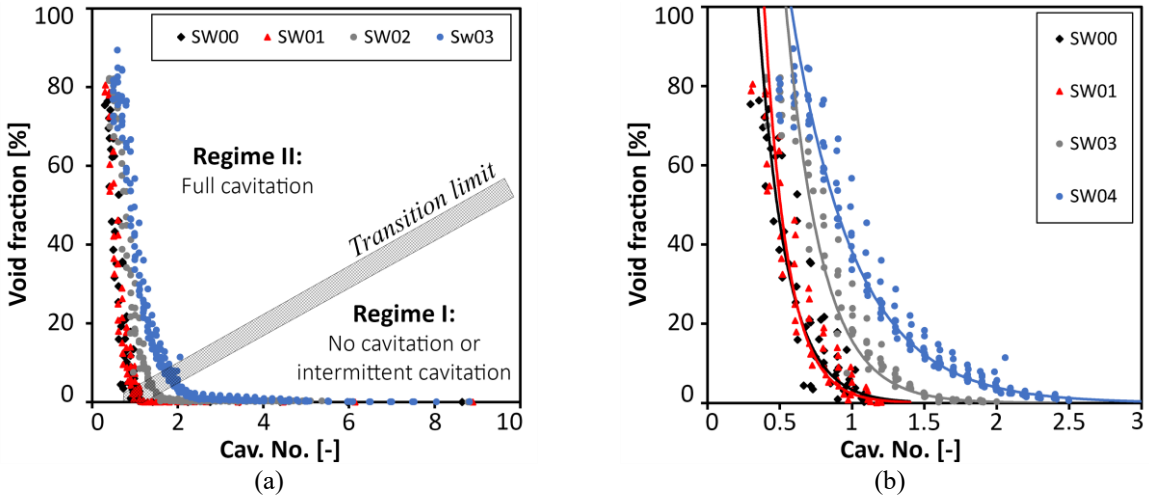

Figure 3.14. Correlation of void fraction in the draft-tube with cavitation number for a. whole range from no-cavitation to full cavitation, and b. from cavitation onset to full cavitation

The exponential correlations for conditions featuring $\beta > 0$ are presented in Table 3.3.

Table 3.3. Correlation between void fraction and cavitation number for different swirlers

Swirler	Exponential correlation	R^2
SW00	$\beta = 620.33e^{-5.223\sigma}$	0.74
SW01	$\beta = 1129.9e^{-6.173\sigma}$	0.77
SW02	$\beta = 897.67e^{-4.044\sigma}$	0.65
SW03	$\beta = 373.57e^{-2.28\sigma}$	0.96

3.3.3. Frequency response of the hydraulic circuit

To understand the cavitation surge characteristics of the system, pressure fluctuations in the Venturi cone are investigated. FFT of pressure fluctuations is computed for sensor B1 (shown in Figure 2.3) using 100-*sec* long signals. In addition, Cross Spectrum Density (CSD) analysis between sensors B1 and B2 (with 2π/3 difference in their angular location) is performed. The purpose of CSD analysis is to understand the nature of fluctuations by looking at the phase difference between the recorded data from two sensors. The nature of pressure fluctuations is synchronous if the phase difference between two sensors is zero, and their nature is convective if the phase difference is equal to the angular difference between locations of two sensors. Results of FFT and phase for one operating condition (SW02, Q = 600 *L/min.*, σ = 4.6) is presented in Figure 3.15.a and b. Frequency values are normalized as Strouhal number by using equation 2.5.

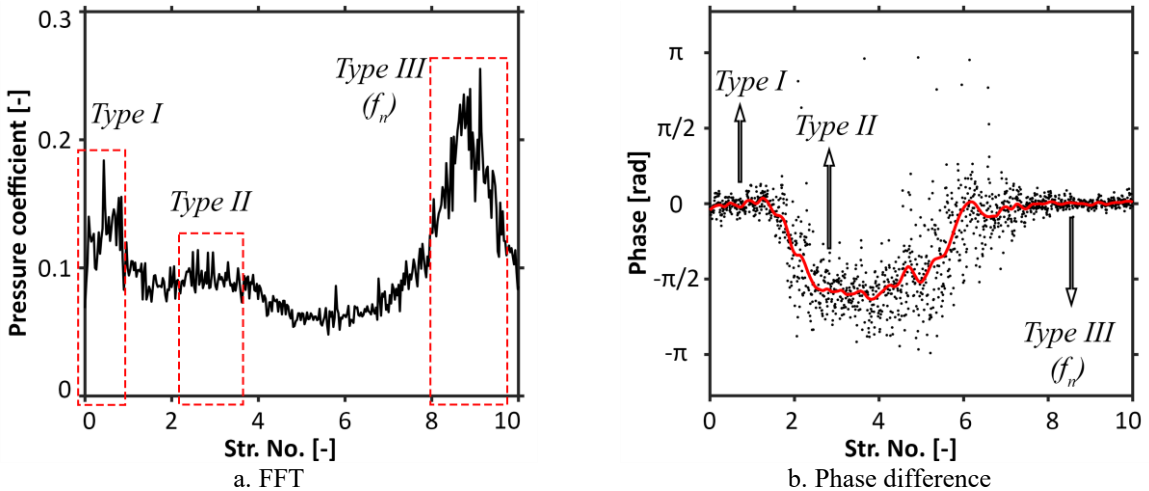

a. FFT b. Phase difference

Figure 3.15. a. FFT of pressure fluctuations and b. phase difference between two sensors at cross section B (SW02, Q = 600 *L/min.*, σ = 4.6)

Similar to the report by Nishi et al. [70], three pressure peaks are identified in Figure 3.15.a called types I, II, and III. Considering the phase values for each peak in Figure 3.15.b, it is revealed that types I and III have synchronous nature (phase ≈ 0). However, type II pressure fluctuations have convective nature (phase ≈ 2π/3). The source and the generation mechanisms of types I and II pressure fluctuations are thoroughly studied in the previous chapter (2). It is seen in the previous chapter that type II pressure fluctuations are induced by local rotation of an axisymmetric vortex in the draft-tube (section 2.2.3). Furthermore, it is revealed that type I pressure pulsations are generated due to an oscillatory instability of vortex breakdown (see section 2.4.1).

FFT and CSD analysis are applied to all the operating conditions. Frequency spectrum of pressure fluctuations are plotted for different cavitation numbers for one operating flowrate in Figure 3.16 (SW02, Q = 600 *L/min.*). It is observed that the frequency of types I and II pressure fluctuations do not change with variation of cavitation number for a certain flowrate. On the other hand, it is noticed that frequency of type III pulsations decreases with decreasing the cavitation number. This reveals that type III pressure peak corresponds to the 1st natural frequency of the hydraulic system. It is reported frequently in the literature that presence of cavitation decreases wave speed in the fluid thus decreases the natural frequencies of the hydraulic system.

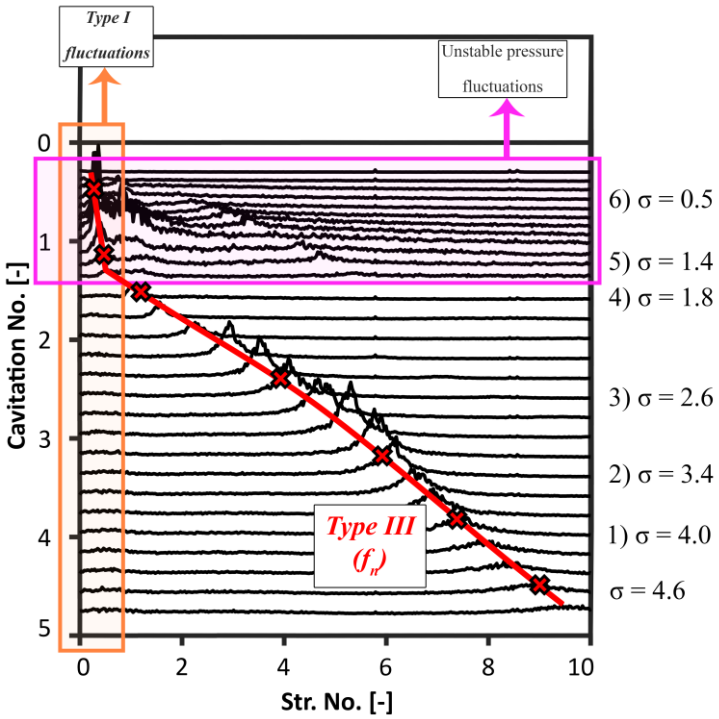

Figure 3.16. Waterfall of pressure fluctuations in cross section B (SW02, Q = 600 *L/min.*)

Type I pressure fluctuations are shown within the orange box in Figure 3.16. Their amplitudes are however very small in comparison with other pressure peaks in the figure. Type III peaks (1st natural frequency of the system) are followed by a red line. By decreasing the

cavitation number in this figure, it is seen that the 1st natural frequency of the system (f_n) decreases and approaches remarkably close to the orange box (type I peaks) around $\sigma \approx 1.8$~1.4. Then for cavitation numbers below this value, the hydraulic system experiences unstable pressure fluctuations with high amplitudes (strong vibrations in the system start from here). This suggests that type I pressure fluctuations act as an excitation trigger to induce resonance and cavitation surge for cavitation numbers lower than the abovementioned values. Therefore, cavitation number $\sigma \approx 1.8$~1.4 (for this certain condition) can be recognized as the onset of cavitation surge in the system (system stability limit). It is also noticed for cavitation numbers within the stable mode ($\sigma > 1.4$) that amplitude of type III pressure fluctuations increases significantly near $\sigma = 3$. This shows that the hydraulic system is excited by one of the harmonics of types I or II pressure fluctuations and experiences resonance. It will be shown later that during this resonance the cavity volume remains very low and cavitation surge does not occur. However, the resonance during the unstable mode (for $\sigma < 1.4$) is accompanied by cavitation surge with significant fluctuations of cavity volume which induces strong vibrations in the hydraulic system.

Six cavitation numbers are selected from Figure 3.16 to investigate the evolution of types I, II, and III pressure peaks with cavitation number. FFT spectrum and phase for these selected cavitation numbers are presented in Figure 3.17. Pressure peaks type I, II and III are clearly identified in Figure 3.17.a, b, and c. It is also noticed that frequency of type III (f_n) moves to lower frequencies by decreasing the cavitation number from Figure 3.17.a to c. In Figure 3.17.d however, frequency of type III (f_n) coincides with frequency of type II. Therefore, pressure peak type II cannot be identified in Figure 3.17.d. By decreasing the cavitation number in Figure 3.17.e, natural frequency of the hydraulic system (f_n) reaches to the frequency of type I pressure pulsations around $\sigma \approx 1.4$; consequently, the vortex becomes unstable and induces unstable pressure pulsations with high amplitudes (cavitation surge) in the system. This unstable pressure pulsations preserves happening by reducing the cavitation number until a very low value. Figure 3.17.f. for $\sigma \approx 0.5$ shows that the natural frequency of the system (f_n) features a significantly low value (lower than frequency of type I pressure pulsations). At this condition, lower frequency of f_n than frequency of type I avoids occurrence of cavitation surge. This statement is also approved during observation of experiments: by reducing the cavitation number, cavitation surge (severe noise and vibrations) appears at a certain cavitation number and it disappears at a lower cavitation number.

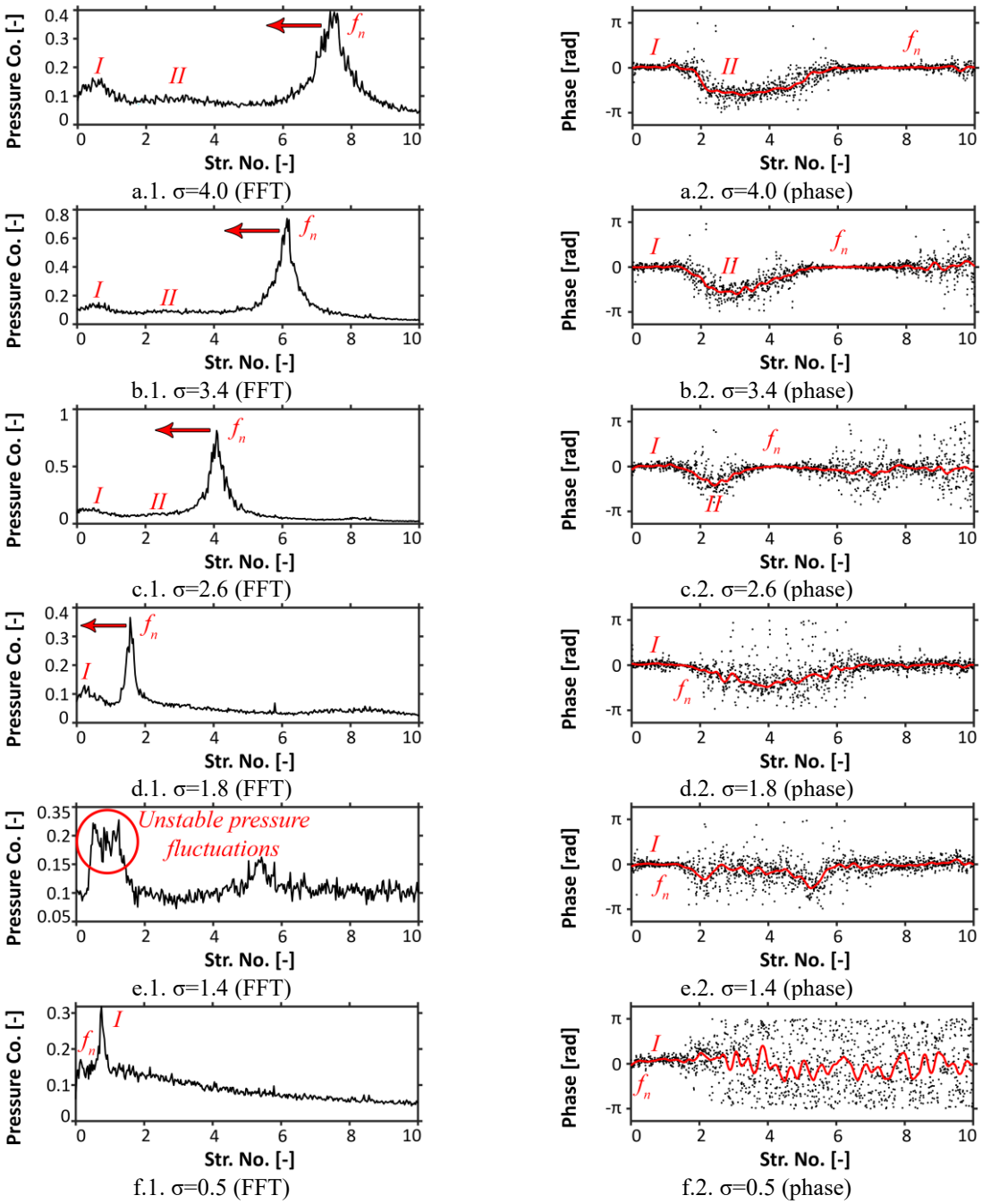

Figure 3.17. a. FFT of pressure fluctuations and b. phase of fluctuations in cross section B for different cavitation numbers: a. σ=4.0, b. σ=3.4, c. σ=2.6, d. σ=1.8, e. σ= 1.4, f. σ=0.5

The natural frequency of the hydraulic system is plotted against cavitation Number for all swirlers in Figure 3.18. Similar to the presented results in Figure 3.13 for evolution of cavity volume by cavitation number, it is noticed in Figure 3.18 that the natural frequency of the system follows the same trend for each swirler. This conveys that flowrate does not have any influence on the natural frequency of the system.

Figure 3.18 shows that the natural frequency of the system for all operating conditions experiences a transition from stable to unstable modes as explained above for Figure 3.16. The transition point is shown in Figure 3.18 for each swirler.

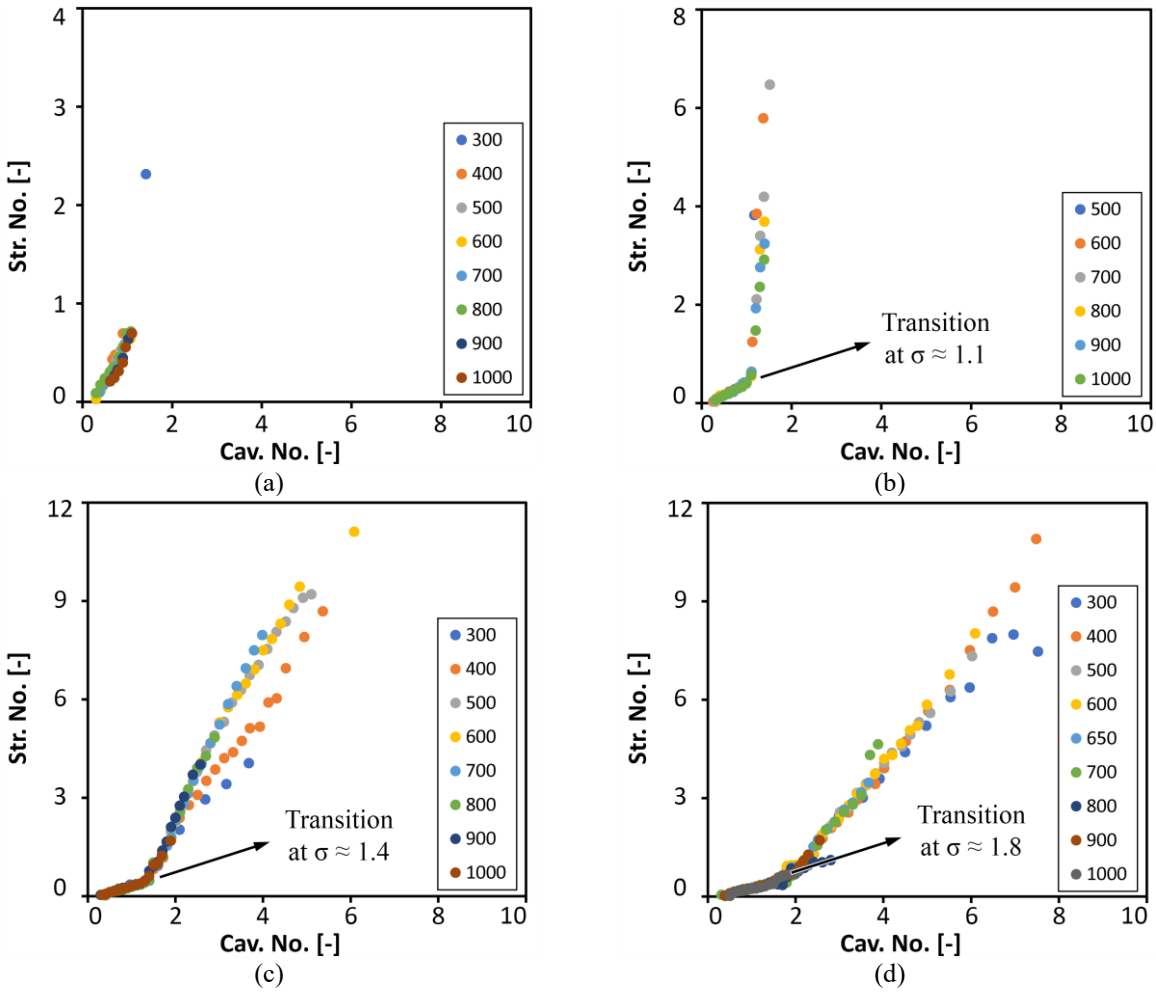

Figure 3.18. Natural frequencies of the hydraulic circuit for a. SW00, b. SW01, c. SW02, and d. SW03

The 1st natural frequencies of the hydraulic system (f_n) are compared for all swirlers in Figure 3.19. Using the transition points which are introduced above, the operating points are divided into two regimes I and II. The pressure fluctuations show a stable behavior in the first regime. However, regime II features system instability with cavitation surge.

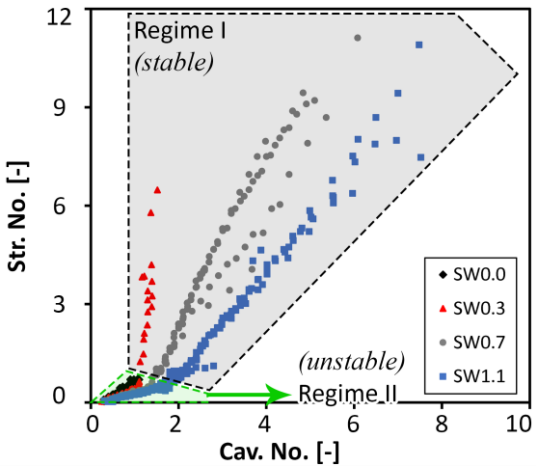

Figure 3.19. Comparison of natural frequencies of the hydraulic circuits for all swirlers

Linear regressions are established between the natural frequency of the system (f_n) and cavitation number for each swirler in Figure 3.20.

The linear correlations for each regime I and II between the natural frequency of the system (f_n) and cavitation number is presented in Table 3.4 and Table 3.5, respectively.

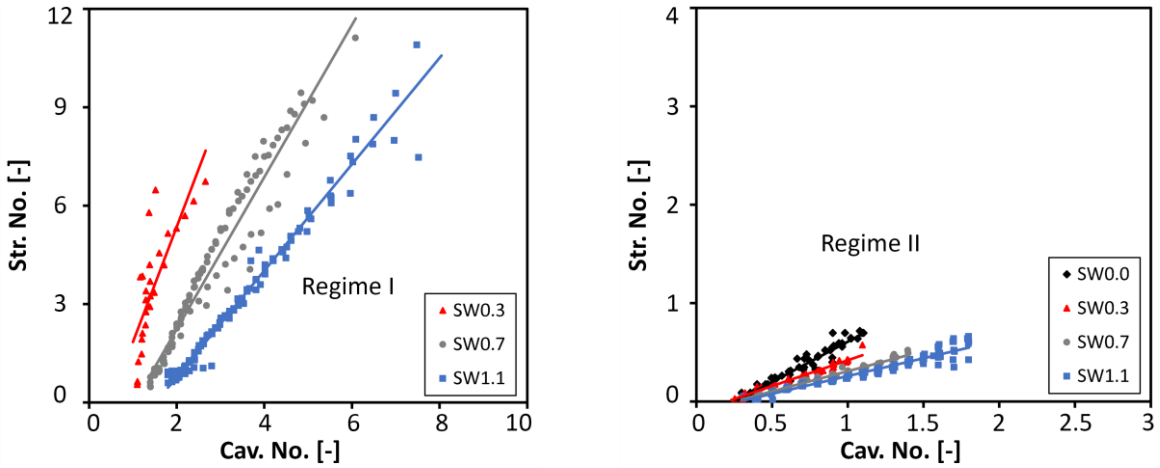

Figure 3.20. Correlation of the natural frequencies of the hydraulic circuits for all swirlers in a. regime I and b. regime II

Table 3.4. Linear correlations of the natural frequencies and cavitation numbers for regime I

Swirler	Linear correlation	slope	R^2
SW00	-	-	-
SW01	$Str. = 3.52\sigma - 1.68$	3.52	0.62
SW02	$Str. = 2.32\sigma - 2.41$	2.32	0.94
SW03	$Str. = 1.62\sigma - 2.47$	1.62	0.98

Table 3.5. Linear correlations of the natural frequencies and cavitation numbers for regime II

Swirler	Linear correlation	slope	R^2
SW00	$Str. = 0.82\sigma - 0.21$	0.82	0.91
SW01	$Str. = 0.52\sigma - 0.10$	0.52	0.96
SW02	$Str. = 0.41\sigma - 0.10$	0.41	0.97
SW03	$Str. = 0.36\sigma - 0.10$	0.36	0.93

It is noticed in Table 3.4 and Table 3.5 for both regimes I and II that increasing the swirl intensity (from SW00 to SW03) decreases the slope of correlations between the natural frequency of the system (f_n) and cavitation number. Slopes of linear correlations in Table 3.4 and Table 3.5 is plotted against the swirl intensity for regimes I and II in Figure 3.21.a. and b, respectively. Figure 3.21 shows that the slope of the correlation between the natural frequency of the system (f_n) and cavitation number can be predicted using exponential correlations shown in this figure. Using the presented correlations in Table 3.4, Table 3.5, and Figure 3.21 enables estimation of the

natural frequency of the system based only on cavitation number and swirl intensity of the swirling flow.

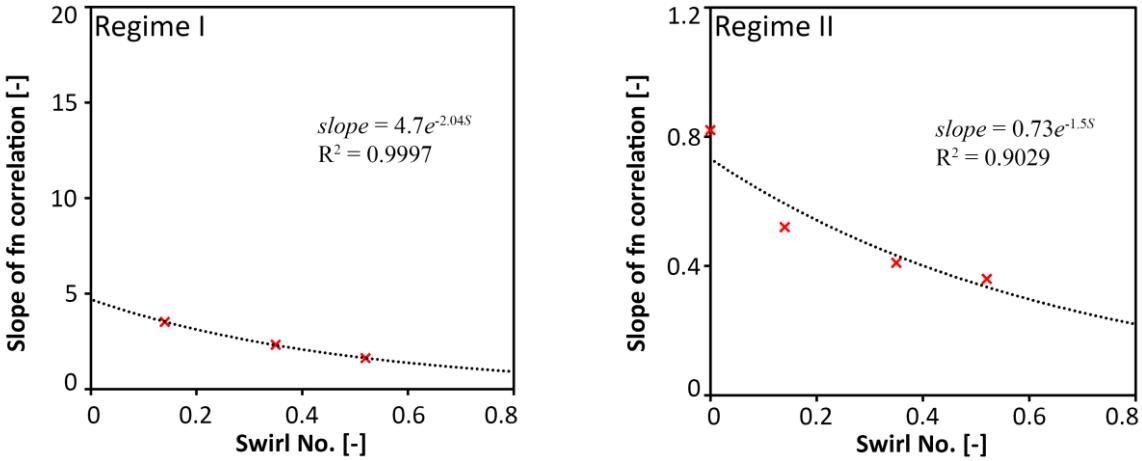

(a) (b)

Figure 3.21. Slope of the correlations for natural frequencies in a. regime I, and b. regime II

3.3.4. Correlation of natural frequency of the hydraulic circuit with void fraction

It has always been advantageous for design engineers to predict the natural frequency of the hydraulic system using practical parameters. It is shown in Table 3.3 that the mean cavity void fraction can be predicted by an exponential correlation for a certain swirl intensity. In the current section, it is tried to find a practical correlation between the natural frequency of the system and void fraction.

Natural frequencies of the hydraulic system (f_n) are plotted against void fraction (β) in Figure 3.22. It is noticed that the natural frequency of the system decreases exponentially with increasing the cavity void fraction in the draft-tube.

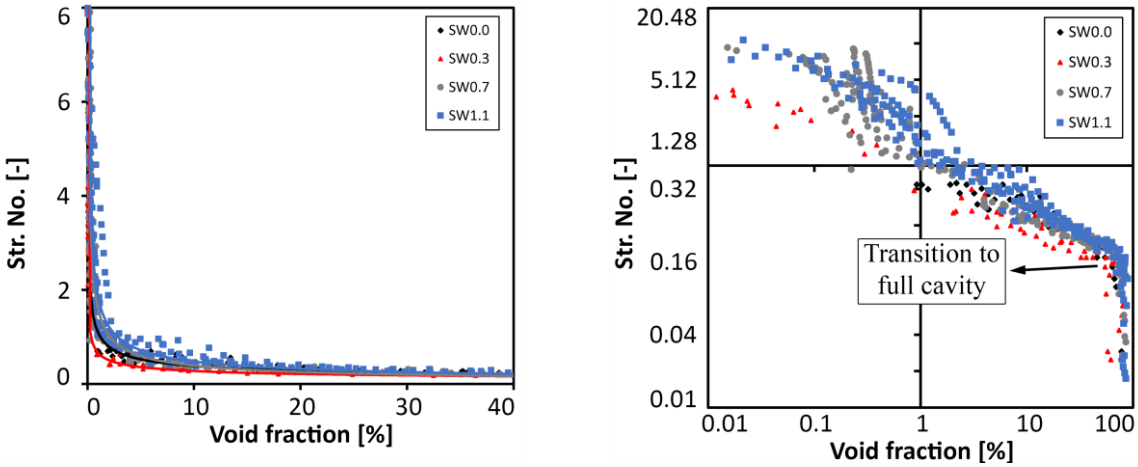

(a) (b)

Figure 3.22. Correlation between natural frequency and void fraction in a. linear and b. logarithmic scales

Four power functions are established for the correlations between the natural frequency and void fraction. The correlations are presented in Table 3.6 for each swirler. The correlations in Table 3.6 would help to predict the natural frequency of the system during its stable and unstable modes.

Table 3.6. Correlation between natural frequency of the hydraulic system and void fraction for different swirl numbers

Swirler	Correlation	R^2
SW00	$Str. = 1.0877\beta^{-0.457}$	0.73
SW01	$Str. = 0.6578\beta^{-0.38}$	0.87
SW02	$Str. = 1.5767\beta^{-0.608}$	0.91
SW03	$Str. = 1.8354\beta^{-0.585}$	0.91

3.3.5. Cavity volume fluctuations

In this section, cavity volume fluctuations are investigated using the cavity visualizations introduced in section 3.2.4. Similar to the previous section, FFT of cavity volume fluctuations are computed over 6 seconds of experiments. The frequency spectrum is plotted for a variation of cavitation numbers in Figure 3.23 (operating condition: SW02, Q = 600 *L/min.*).

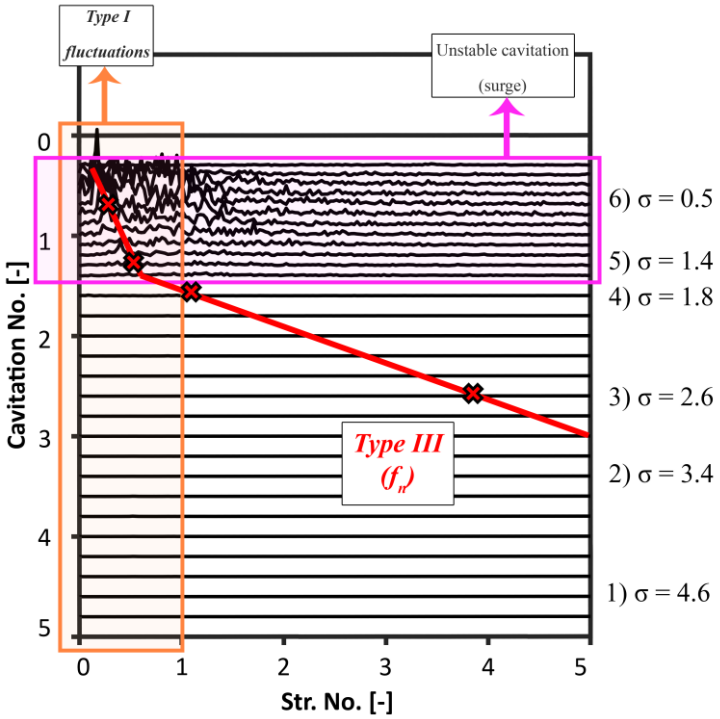

Figure 3.23. FFT of cavity volume fluctuations for cavitation numbers 0.5 to 5 (SW02, Q = 600 *L/min.*)

Unstable cavity fluctuations with high amplitudes are identified in Figure 3.23 for cavitation numbers σ < 1.8~1.4 (purple box) which show occurrence of cavitation surge in the draft-tube. Similar to the results of pressure pulsations which are previously presented in Figure 3.16, type I (orange box) and type III fluctuations (followed by the red line) are identified in Figure 3.23 as well. Frequencies of types I and III cavity volume fluctuations (presented in Figure 3.23) are the same as frequencies of type I and III pressure fluctuations (presented in Figure 3.16). This shows two important matters: 1. Cavitation volume fluctuates only with the frequencies of synchronous pressure pulsations in the system, and 2. Cavitation volume fluctuates at two distinct frequencies, the frequency corresponding to the fluctuations of vortex breakdown location (type I) and the natural frequency of the system (type III or f_n).

The amplitudes of types I and III fluctuations are comparatively smaller than the amplitudes during cavitation surge. Therefore, it is hard to see types I and III in Figure 3.23. To examine the interaction of types I and III fluctuations, the frequency spectrums for six cavitation numbers are selected from Figure 3.23 and presented in Figure 3.24.

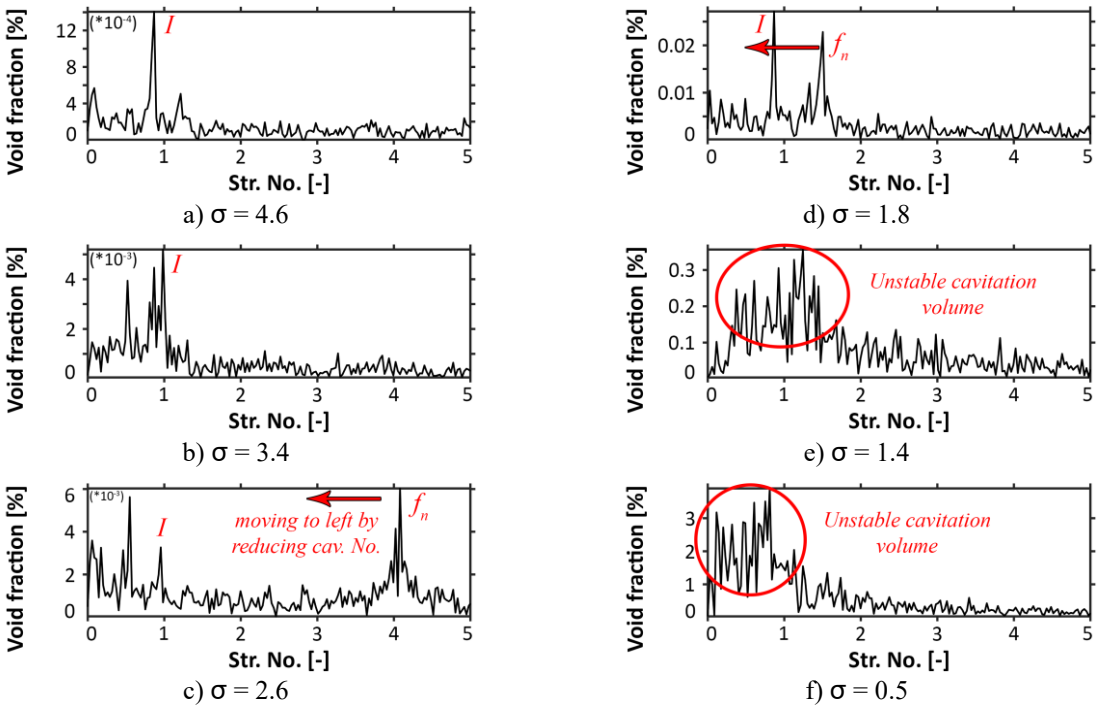

Figure 3.24. FFT of cavity volume fluctuations in the draft-tube for different cavitation numbers: a. σ=4.6, b. σ=3.4, c. σ=2.6, d. σ=1.8, e. σ=1.4, and f. σ=0.5

Figure 3.24.a and b show type I fluctuations with very small amplitudes. Type III fluctuations which moves with decreasing cavitation number is identified in Figure 3.24.c and d Similar to Figure 3.17 from the results of pressure measurements, high-amplitude cavity fluctuations start when frequency of type III coincides with frequency of type I fluctuations. This confirms that type I fluctuations act as an excitation trigger for cavitation surge onset.

In the previous chapter (2), it is proved for no-cavitation condition that type I fluctuations are induced by an oscillatory instability of vortex breakdown location. In Figure 3.25, it is shown for cavitating condition that the vortex breakdown location oscillates with a low frequency as well. This oscillation of vortex breakdown location induces the low frequency pulsations in cavity volume, marked as type I fluctuations in Figure 3.24.

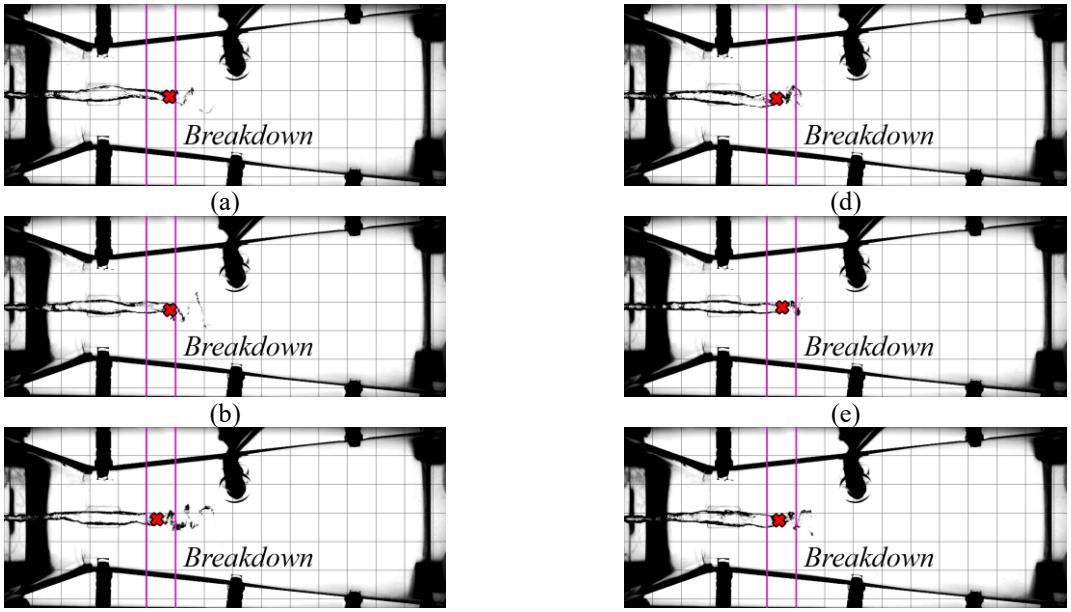

Figure 3.25. Type I fluctuations due to breakdown location oscillations at timesteps a. *t*, b. *t*+0.01 *sec*, c. *t*+0.02 *sec*, d. *t*+0.03 *sec*, e. *t*+0.04 *sec*, and f. *t*+0.05 *sec*

To study the evolution of type III cavity fluctuations with cavitation number, their frequencies and amplitudes are presented in Figure 3.26 for four swirlers. The same behavior as for the natural frequency of the hydraulic system (f_n) presented in Figure 3.18 is observed for evolution of type III fluctuations of cavity volume in Figure 3.26. The same transitions are identified for each swirler. It is noticed that the amplitude of cavity fluctuations type III increases rapidly for cavitation numbers lower than the transition point. This confirms that, for cavitation numbers below the transition point, system features an unstable mode due to cavitation surge.

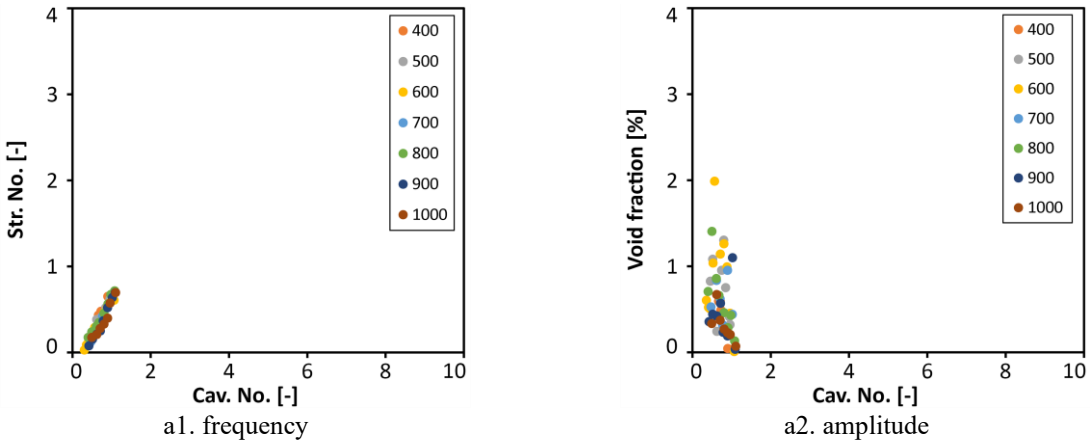

a1. frequency a2. amplitude

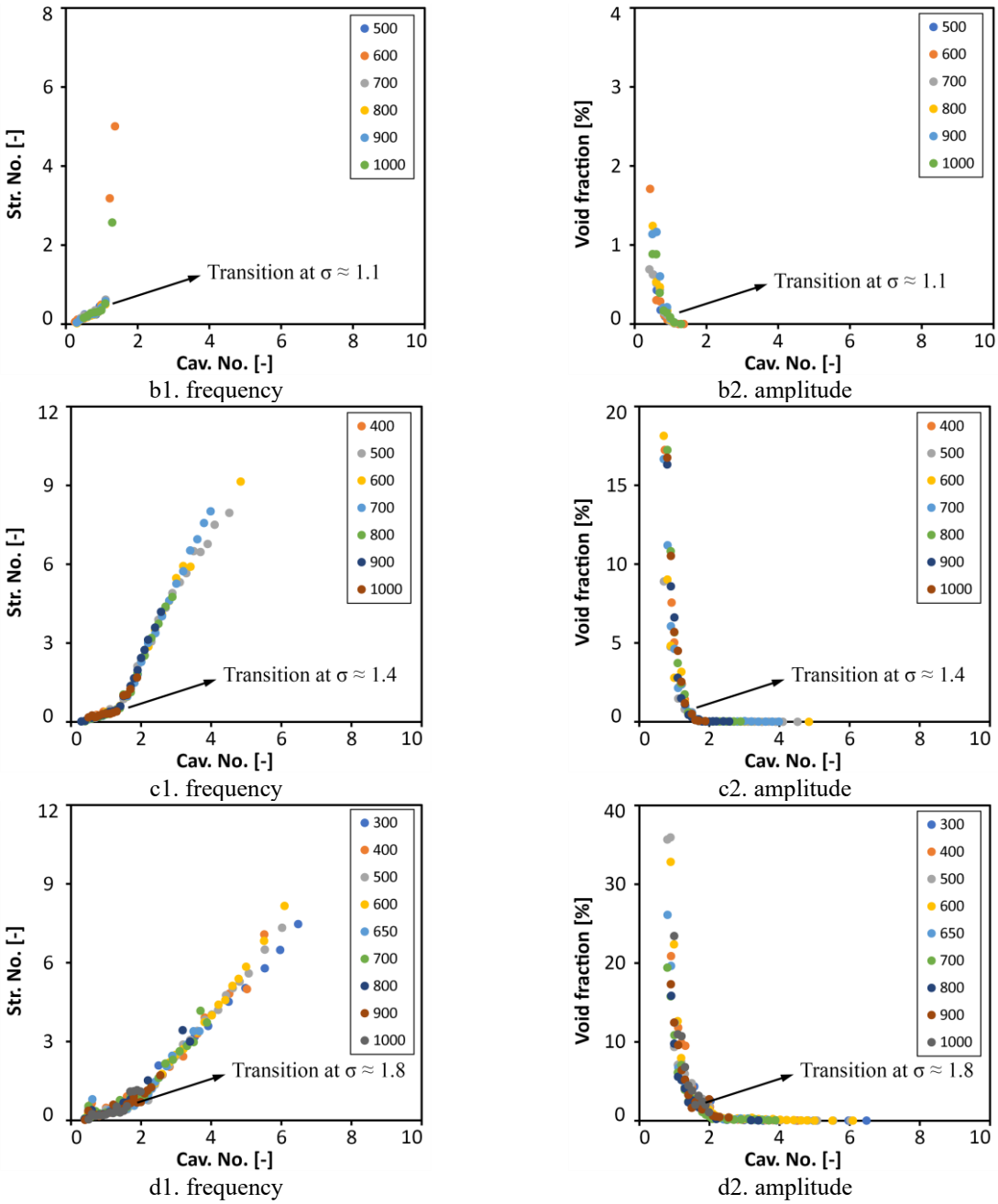

Figure 3.26. Frequency and amplitude of type III cavity volume fluctuations for a. SW00, b. SW01, c. SW02, and d. SW03

Frequency spectrum and amplitudes of type III cavity volume fluctuations are plotted for all swirlers in Figure 3.27. The transition points are used to divide the operating conditions into two regimes I and II, similar to the natural frequencies of the hydraulic system (f_n) in Figure 3.19. During regime I, the cavity shows a stable behavior while it becomes unstable with high-amplitude cavity fluctuations in regime II.

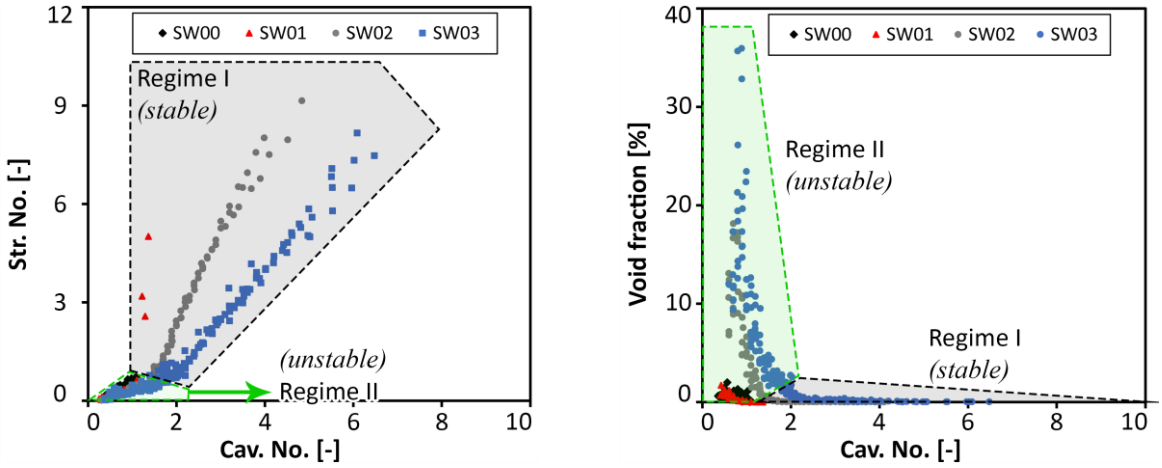

(a) (b)

Figure 3.27. FFT of type III cavity volume fluctuations for all swirlers (a. frequency, and b. amplitude)

Linear correlations between frequency of type III cavity fluctuations and cavitation number are established for regimes I and II in Figure 3.28.a and b, respectively. The correlations are presented in Table 3.7 and Table 3.8.

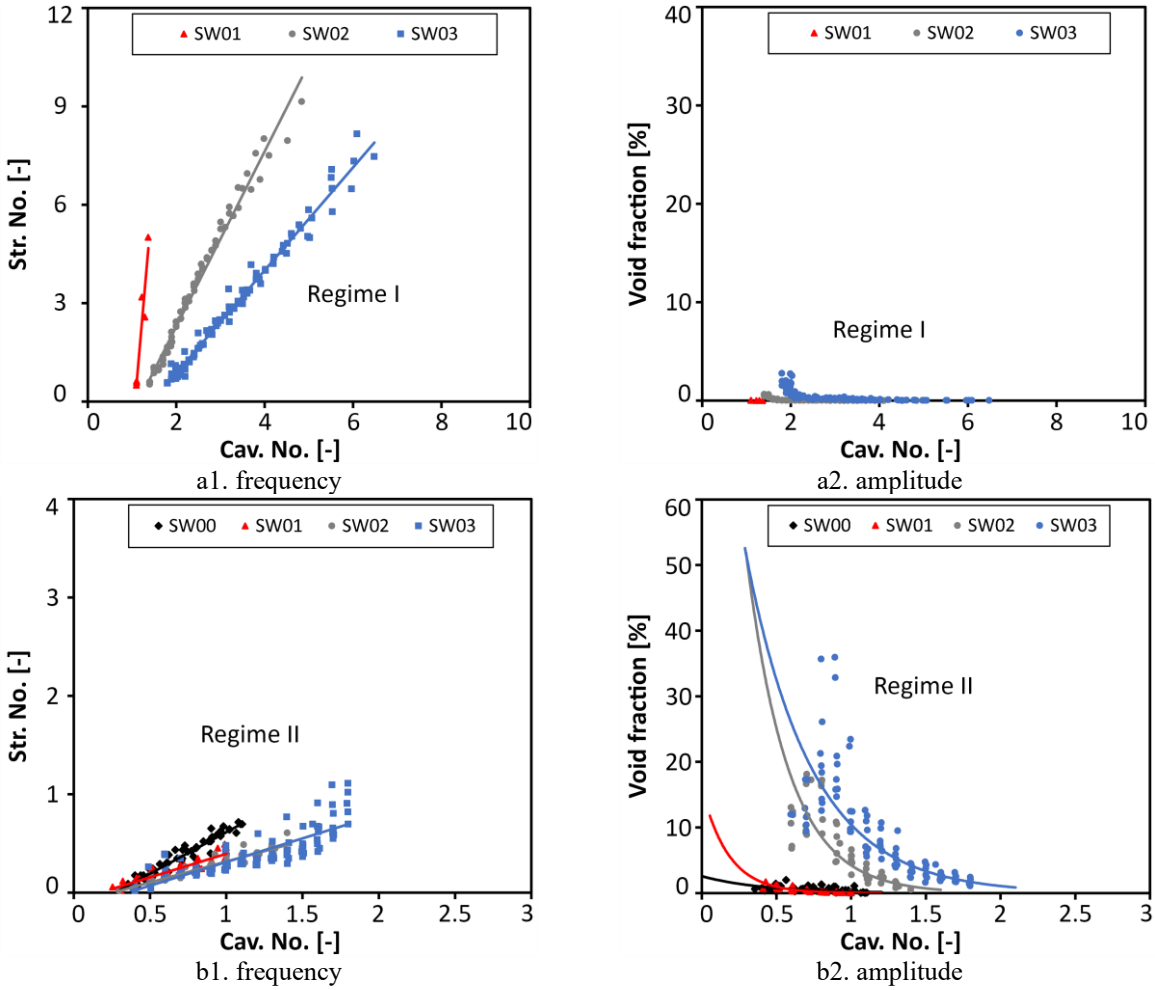

a1. frequency a2. amplitude

b1. frequency b2. amplitude

Figure 3.28. Correlation between FFT of cavity volume fluctuation and cavitation number for a. regime I, and b. regime II

Table 3.7. Linear correlations for frequency of cavity fluctuations and cavitation numbers for regime I

Swirler	Linear correlation	slope	R^2
SW00	-	-	-
SW01	$Str. = 15.48\sigma - 16.50$	15.48	0.91
SW02	$Str. = 2.68\sigma - 3.07$	2.68	0.98
SW03	$Str. = 1.57\sigma - 2.28$	1.57	0.98

Table 3.8. Linear correlations for frequency of cavity fluctuations and cavitation numbers for regime II

Swirler	Linear correlation	slope	R^2
SW00	$Str. = 0.84\sigma - 0.23$	0.84	0.92
SW01	$Str. = 0.47\sigma - 0.08$	0.47	0.88
SW02	$Str. = 0.42\sigma - 0.11$	0.42	0.89
SW03	$Str. = 0.48\sigma - 0.17$	0.48	0.69

Slopes of the linear correlation presented in Table 3.7 and Table 3.8 are plotted against swirl intensities for regimes I and II in Figure 3.29. The correlations presented in Table 3.7 and Table 3.8 along with Figure 3.29 may be used by a design engineer to estimate the frequency of type III cavity fluctuations based on cavitation number and swirl intensity at the inlet of a draft-tube.

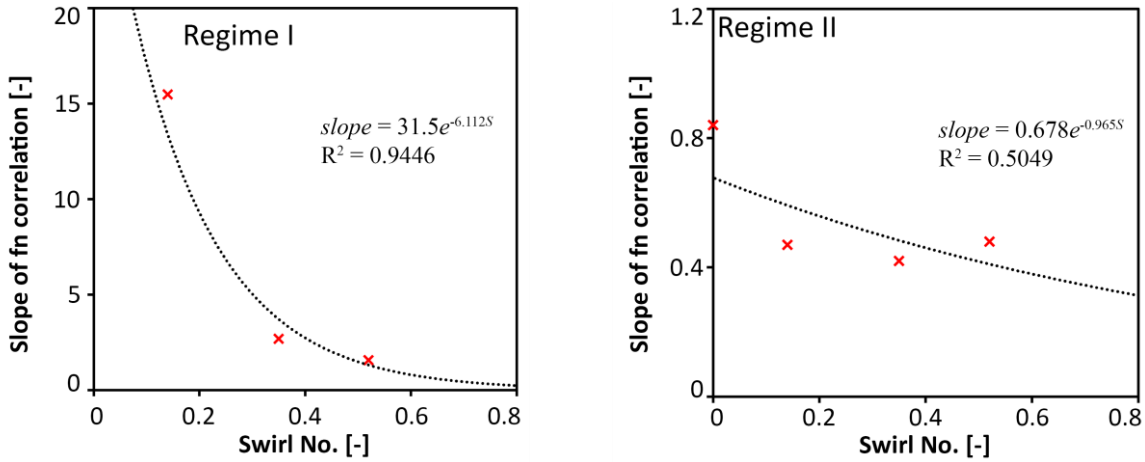

(a) (b)

Figure 3.29. Slope of the correlations for frequency of cavity fluctuations in a. regime I, and b. regime II

3.3.6. Comparison between the natural frequency of the hydraulic circuit and frequency of cavity volume fluctuations

This section is devoted to compare the natural frequencies of the hydraulic system (f_n) obtained from study of pressure fluctuations in section 3.3.3 with the frequencies of type III cavity fluctuations. To do so, the linear correlations presented in Table 3.4, to Table 3.8 are used to

compare the frequencies in regimes I and II in Figure 3.30.a and b. Figure 3.30.a shows that during regime I (stable mode) type III fluctuations of cavity volume matches with the natural frequencies of the hydraulic system for SW02 and SW03. For SW01 however a large deviation between two correlations is observed. During regime II (unstable mode) in Figure 3.30.b, a fair agreement between type III fluctuations and the natural frequencies of the system is achieved.

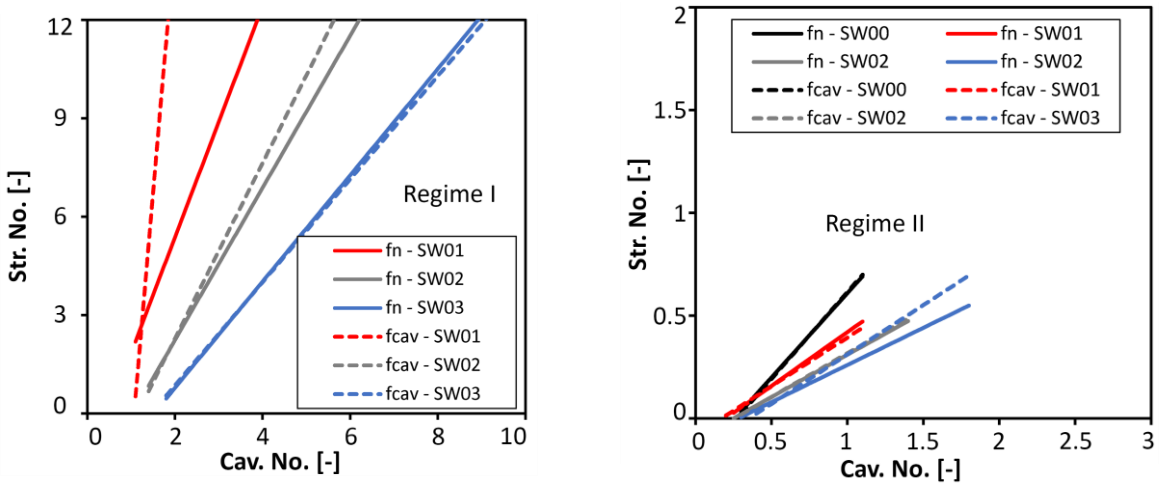

(a) (b)

Figure 3.30. Comparison of the natural frequency of the hydraulic system and the frequency of the cavitation volume fluctuations for different swirl intensities in a. regime I, and b. regime II

Slopes of correlations shown in Figure 3.30 are compared with each other in Figure 3.31. Acceptable agreements between the slopes of correlations in Figure 3.31 are observed. This confirms that the cavity visualization method explained in section 3.2.4 is accurate enough. In addition, the axisymmetric assumption for vortex shape in section 3.2.4 is also correct and practical.

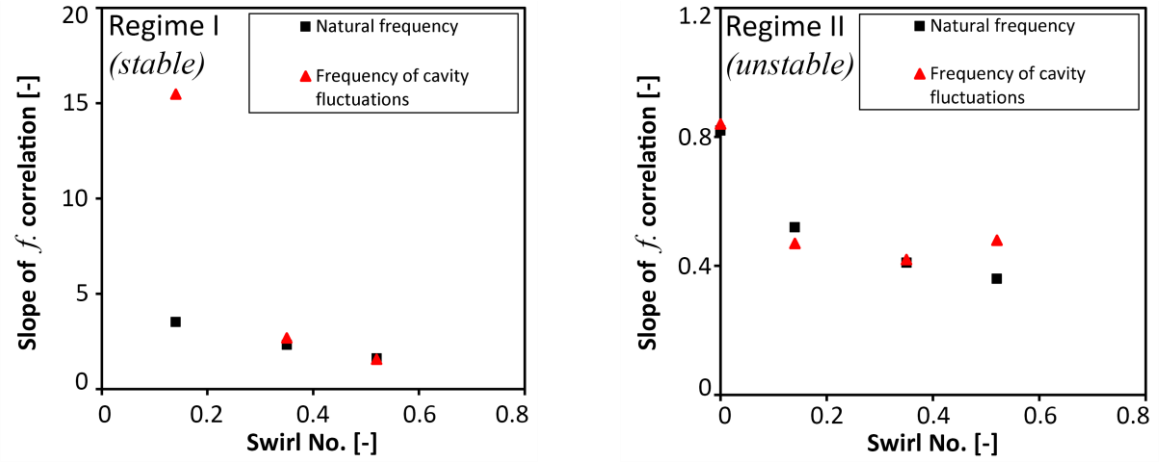

(a) (b)

Figure 3.31. Slopes of the correlations for the natural frequency of the hydraulic system and type III frequency of the cavitation volume fluctuations for different swirl intensities in a. regime I, and b. regime II

3.4. 1D prediction of the hydroacoustic characteristics of the draft-tube

3.4.1. 1D estimation of cavitation compliance

Brennen et al. [56] introduced a transfer matrix back in 1976, as in equation 3.4, to relate the fluctuations of the inlet parameters of an inducer to the fluctuations of the outlet parameters:

$$\begin{Bmatrix} p_2 - p_1 \\ m_2 - m_1 \end{Bmatrix} = \begin{bmatrix} Z_{11} & Z_{12} \\ Z_{21} & Z_{22} \end{bmatrix} \begin{Bmatrix} p_1 \\ m_1 \end{Bmatrix} \quad \textbf{3.4}$$

where p_1 and m_1 are the inlet fluctuating pressure and mass flowrate, p_2 and m_2 are the corresponding values at outlet. Two first constants in the transfer matrix (Z_{11} and Z_{12}) represent the hydraulic characteristics of a hydro-machine (pump, turbine, etc.). The other two constants (Z_{21} and Z_{22}) would be zero if fluid compressibility and structural compliance is negligible. In presence of cavitation, however, these two parameters (Z_{21} and Z_{22}) become important and represent the characteristics of a cavity. Brennen et al. [56, 104] showed that Z_{21} and Z_{22} can be characterized as "cavitation compliance" and "mass flow gain factor", respectively. Cavitation compliance (C_c) and mass flow gain factor (χ) are defined in equations 3.5 and 3.6:

$$C_c = -\frac{\partial V_c}{\partial h} \quad \textbf{3.5}$$

$$\chi = -\frac{\partial V_c}{\partial Q} \quad \textbf{3.6}$$

where V_c, h, and Q are cavity volume (m^3), head (m) and flowrate (m^3/s).

The main objective of the current section is to predict the natural frequency of the draft-tube using the 1D hydroacoustic characteristics of the draft-tube. It is shown that the natural frequency of a draft-tube during cavitation condition mainly depends on cavitation compliance (C_c), while mass flow gain factor (χ) does not have a significant influence on it [20, 105]. Plenty of precious research have been published in literature proposing different methods for calculation of cavitation compliance [55, 59, 106-112]. In the current thesis however, a direct method based on cavitation visualization is employed to compute cavitation compliance. The methodology explained in section 3.2.4 is used to compute the mean cavity volume for all operating conditions. Then, cavitation compliance is directly calculated using equation 3.5 and plotted in Figure 3.32 for four swirlers. Therefore, the computed compliance is the concentrated cavitation compliance in the diffuser part of the Venturi.

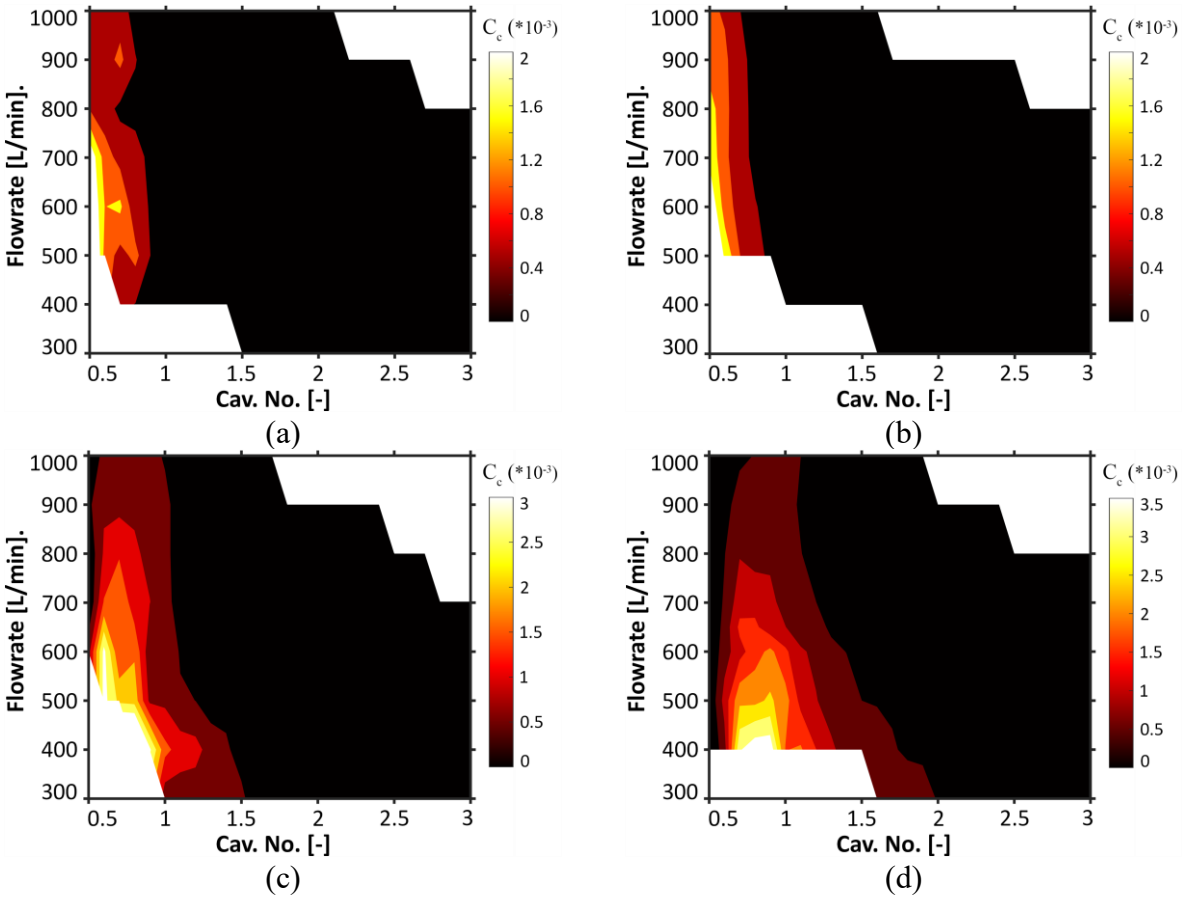

Figure 3.32. Cavitation compliance for a. SW00, b. SW01, c. SW02, and d. SW03

It is noticed in Figure 3.32 that the cavitation compliance for each swirler starts increasing by appearance of cavitation at a certain cavitation number. Moreover, for each swirler, the maximum value of cavitation compliance is identified at a certain cavitation number for all flowrates. This conveys that the operating flowrate does not have any influence on the location of the maximum cavitation compliance. The presented results of cavitation compliance will be used in the following sections (3.4.2 and 3.4.3) to compute wave speed and the first natural frequency of the draft-tube.

3.4.2. Approximation of wave speed in the draft-tube

Nicolet [113], Alligne [114], and Landry [115] developed a 1-dimensional methodology based on an equivalent RLC electrical scheme for predicting the hydroacoustic characteristics of a hydraulic system. They showed that the local wave speed (a) in a differential element of the draft-tube (dz) with cavitating flow can be estimated using equation 3.7:

$$a_{equ.} = \sqrt{\frac{g.A(z).dz}{C_{equ.}}} \quad \textbf{3.7}$$

where $A(z)$ is the corresponding cross-section area at location z, and the equivalent cavitation compliance ($C_{equ.}$) is:

$$C_{equ.} = C_c + C_{water} + C_{pipe} \quad \textbf{3.8}$$

Gomez showed in his paper [116] that cavitation compliance, in presence of cavitation, features much higher values than water and pipe compliances ($C_c >> C_{water} + C_{pipe}$). Therefore, by neglecting C_{water} and C_{pipe} in equation 3.8, equation 3.7 for the local wave speed can be re-written as in equation 3.9.

$$a = \sqrt{\frac{g.A(z).dz}{C_c}} \quad \textbf{3.9}$$

For simplicity in calculation of wave speed, the whole draft-tube is assumed as one long element. Therefore, dz and $A(z)$ in equation 3.9 can be replaced with L and A_{throat} (equation 3.10):

$$a = \sqrt{\frac{g.A_{throat}.L}{C_c}} \quad \textbf{3.10}$$

where L and A_{throat} are draft-tube length and throat area.

The local wave speed in the draft-tube is calculated for the whole operating condition using equation 3.10. Values of local wave speed are plotted for all swirlers in Figure 3.33.

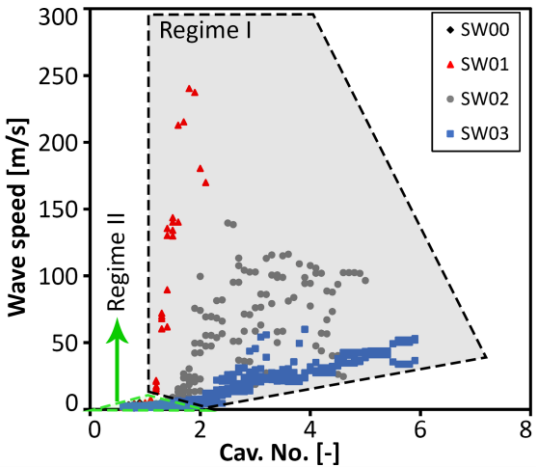

Figure 3.33. Wave speed in the draft-tube for all operating conditions

Similar to the previous sections, a transition between the slope of wave speed versus cavitation number is obvious in Figure 3.33. The operating conditions are then divided into regimes I and II using this transition. Linear regressions between the wave speed and cavitation number are plotted for each regime in Figure 3.34.

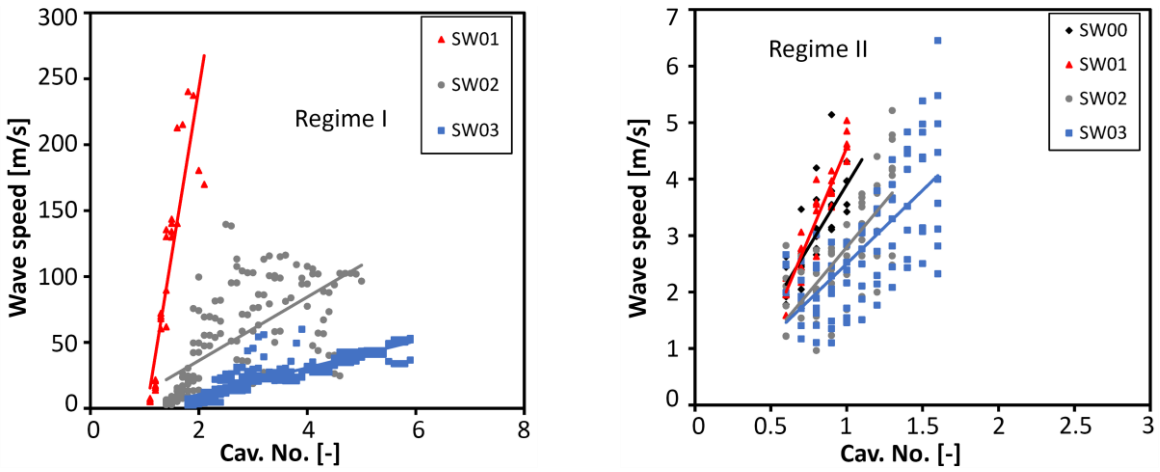

Figure 3.34. Wave speed in the draft-tube for a. regime I, and b. regime II

It is noticed in Figure 3.34 that the local wave speed decreases, however with different slopes, in both regimes I and II by decreasing the cavitation number. It is also interesting that the local wave speed decreases with a higher slope for lower swirl intensities. The linear correlations between the local wave speed and cavitation number are presented in Table 3.9 and Table 3.10 for regimes I and II, respectively.

Table 3.9. Correlation of wave speed in the draft-tube and cavitation number in regime I

Swirler	Linear correlation	slope	R^2
SW01	$a = 252.11\sigma - 261.9$	252.11	0.81
SW02	$a = 24.15\sigma - 12.11$	24.15	0.43
SW03	$a = 10.19\sigma - 9.97$	10.19	0.75

Table 3.10. Correlation of wave speed in the draft-tube and cavitation number in regime II

Swirler	Linear correlation	slope	R^2
SW00	$a = 4.42\sigma - 0.51$	4.42	0.55
SW01	$a = 6.39\sigma - 1.83$	6.38	0.90
SW02	$a = 3.20\sigma - 0.41$	3.20	0.55
SW03	$a = 2.60\sigma - 0.10$	2.60	0.49

3.4.3. Prediction of the natural frequency of the draft-tube

According to Nicolet [113], the cavitating flow in a pipe element (or diffuser) can be represented by an equivalent RLC electrical scheme as shown in Figure 3.35:

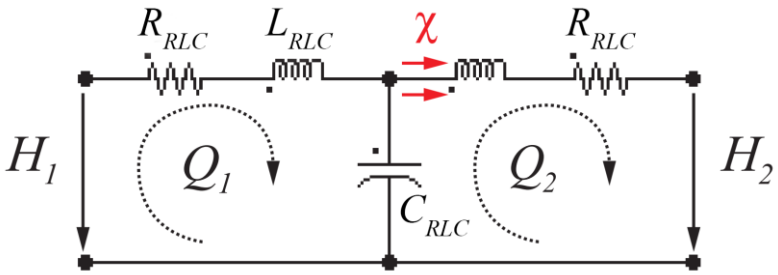

Figure 3.35. RLC electrical scheme for cavitating flow in a pipe element

where R_{RLC}, L_{RLC}, and C_{RLC} represent the resistance, inductance, and capacitance, respectively. If the compressibility of the pipe is neglected, the capacitance C_{RLC} corresponds to the concentrated cavitation compliance (C_c) in the pipe element. L_{RLC} is defined as L/gA where L is the length of the pipe element (here is the diffuser length) [115]. H and Q in Figure 3.35 correspond to the head and flowrate at inlet and outlet of the pipe element. Based on the RLC electrical scheme presented in Figure 3.35, the system of differential equations of the equivalent scheme can be written as:

$$\begin{cases} H_1 = L_{RLC}.\dfrac{dQ_1}{dt} + R_{RLC}.Q_1 + H_c \\ \chi.\dfrac{dQ_2}{dt} + C_{RLC}\dfrac{dH_c}{dt} = Q_1 - Q_2 \\ H_c = L_{RLC}.\dfrac{dQ_2}{dt} + R_{RLC}.Q_2 + H_2 \end{cases} \qquad \textbf{3.11}$$

The determent of the set of equations 3.11 in matrix-form leads to the following characteristic equation 3.12:

$$\begin{pmatrix} \dfrac{R_{RLC}}{L_{RLC}} \\ 1/\tau \end{pmatrix} + \delta \left(\delta^2 + \underbrace{\left[\frac{R_{RLC}}{L_{RLC}} + \frac{\chi}{L_{RLC}.C_{RLC}} \right]}_{2.\mu_s} .\delta + \underbrace{\frac{2}{L_{RLC}.C_{RLC}}}_{\omega_n^2} \right) = 0 \qquad \textbf{3.12}$$

where δ is the eigne value of equations 3.11. τ and μ_s correspond to a free-motion time constant and stability criterion of the system, respectively. By using equation 3.12, the frictionless natural frequency of the system can be derived as in equation 3.13:

$$f_n = \frac{\omega_n}{2\pi} = \frac{1}{2\pi}\sqrt{\frac{2}{L_{RLC}.C_{RLC}}} = \frac{1}{2\pi}\sqrt{\frac{2}{\left(\dfrac{L}{gA}\right).C_c}} \qquad \textbf{3.13}$$

By introducing equation 3.10 into 3.13, the first natural frequency of the pipe element can be written as a function of the local wave speed in 3.14:

$$f_n = \frac{1}{2\pi}\sqrt{\frac{2}{\left(\dfrac{L}{gA}\right).\left(\dfrac{gAL}{a^2}\right)}} = \frac{a}{\sqrt{2}.\pi.L} \qquad \textbf{3.14}$$

The first natural frequency of the draft-tube is computed by using equation 3.14 for all operating conditions [51, 115] and values of the local wave speed presented in Figure 3.33.

The first natural frequencies of the draft-tube under different operating conditions are plotted in Figure 3.36. The predicted values of natural frequency from 1D predictions (Figure 3.36) show very similar trends with the previously presented values in Figure 3.19. Similar to the explanations in section 3.3, a transition line is identified in Figure 3.36, as well.

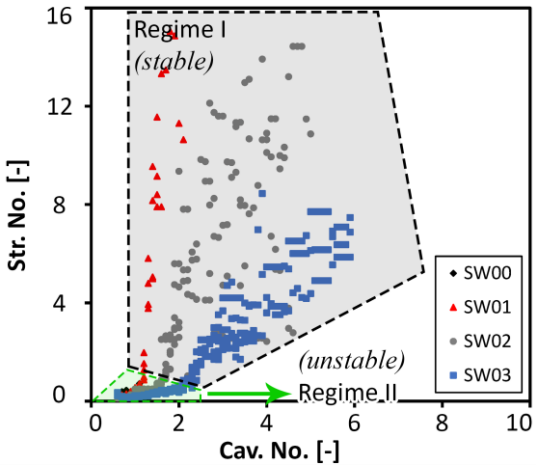

Figure 3.36. Natural frequencies of the draft-tube for all the operating points

The operating conditions presented in Figure 3.36 are divided into two regimes I and II. The regression lines between the natural frequencies of the draft-tube and cavitation numbers are plotted in Figure 3.37. The regression lines presented in Figure 3.37 are very similar to those presented in Figure 3.20 from investigation of pressure fluctuations in the draft-tube.

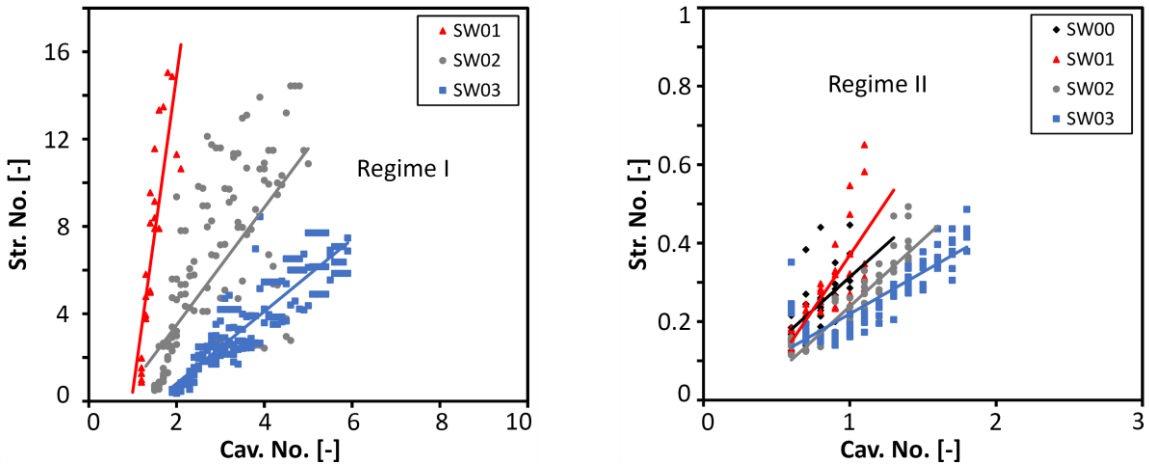

Figure 3.37. Natural frequencies of the draft-tube for a. regime I, and b. regime II

The correlations between natural frequencies of the draft-tube from 1D prediction are presented in Table 3.11 and Table 3.12. These correlations will be used in the next subsection to make a comparison with the natural frequencies obtained in the previous sections of this chapter (3.3.3 and 3.3.5).

Table 3.11. Correlation of natural frequency of the draft-tube from 1D prediction in regime I

Swirler	Linear correlation	slope	R^2
SW01	$Str. = 14.47\sigma - 14.06$	14.47	0.69
SW02	$Str. = 2.69\sigma - 1.90$	2.69	0.45
SW03	$Str. = 1.65\sigma - 2.50$	1.65	0.83

Table 3.12. Correlation of natural frequency of the draft-tube from 1D prediction in regime II

Swirler	Linear correlation	slope	R^2
SW00	$Str. = 0.33\sigma - 0.02$	0.33	0.30
SW01	$Str. = 0.55\sigma - 0.18$	0.55	0.58
SW02	$Str. = 0.34\sigma - 0.10$	0.34	0.81
SW03	$Str. = 0.21\sigma + 0.01$	0.21	0.74

3.4.4. Comparison of the natural frequencies of the draft-tube between 1D prediction and experiments

In the previous sections (3.3.3 and 3.4.3), the 1st natural frequencies of the draft-tube are identified for all operating conditions by using different methods. Linear correlations are established between the 1st natural frequency of the draft-tube and cavitation number within two regimes I and II. The linear correlations obtained from investigation of pressure fluctuations in the draft-tube are presented in Table 3.4 and Table 3.5. Moreover, the linear correlations obtained from 1D predictions are presented in Table 3.11 and Table 3.12. These correlations are compared in Figure 3.38.

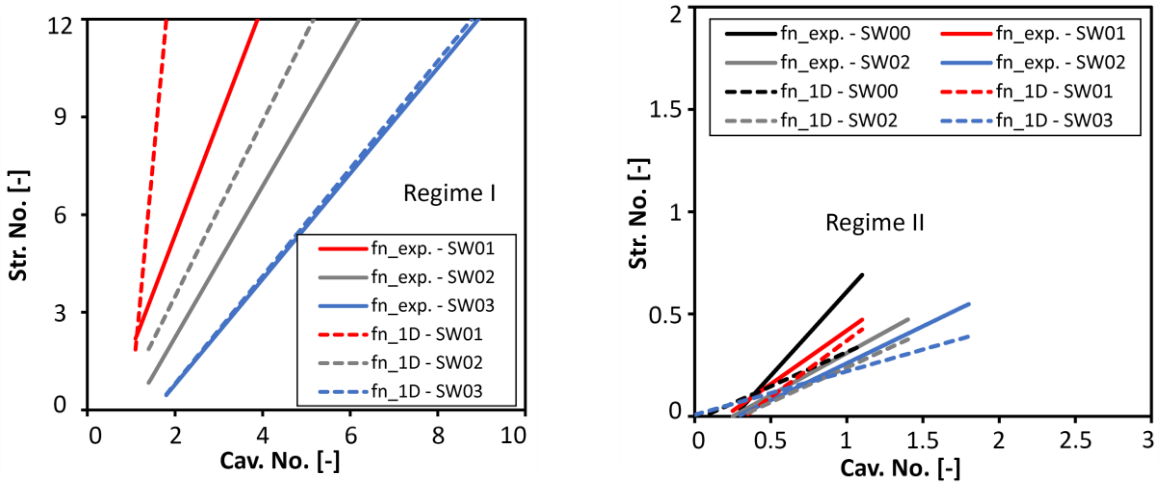

Figure 3.38. Comparison of the 1st natural frequency of the draft-tube obtained from pressure measurements and 1D predictions in a. regime I, and b. regime II

It is seen in Figure 3.38.a. for regime I that the predicted correlations from 1D model shows a perfect match with the obtained values from pressure measurements for SW03 (highest swirl

intensity). However, the deviation between the predicted values from 1D model and pressure measurements increases by reducing the swirl intensity and reaches to a maximum deviation for SW01. In regime II (Figure 3.38.b) however it seems difficult to compare the predicted values.

To obtain a better comparison between the 1D model and pressure measurements, slopes of the correlations presented in Figure 3.38.a and b are shown and compared in Figure 3.39 for regimes I and II.

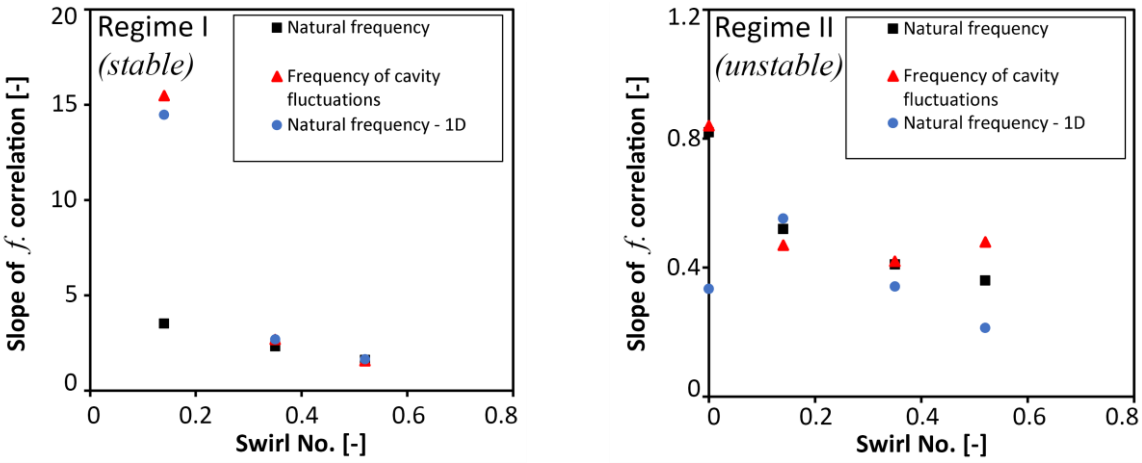

(a) (b)

Figure 3.39. Slopes of the correlations for the natural frequency of the hydraulic system obtained from pressure measurements and 1D prediction and type III frequency of the cavitation volume fluctuations for different swirl intensities in a. regime I, and b. regime

It is noticed in Figure 3.39.a. that the slopes of correlations obtained from 1D predictions and pressure measurements match for SW02 and SW03. However, a comparatively large deviation is observed for SW01. Appearance of this large deviation for SW01 may be due to inaccurate or poor-quality videos of cavity during the experiments. For regime II in Figure 3.39.b. it is seen that the maximum deviation between the slopes of correlations obtained from 1D predictions and pressure measurements occurs for SW00 and SW03. While the slopes show a reasonable match for SW01 and SW02.

The results presented in Figure 3.38 and Figure 3.39 show that the 1D model, with some improvements, can be used to predict the 1st natural frequency of the draft-tube thus its transient behavior during transient operations.

3.5. Summary

This chapter is dedicated to study the cavitation surge characteristics in a simplified draft-tube under different swirling intensities by using experimental methods. A Venturi-tube, installed in a closed-loop, constitute of a converging part, a throat, and a diverging part is employed of

which the diverging part is similar to the draft-tube of a hydro-turbine. The diverging part and the throat concentrate the swirl magnitude in the center of the Venturi to form an axisymmetric vortex in the draft-tube. Four swirl generators (swirler) are used to generate swirling flows with different swirl intensities in the draft-tube, namely, a. zero-swirl, b. low-swirl, c. medium swirl, and d. high-swirl intensities. The swirl configuration (swirl shape and intensity) is similar to the flow field in the draft-tube of a hydro-turbine during its high-load operation.

Experiments are conducted for over 600 operating points for a variety of swirl intensities, flowrates, and cavitation numbers. Cavitation number in the draft-tube is adjusted by using a vacuum pump connected to the downstream tank. LDV measurements are performed in the throat of the Venturi (representing the draft-tube inlet) to compute the swirl number corresponding to each swirler by obtaining the meridional and tangential velocity profiles. Pressure measurements are carried out at 5 sections in the test rig by using 11 wall flush-mounted pressure sensors. A high-speed camera is used to capture the cavity mean volume and its time-transient fluctuations in the Venturi.

Variation of mean cavity volume (in terms of void fraction β) is plotted against cavitation number (σ). It is seen that the cavity volume corresponding to all flowrates follow the same trendline for a certain swirl intensity. Increasing the swirl intensity however increases the cavity volume. A transition point is observed in the β-σ trend for each swirler. It is seen that the void fraction β increases exponentially with decreasing the cavitation number lower than the transition point. Exponential correlations between the void fraction and cavitation number are established for four swirl intensities. These correlations can be further used to predict the void fraction based only on the swirl intensity and cavitation number (independent of flowrate).

FFT and Cross Spectrum Density (CSD) analyses are performed over the pressure fluctuations recorded in the draft-tube. Three pressure peaks are identified in the frequency spectrum of pressure fluctuations, named a. type I: with synchronous nature, b. type II: with convective nature, and c. type III: with synchronous nature. The source and generation mechanisms of type I and II pressure fluctuations, whose frequency remain constant with changing cavitation number, are thoroughly studied in the previous chapter (2). It is observed that type II pressure fluctuations are induced by local rotation of vortical structures in the draft-tube while type I pulsations are generated due to an oscillatory instability of the vortex breakdown. Type III fluctuations, whose frequencies reduce with decreasing the cavitation number, are identified as the 1st natural frequency of the hydraulic system.

The 1st natural frequencies of the hydraulic system are identified for all operating points and plotted against cavitation number. It is seen that, by decreasing the cavitation number, the 1st

natural frequencies of the system (f_n) for each swirler follow a linear trendline until a certain cavitation number, which is the same as the transition point which is also observed on the β-σ plot. It is noticed that the 1st natural frequencies of the system (f_n) follow another linear trendline with a smaller slope for cavitation numbers lower than the transition point. Moreover, it is noticed that the pressure pulsations for the operating points with lower cavitation number than the transition point feature an unstable nature with high-amplitude pressure pulsations. This conveys that the identified transition point in the 1st natural frequency of the system (f_n) is the onset of cavitation surge and resonance in the hydraulic system. By using the identified transition point for each swirler, the operating conditioned are divided into two regimes, a. regime I: stable cavitation, and b. regime II: unstable cavitation surge.

The frequency spectrums of pressure fluctuations for different cavitation numbers at a certain flowrate and swirl intensity are plotted. It is noticed that the abovementioned transition (between the stable and unstable modes of the pressure fluctuations) occurs when the 1st natural frequency of the system (f_n) reaches the frequency-range corresponding to the type I pressure pulsations. This happening proves that the identified transition corresponds to the onset of cavitation surge. Several correlations between the 1st natural frequency of the hydraulic system (f_n) and both cavitation number and void fraction are established. The correlations between the 1st natural frequency of the hydraulic system and void fraction can be used to predict the natural frequency of the system based on volume of cavity and swirl intensity.

Study of the cavity volume fluctuations showed that the cavity volume fluctuates with type I and III (f_n) frequencies. Similar to the previous results from pressure measurements, type III fluctuations of cavity volume experience a transition in their trendline with cavitation number after which the cavity volume becomes unstable featuring high-amplitude pulsations in the draft-tube. This confirms that the system becomes unstable with cavitation surge for cavitation numbers below the transition point.

In the last section of this chapter, cavitation compliance is computed using the results of high-speed visual processing of cavity volume. An 1D electrical scheme and cavitation compliance are used to predict the wave speed in the draft-tube. The 1st natural frequencies of the system (f_n) are then predicted by using the 1D model. Comparison of the obtained natural frequencies from pressure analysis and 1D prediction show agreement for medium and high swirl intensities in regime I. In regime II however the results show acceptable agreement for low and medium swirl intensities.

4. Generation of twin vortex rope in the draft-tube elbow of a Francis turbine during deep part-load operation

4.1. Preface

This chapter focuses on the generation of twin vortex rope in the draft-tube elbow of a Francis turbine at deep part-load operation through analyzing the results of model tests along with numerical simulations. The present research is conducted in the framework of an industrial project to investigate the performance and the draft-tube flow behavior of a medium specific speed Francis turbine under its off-design conditions. The main objective of this research is to study the behavior of precessing vortex core (PVC) and resulting pressure pulsations during deep part-load condition of the turbine. Pressure fluctuations in the draft-tube are measured during model tests over a wide operating range, including 95 operating points with 10 and 11 different values of speed and discharge factors, respectively, to characterize the vortex rope behavior from upper part-load to deep part-load. Frequencies of pressure fluctuations in the draft-tube are determined by performing a Cross Spectrum Density (CSD) analysis over the measured pressure signals during model tests. The frequencies of the resulting pressure pulsations are then correlated to the swirl number of the flow at the runner outlet, whose estimation is based on steady CFD simulations and the analytical expression developed by Favrel et al. [26]. The correlations between the vortex frequency and swirl number feature two transitions used to divide the part-load conditions into three distinct regimes. The behavior of the vortex rope during deep part-load condition is then characterised by performing unsteady CFD analysis at one particular operating point corresponding to 43% of the discharge factor at the BEP. Fast Fourier Transform (FFT) analysis of pressure fluctuations on the complete draft-tube wall and vortex center tracking are then performed to understand the behavior of the vortex in the draft-tube.

4.2. Test case

4.2.1. Description of the test case

The test case is a real size model of a medium specific-speed Francis turbine (Ns. 184 m.kW) designed by the authors in the framework of an industrial project between Waseda University, EAML engineering, and Meidensha companies. The turbine features 15 runner blades, 18 guide vanes, and 9 stay vanes. The draft-tube is an elbow-type draft-tube which includes a cone, a straight pipe, an elbow, and a diffuser. The straight pipe is used due to the structural restrictions of the plant. The hydraulic performance of this turbine has been presented in a previous paper [117]. Table 4.1. General specifications of the turbine at the design point presents the

general specifications of the turbine at its design point, and Figure 4.1. 3D model of the turbine shows the 3D model of the turbine.

Table 4.1. General specifications of the turbine at the design point

Effective head	13.45 [m]	Runner inlet diameter	0.3587 [m]
Discharge	0.36 [m^3/s]	Number of runner vanes	15 [-]
Rotational speed	730 [rpm]	Number of guide vanes	18 [-]
Specific speed (N_s)	184 [m.kW]	Number of stay vanes	9 [-]

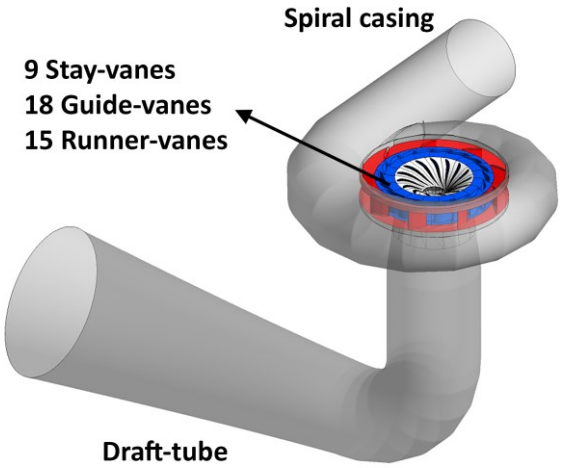

Figure 4.1. 3D model of the turbine

4.2.2. Description of model tests

The model tests are conducted in an open-loop hydraulic test rig located at EAML Engineering Co., Ltd. Figure 4.2 presents the general layout of the test rig. The high head water tanks in Figure 4.2 maintain a constant 15-m head during model tests, while the effective head varies based on flowrate. Flowrate, static head, and torque-speed are respectively measured using an electromagnetic flowmeter (±0.2% accuracy), a digital differential pressure gauge (±0.01% accuracy), and a vortex type electric dynamometer (±0.5% accuracy for torque and ±1 min-1 for speed). The main purpose of the model tests is to determine the performance of the turbine and pressure fluctuations characteristics in no-cavitation conditions from no-load to full-load operating range.

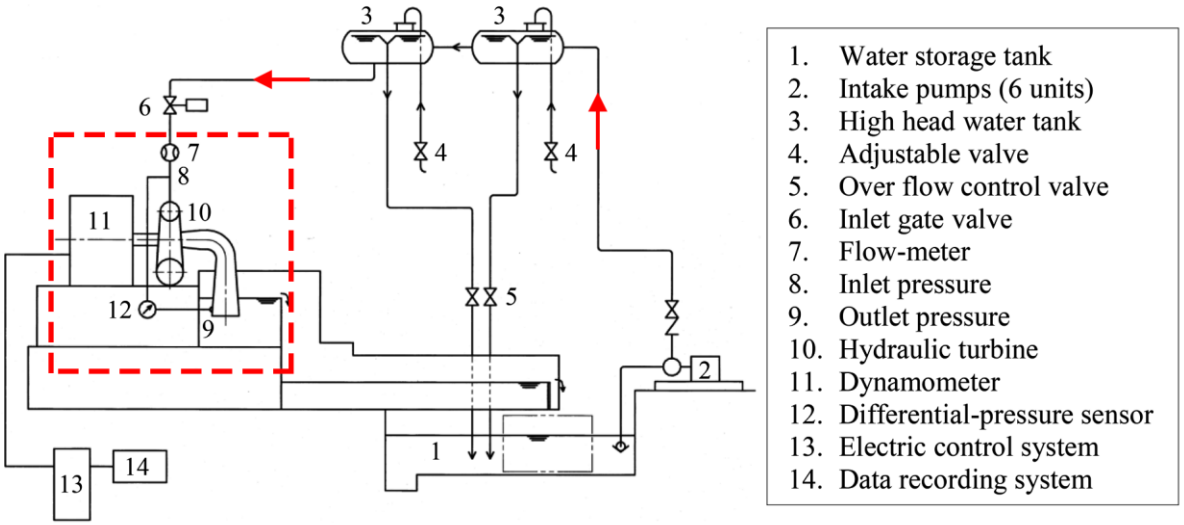

Figure 4.2. General layout of the test rig

Model tests are performed in the range of 10% to 110% guide vane openings for 10 values of n_{ED} and 11 values of Q_{ED} (95 operating points in total), where n_{ED} and Q_{ED} are the speed and discharge factors, respectively, defined as [118]:

$$n_{ED} = \frac{nD}{\sqrt{E}} \qquad Q_{ED} = \frac{Q}{D^2\sqrt{E}}$$

where n, D, Q and E are rotational speed, runner outlet diameter, flowrate, and specific hydraulic energy, respectively. In this chapter, n^*_{ED} and Q^*_{ED} represent the dimensionless speed and discharge factors normalized by the speed and discharge factors at the BEP, respectively:

$$n^*_{ED} = \frac{n_{ED}}{n^{BEP}_{ED}} \qquad Q^*_{ED} = \frac{Q_{ED}}{Q^{BEP}_{ED}}$$

Since the model tests are conducted in an open-loop test rig, the Thoma number cannot be adjusted. The tail water level was however high enough to avoid cavitation onset nearly at all the operating conditions. In addition to the performance tests, pressure measurements are carried out in the draft-tube by using 12 wall flush-mounted static pressure sensors installed in 4 sections of the draft-tube (B, D, E, and G), as shown in Figure 4.3. Two sensors with 180 degrees difference in angular location are installed in each section B and D. In sections E and G, four sensors regularly spaced by 90 degrees are installed. The other sections shown in Figure 3 correspond to monitoring points in CFD simulations which will be described in the following sections.

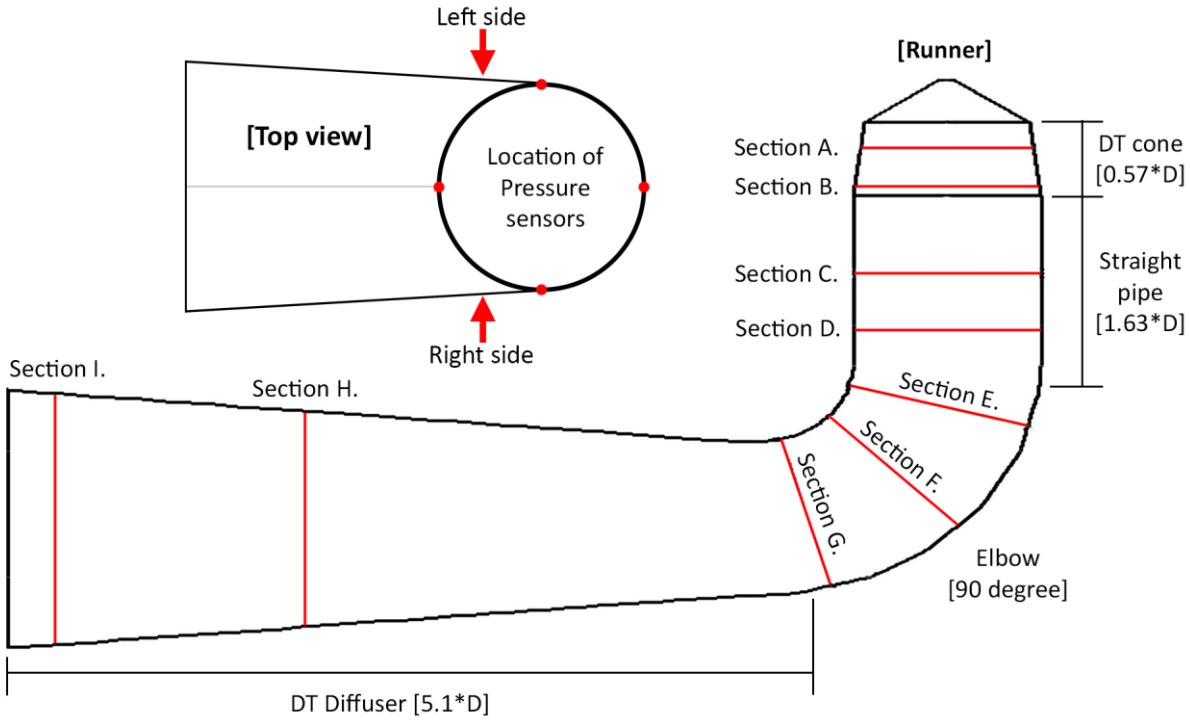

Figure 4.3. Pressure measurement sections in the draft-tube

4.3. Methodology for estimation of iso-swirl lines

4.3.1. Swirl number definition

The precessing vortex core (PVC) observed at part-load conditions results from a vortex breakdown of the swirling flow in the draft-tube. The dynamics of the PVC mainly depend on the swirl intensity of the incoming flow, i.e. the flow leaving the runner in the case of hydraulic turbines [119, 120]. The swirl number S is a common dimensionless parameter to characterize the swirl intensity in the draft-tube of hydraulic machines and in other industrial devices [116, 121, 122]. It corresponds to the ratio between the axial flux of the angular momentum and the axial flux of the axial momentum. A simplified expression omitting the turbulence and pressure terms is given in Equation 4.1 [65].

$$S = \frac{G_\theta}{G_z R} = \frac{\int_0^R V_m . V_t . r^2 . dr}{R . \int_0^R V_m^2 . r . dr} \qquad \textbf{4.1}$$

where V_m and V_t are the meridional and tangential velocity components at the runner outlet, respectively, and R is the radius of the runner outlet. Favrel et al. have obtained an analytical expression of the swirl number as a function of the operating parameters of the machines, i.e. the discharge and speed factors, see Equation 4.2 [26]. By performing Laser Doppler Velocimetry

(LDV) measurements along the diameter of one cross-section in the draft-tube cone, they showed that this analytical expression is in fair agreement with the experimental data. The advantage of using Equation 4.2 is to simply link the speed and discharge factors to the swirl number.

$$\overline{S} = n_{ED} \frac{\pi^2}{8} \cdot \left(\frac{1}{Q_{ED}} - \frac{1}{Q_{ED}^0} \right) \qquad \textbf{4.2}$$

Q_{ED}^0 in Equation 4.2 represents the discharge factor corresponding to the no-swirl condition for a given n_{ED} value.

By using Equation 4.2, the swirl number at the runner outlet of the machine can be estimated on the complete operating range, including head and flow rate variations. However, that requires the value of the discharge factor in no-swirl conditions (Q_{ED}^0) for any value of speed factor. Therefore, steady-state CFD simulations are employed to determine Q_{ED}^0 over the entire range of speed factor, as described in the following section.

4.3.2. Steady-state CFD simulation

Steady-state simulations of the full domain turbine are performed at 87% guide vanes opening which is near the BEP. The results will be further used to estimate the iso-swirl lines of the machine on its complete operating range by applying a method described in the next section. The flow field is computed based on RANS equations using the commercial CFD code ANSYS CFX 19.0 with incompressible and turbulent flow assumptions. The two-equation Shear Stress Transport (SST) k-ω turbulence model is adopted to accurately predict flow separation. The k-ω based turbulence model is commonly used for hydro-machinery simulations [123, 124] since it combines the advantages of both k-ω model (i.e. accurate predictions near walls) and k-ε model (i.e. accurate predictions in the fluid bulk). The inlet and outlet boundary conditions are set to total pressure and average static pressure, respectively, at the inlet of the spiral casing and outlet of the draft-tube. The effective head is determined according to the model tests at the same operating point. Therefore, the flowrate is predicted based on the calculation of the total pressure losses in the turbine. The stationary and rotary domains are connected by using general grid interfaces (GGI). The interfaces between rotating components are set to mixing-plane and frozen rotor for the interfaces between guide vanes and runner, and between runner and draft-tube, respectively. High resolution advection scheme is applied to the governing equations. The convergence criteria

are defined as RMS below 10e-05. Using 22 CPU cores, the simulation takes 5.283e+6 CPU-seconds to achieve the convergence criteria.

4.3.3. Spatial discretization

The whole turbine domain from the spiral casing to the draft-tube outlet is simulated. The stationary parts comprise the Spiral Casing (SC), 9 Stay Vanes (SV), 18 Guide Vanes (GV), and the Draft-Tube (DT), while the rotating part includes 15 Runner Vanes (RV). The mesh is generated separately for each sub-domain. Turbogrid commercial grid generator is used to produce hexahedral elements in the guide vanes and runner vanes while Ansys mesher is employed to generate fine tetrahedral elements in the spiral casing, stay vanes, and the draft-tube. To confirm the independency of the CFD results to the mesh size in terms of efficiency and hydraulic losses, a mesh dependency study was conducted at the BEP for the previous research, and it was shown [117] that the CFD results are in fair agreement with the experiments in terms of efficiency and hydraulic losses. Figure 4.4 shows the comparison of the turbine efficiency at $n_{ED}^{*}=1$ over the entire values of Q_{ED}^{*} between CFD and model test results. It is confirmed that the average difference between CFD and model test results in terms of efficiency is equal to approximately 0.1%.

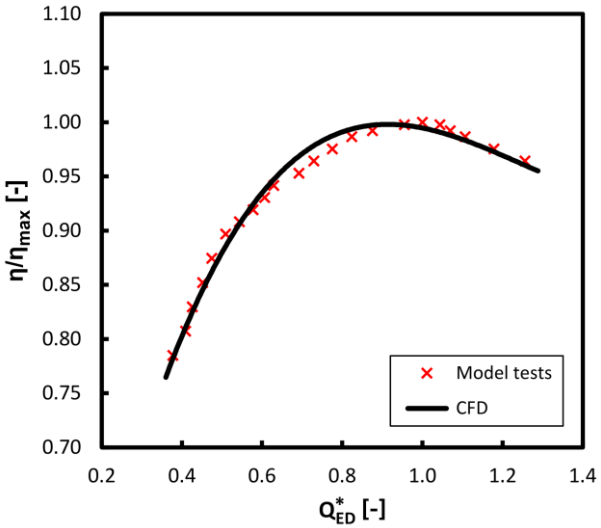

Figure 4.4. Comparison of efficiency between CFD and model test results at $n_{ED}^{*}=1$

4.3.4. Mesh independency

Contrary to the previous research [117] which was focused on the performance of the machine, the present research aims at investigating the behavior of the draft-tube flow during part-load and deep part-load conditions. Therefore, a new mesh dependency study is performed only for the draft-tube mesh, while the mesh for other components remains the same as in the previous research [117]. Table 4.2 presents the grid information for the other components. For the draft tube domain, five grids with different densities are generated and steady-state numerical simulations for the whole components (SC, SV, GV, RV, and DT) are carried out at $n_{ED}^{*}=1$ and 87% guide vanes opening to evaluate the independency of the results to the grid size. The mesh sizes are presented in Table 4.3. For all the draft-tube meshes, the average value of Y+ is kept below 10. The meridional and tangential velocity profiles at the inlet of the draft-tube domain for each mesh are given in Figure 4.5 and Figure 4.6, respectively. The difference between the results of meshes 4 and 5 in terms of velocity is negligible since the average differences between the meridional and tangential velocity profiles obtained with meshes 4 and 5 are equal to 0.25% and 0.61%, respectively. To achieve accurate CFD results, the finest mesh (mesh 5) is chosen for further simulations to mitigate the influence of the mesh on the results.

Table 4.2. Mesh information for the SC, SV, GV, and RV domain

Domain	Mesh type	Nodes	Y+
SC	Tetrahedral	2.69 M	16.7
SV			
GV	Hexahedral	7.63 M	0.2
RV	Hexahedral	8.07 M	3.81

Table 4.3. Mesh information for the draft-tube domain

Mesh	Mesh type	Nodes	Y+
01	Tetrahedral	3.14 M	6.34
02		3.45 M	6.61
03		3.69 M	6.62
04		4.07 M	6.79
05		4.35 M	7.22

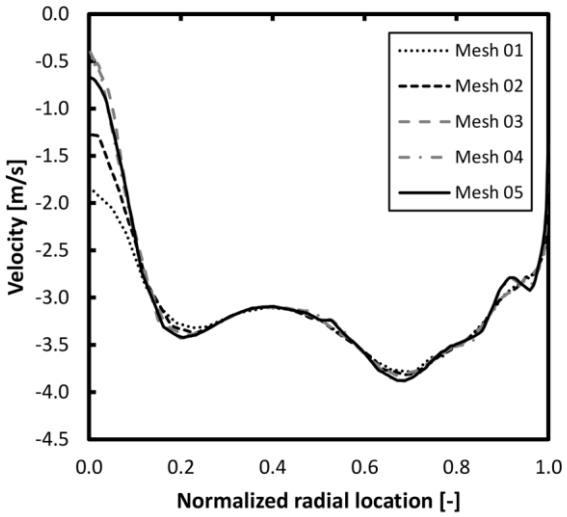

Figure 4.5. Comparison of meridional velocity components at the draft-tube inlet for different meshes

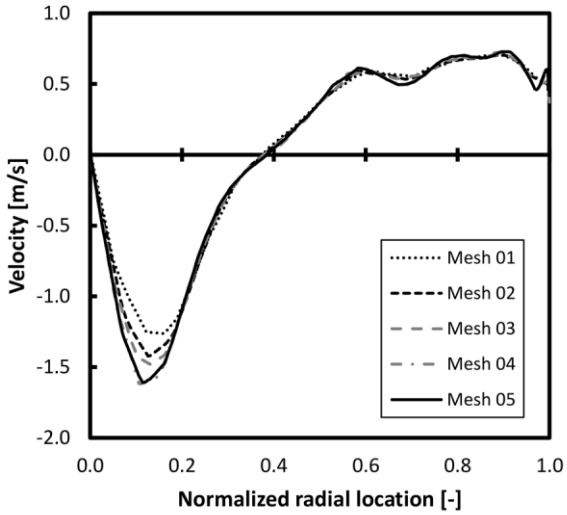

Figure 4.6. Comparison of tangential velocity components at the draft-tube inlet for different meshes

4.3.5. Determination of iso-swirl lines

The no-swirl zone (S=0) is usually identified during model tests by performing visualization of the draft-tube flow in cavitation conditions: it is assumed that the conditions featuring no cavitation in the draft-tube correspond to the no-swirl zone. In the present test-case, model tests are performed in cavitation-free conditions and the no-swirl zone cannot therefore be identified by flow visualization. This section describes a novel method to estimate the no-swirl conditions and iso-swirl lines based on Equation 4.2 and the results of steady-state CFD simulations. The steady-state CFD simulation is first performed at a selected operating point (

$n_{ED}^{*}=1$ and 87% guide vanes opening) near the BEP, where no unsteady phenomenon occurs. The complete method described in the following is summarized in the form of a flowchart in Figure 4.7.

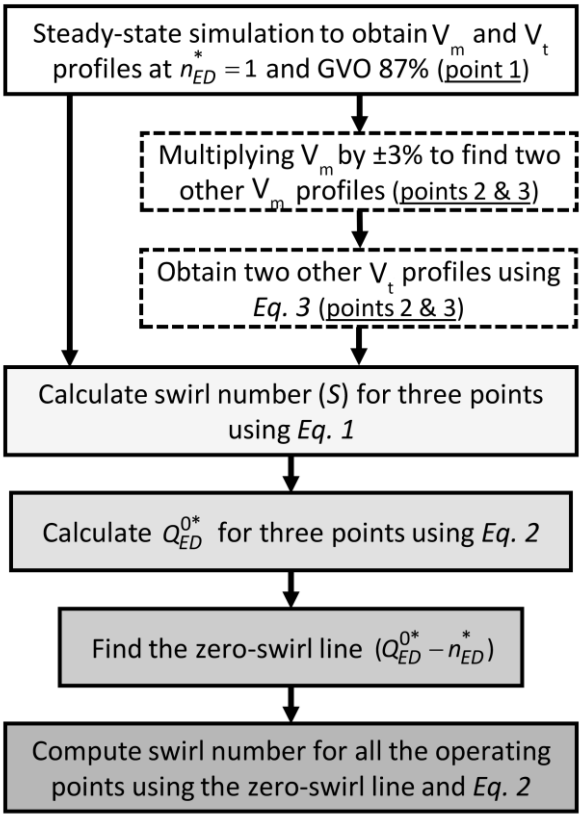

Figure 4.7. Flowchart for determination of the zero-swirl line

To estimate the no-swirl line, it is first necessary to find a set of no-swirl points Q_{ED}^{0*} on the $n_{ED}^{*}-Q_{ED}^{*}$ chart. However, it has been reported in the literature [26] that the relation between Q_{ED}^{0*} and n_{ED}^{*} nearly follows a linear relation over the entire range of n_{ED}^{*}. Therefore, only two no-swirl points may be sufficient to determine the no-swirl line. The method presented in the following however uses three points to improve the quality of the linear regression.

By using Equation 4.1 along with the meridional and tangential velocity profiles at the runner outlet obtained from steady CFD, the swirl number is estimated at S=-0.1324 for the simulated operating point. A negative value for the swirl number indicates that the simulated point is slightly located at high load condition (flowrate higher than the value in no-swirl conditions). By using Equation 4.2, the value of the discharge factor in no-swirl conditions for the simulated speed factor $n_{ED}^{*}=1$ can be estimated at $Q_{ED}^{0*}=0.917$.

To determine two additional no-swirl points, the meridional and tangential velocity profiles (V_m and V_t) at the runner outlet for two additional operating points at other n_{ED}^* values on the $n_{ED}^* - Q_{ED}^*$ chart are necessary. One method would be to simulate two additional operating points by CFD, which is however time-consuming. In the present chapter, a more straightforward method is used. It is assumed that the V_m distribution in the span direction at the runner outlet remains constant along an iso-swirl line for operating points very close to the simulated one. Therefore, the meridional velocity profiles of two additional points with same swirl number as the simulated point are assumed to be equal to ±3% of the meridional velocity profile of the simulated point. In this case, the discharge factors (Q_{ED}^*) for the two additional points are equal to ±3% of the discharge factor from CFD simulation with assuming constant specific hydraulic energy (E) for all three points. Then, the runner speed is modified for the additional points to achieve kinematic similarity with the simulated operating point, i.e. similar velocity triangle and swirl number. Based on the velocity triangles at the runner outlet, the V_t profiles can be computed for the two additional operating points by solving Equations 4.1 and assuming a constant β_2.

$$V_t = U - \frac{V_m}{\tan(\beta_2)} \qquad \textbf{4.3}$$

where U and β_2 are the runner circumferential velocity and blade angle at runner outlet, respectively.

By using the same procedure as the one used to determine the first no-swirl point, two additional no-swirl points (n_{ED}^* and Q_{ED}^{*0}) are determined and given in Table 4.4 and Figure 4.8.

Table 4.4. Zero-swirl points

Point	n_{ED}^*	Q_{ED}^*	S	Q_{ED}^{0*}
[-3% V_m]	0.9658	0.9543	-0.1324	0.889
[CFD V_m]	1.0033	0.9838	-0.1324	0.917
[+3% V_m]	1.0256	1.0133	-0.1324	0.944

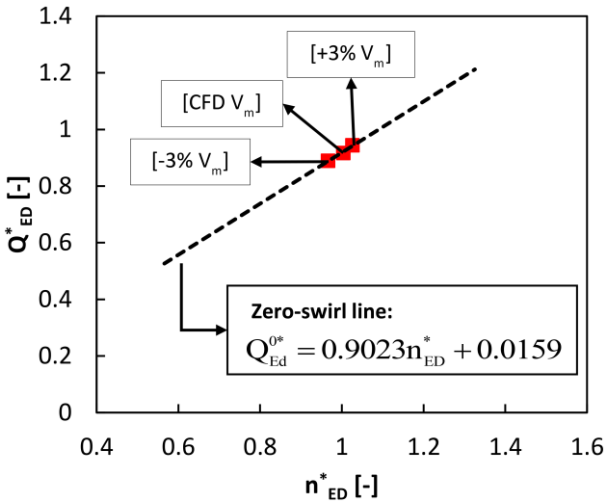

Figure 4.8. Extrapolation of no-swirl points into the zero-swirl line

As shown in Figure 4.8, the no-swirl line is now defined by a linear interpolation between the three no-swirl points which is then extrapolated to the complete range of n^*_{ED} values (zero-swirl line: $Q^{0*}_{ED} = 0.9023 n^*_{ED} + 0.0159$, R^2=0.98).

By using this linear relation between n^*_{ED} and Q^{0*}_{ED} together with Equation 4.2, the iso-swirl lines over the complete operating range of the turbine can be finally estimated. Figure 4.9 shows the iso-swirl and iso-efficiency lines on the $n^*_{ED} - Q^*_{ED}$ chart. The iso-swirl lines are later used in this chapter to determine the limits of part-load regimes.

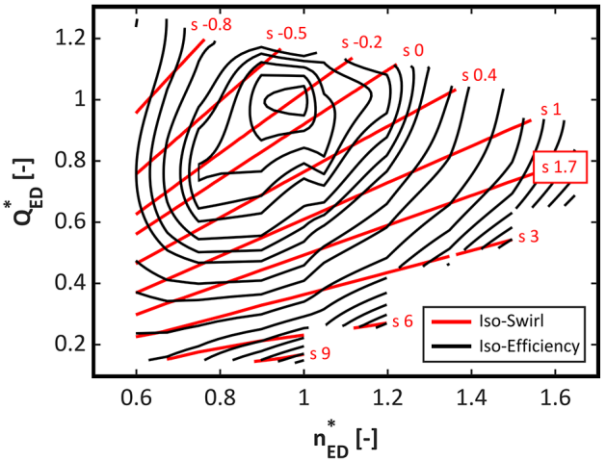

Figure 4.9. Iso-swirl and iso-efficiency lines on the $n^*_{ED} - Q^*_{ED}$ chart

Favrel et al. showed [26] that Equation 4.2 is valid only for a limited range of flow rates for their test case. However, they did not conclude a general limit that can be used for all turbines, since it would require a comprehensive study over a large database of turbines' performance tests. Consequently, it is not possible to conclude the limit of validity of Equation 4.2 for the present test-case without performing LDV measurements, which is out of the scope of this research.

4.4. Model test results

4.4.1. Highlight of pressure fluctuations' frequencies

A Cross-Spectral Density (CSD) analysis [125] of the pressure fluctuations measured in the draft-tube during model tests are performed to identify the frequencies of the pressure fluctuations and their nature, i.e. synchronous or convective. Furthermore, the coherence between two signals measured in the same cross-section is computed to assess the stability of the vortex at each section in the draft-tube. To compute CSD at each section, two signals are measured by two pressure sensors spaced by π/2 *rad* in angular position. In this case, the pressure fluctuations are purely convective if the phase difference between two signals estimated by CSD is equal to the difference in the angular location of the two sensors (π/2 *rad* in this case); while they have pure synchronous nature if the phase difference is equal to 0. If the phase difference between two signals has a value other than 0 or π/2 *rad*, the pressure fluctuations correspond to the superimposition of synchronous and convective components occurring at the same frequency.

It is observed that for a given operating condition the frequency of the pressure fluctuations below the runner remains constant for all the sections in the draft-tube before the elbow. Therefore, the results of CSD analysis are presented only for two sections before and after the elbow (sections E and G) to highlight the significance of further investigations in the next section. Figure 4.10 shows the cross spectral density and coherence at section E for the operating point at $n_{ED}^{*} = 1$ and $Q_{ED}^{*} = 0.53$. The values of power from the cross spectral density calculations are normalized by their maximum value. Two distinct peaks are identified in this figure, Peaks I and II. The first frequency peak (I) equal to 0.28 times the runner frequency (Figure 4.10.a) corresponds to the pressure fluctuations induced by the precession of the vortex rope (PVC) in the draft-tube at its frequency f_{PVC}. The phase difference between the two signals at the PVC frequency is equal neither to π/2 nor to 0, which demonstrates that these pressure fluctuations are a superimposition between synchronous and convective components. The convective component of pressure fluctuations is related to the local vortex behavior, while the synchronous component can propagate in the entire hydraulic system. Pasche et al [64] showed that the precession of the vortex rope in an asymmetrical geometry as the draft-tube elbow generates synchronous pressure fluctuations. Coherence between two pressure signals at this frequency is ≈1 (Figure 4.10.b). The second peak (II) at 0.56 f_{Runner} (equal to 2*0.28 f_{Runner}) corresponds to the first harmonic of the PVC frequency.

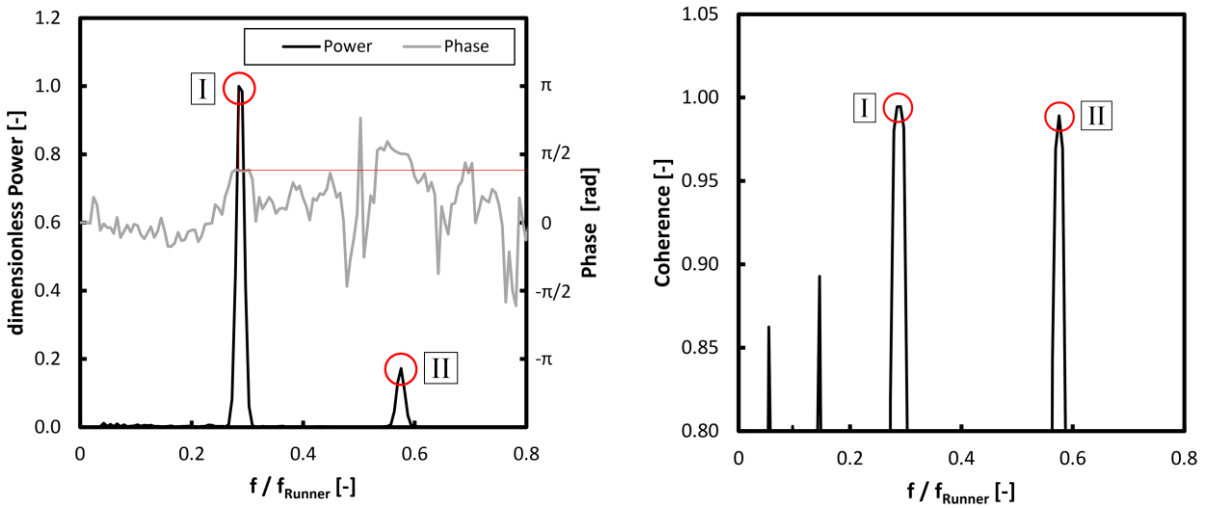

Figure 4.10. a. Cross spectral density and b. coherence for $n_{ED}^{*}=1$, and $Q_{ED}^{*}=0.53$ at section E

Figure 4.11 shows the results of the CSD and coherence for the same operating condition at section G, after the elbow. As in section E, peaks I and II are identified at the same frequencies in this figure. The value of phase difference between the two signals at peak I shows that the pressure fluctuations at section G are also composed of both convective and synchronous components, which demonstrates that the PVC extends beyond the elbow at this operating condition.

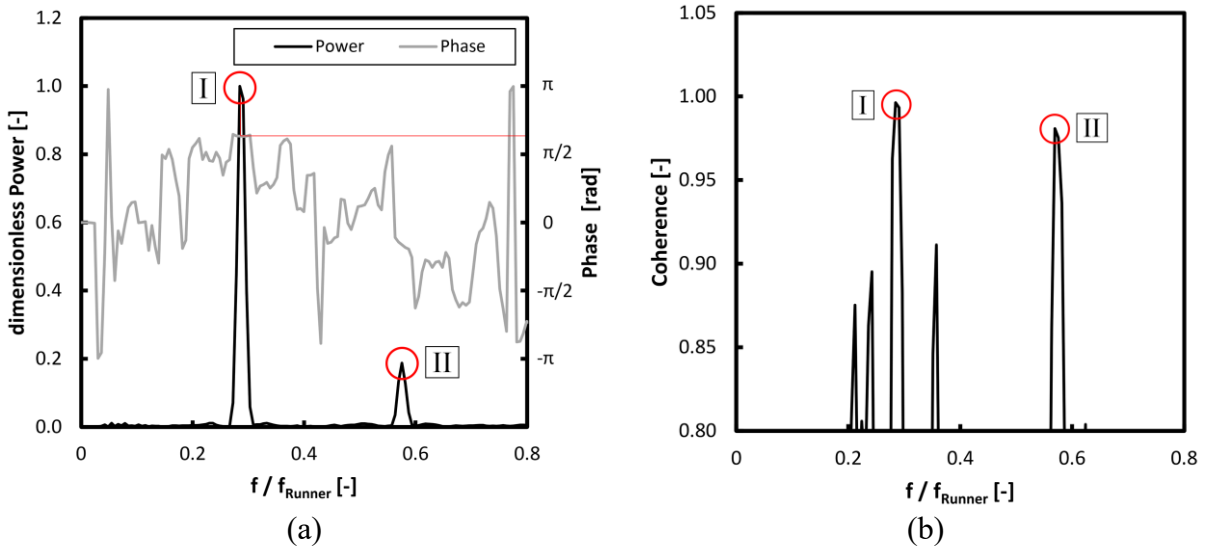

Figure 4.11. a. Cross spectral density and b. coherence for $n_{ED}^{*}=1$, and $Q_{ED}^{*}=0.53$ at section G

The results of CSD analysis are presented for the operating point at $n_{ED}^{*}=1$ and $Q_{ED}^{*}=0.43$. Figure 4.12 and Figure 4.13 present the CSD and coherence computed at the same sections in the draft-tube (sections E and G) for this operating condition.

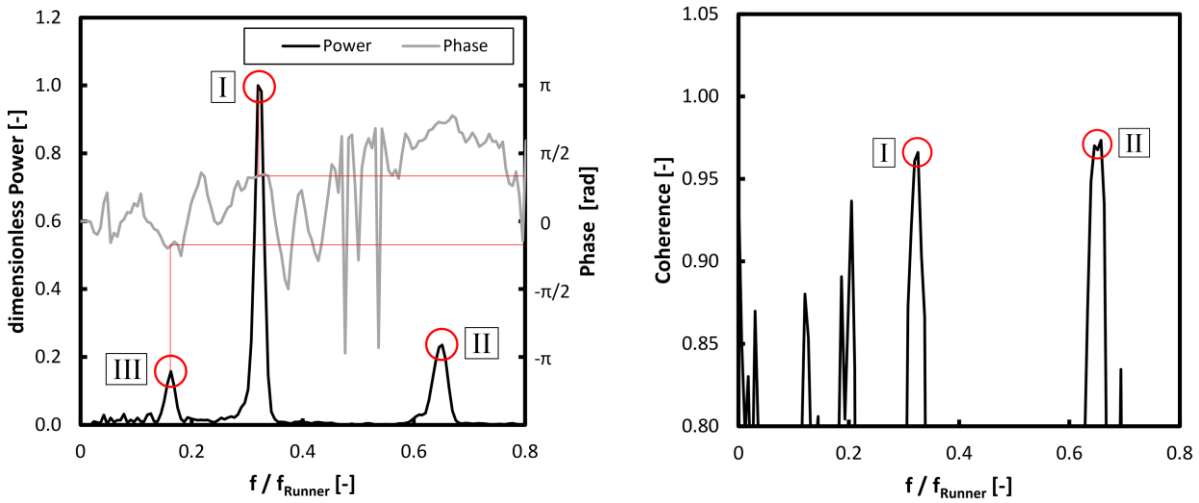

Figure 4.12. a. Cross spectral density and b. coherence for $n_{ED}^{*}=1$, and $Q_{ED}^{*}=0.43$ at section E

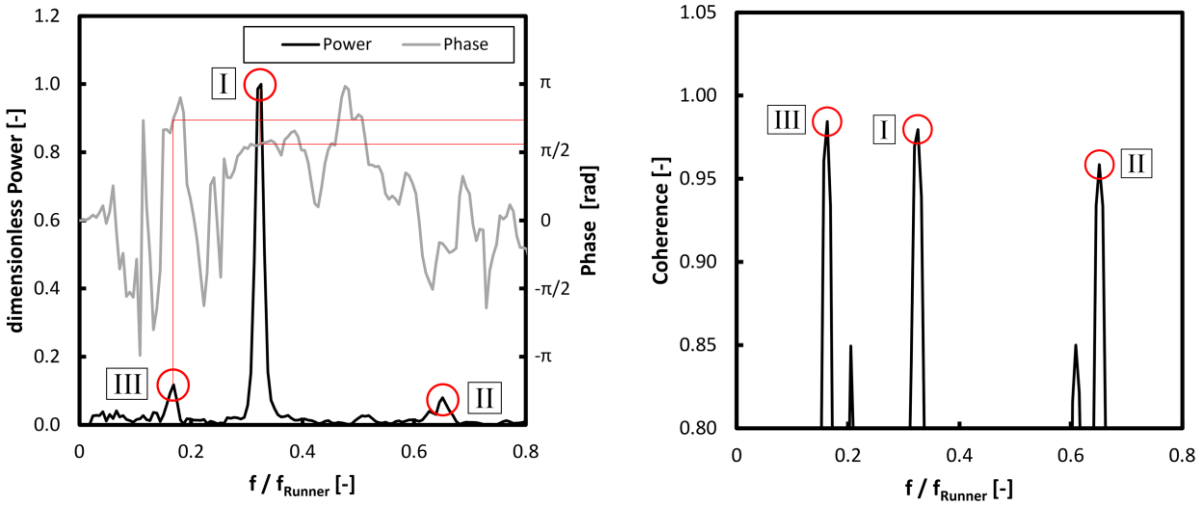

Figure 4.13. a. Cross spectral density and b. coherence for $n_{ED}^{*}=1$, and $Q_{ED}^{*}=0.43$ at section G

Similar to the previous operating point, peaks I and II, corresponding to the frequency of the PVC and its first harmonic, are identified in both sections E and G (see Figure 4.12.a and Figure 4.13.a, respectively). Unexpectedly, an additional low-frequency pressure peak (III) whose origin remains unknown at this stage is identified at both sections E and G. Its frequency value is approximately equal to half the PVC frequency f_{PVC}. Considering the phase difference between the two signals in Figure 4.12.a and Figure 4.13.a, it can be inferred that the pressure fluctuations at this frequency III feature both convective and synchronous components. This brings up the idea that these low-frequency pressure fluctuations are induced by the rotation of one (or several) vortical structure in the draft-tube. Figure 4.12.b shows that the coherence for the frequency peak III at section E is low while it is almost equal to 1 at section G, see Figure 4.13.b. This suggests

that the phenomenon responsible for the generation of the pressure fluctuations at the frequency III occurs probably in the elbow. Considering the results of CSD analysis over all the operating conditions, it is observed that type III pressure fluctuations appear only at a certain number of operating points which will be discussed in the next section.

4.4.2. Correlation of pressure fluctuations' frequencies with the swirl number

The above-mentioned CSD analysis is performed for all the tested operating points of the turbine (95 points) to estimate the frequencies of types I and III pressure fluctuations in the draft-tube. Then, frequencies of the pressure fluctuations (f) are expressed as the Strouhal number defined in Equation 4.4, representing the dimensionless frequency. The swirl number for all operating points is computed using Equation 4.2, as mentioned in section 4.3.5.

$$Str. = \frac{f.D^3}{Q} \qquad \textbf{4.4}$$

In Figure 4.14, the Strouhal numbers corresponding to the peaks I and III pressure fluctuations are plotted against the swirl number for n^*_{ED} values ranging from 0.6 to 1.65 and Q^*_{ED} values 0.2-1.1.

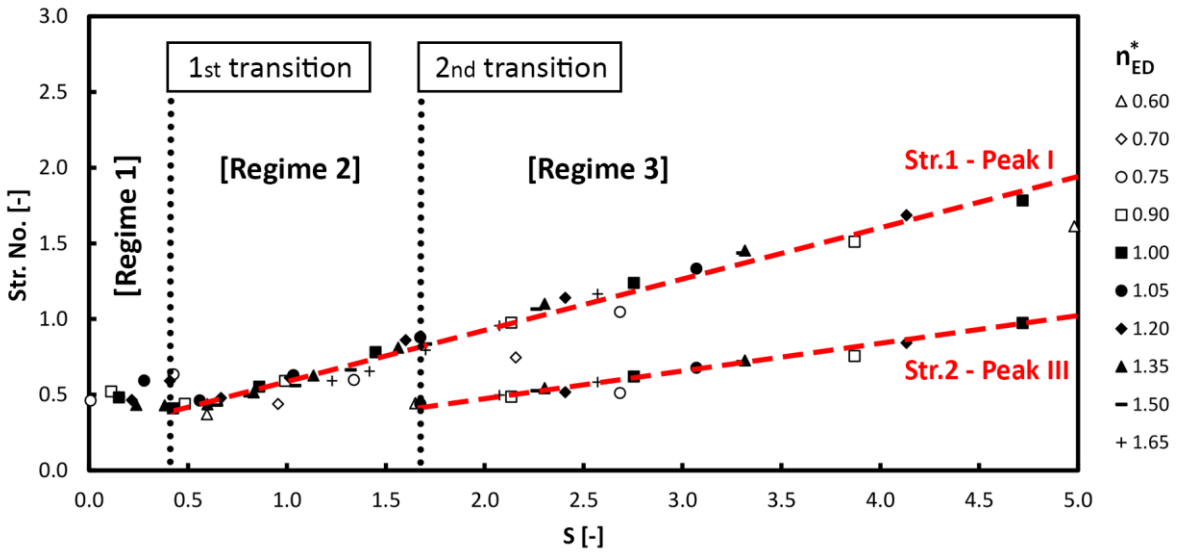

Figure 4.14. Strouhal number vs. swirl number for n^*_{ED} = 0.6 to 1.65

As shown in Figure 4.14, f_{PVC} (peak I) is observed for swirl numbers in the range between 0 to 0.4 but there is not any evident correlation between Strouhal and swirl numbers within this range. It is however noticed for swirl numbers beyond S=0.4 that Strouhal number of PVC follows a linear correlation with swirl number (Str.1), which is valid for all swirl numbers higher than 0.4.

This type of correlation has already been observed in Francis turbines [24-26]. More generally, the dynamics of PVC phenomenon mainly depends on the swirl intensity, and linear correlations between Strouhal number and swirl number were reported in several swirling flow applications. The empirical relation Str.1 (corresponding to peak I) enables to determine the PVC frequency on the complete range of part-load operating points on the corresponding prototype machine without measuring the specific operating points on the reduced scale model.

At swirl number S=1.7 (Figure 4.14), the frequency peak III starts appearing remarkably and its corresponding Strouhal number displays another linear correlation with the swirl number (St.2), whose slope corresponds to approximately half of the slope of the first correlation. Characteristics of the observed linear correlations (Str.1 and Str.2) are described in Table 4.5. It is mentioned in the previous section that frequency of peak III is almost half the f_{PVC}. This is confirmed in Figure 4.14 and Table 4.5 showing the fact that the slope of Str.2 is roughly half the slope of Str.1. The ratio between their amplitudes however depends on the operating condition of the turbine, and no clear correlation between swirl number and amplitude of the pressure fluctuations at the frequencies I and III beyond $S > 1.7$ have been found.

Table 4.5. Linear correlations between vortex frequencies and swirl intensity

Line	Corresponding regime	Linear correlation	R^2	Slope
Str.1 - Peak I	two and three	$Str. = 0.304S + 0.2954$	0.96	0.3040
Str.2 - Peak III	three	$Str. = 0.1485S + 0.1951$	0.96	0.1485

Considering the above-mentioned observations, it is confirmed that the draft-tube flow field during part-load operation of the turbine experiences two transitions in its behavior occurring at swirl numbers S=0.4 and S=1.7. Using the identified transitions, the part-load operating range of the turbine is divided into three regimes as shown in Figure 4.14; these part-load regimes are frequently named in literature as upper part-load, part-load, and deep part-load. Figure 4.15 shows the part-load regimes on the $n_{ED}^{*} - Q_{ED}^{*}$ chart of the turbine. Using Figure 4.15, it can be observed that two operating points discussed in the previous section (at $n_{ED}^{*} = 1$, $Q_{ED}^{*} = 0.53$ and $Q_{ED}^{*} = 0.43$) are located at part-load and deep part-load regimes, respectively.

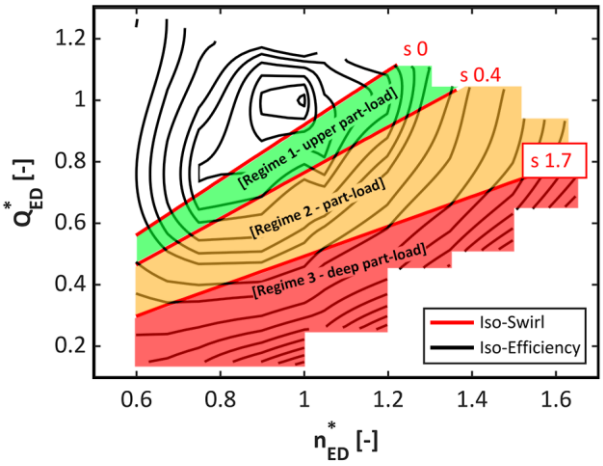

Figure 4.15. Part-load regimes on $n_{ED}^{*} - Q_{ED}^{*}$ chart

Favrel et al. [26] studied the flow field in the draft-tube for the swirl numbers within the range $0.6 < S < 1.5$ which corresponds to the second regime, and they confirmed the occurrence of the linear correlation between f_{PVC} and the swirl number; however, they did not investigate the behavior of vortex core during deep part-load condition in their paper. The objective of the following section is to identify the nature and the source of the pressure fluctuations at the frequency peak III during the deep part-load operation of a Francis turbine.

4.5. Unsteady numerical investigation of deep part-load regime

4.5.1. Unsteady CFD simulation set-up

Unsteady-state numerical simulation is performed for one operating point at deep part-load regime to study the source of the low-frequency pressure fluctuations (peak III) occurring beyond S=1.7. The selected point is located at $n_{ED}^{*} = 1$ while guide vanes opening is 30% corresponding to $Q_{ED}^{*} = 0.43$. The unsteady simulations are performed by solving URANS equations using Ansys CFX 19.0. The Scale-Adaptive Simulation (SAS) is utilized to capture the LES-like behavior of the flow in the draft-tube where the flow is strongly unsteady and turbulent [126, 127]. In this case, the inlet boundary condition is set to mass flowrate which provides appropriate predictions in transient simulations of Francis turbines [128-130], while the outlet boundary condition is kept as average static pressure. Values of flowrate and effective head for inlet and outlet boundary conditions are selected from model tests at the same n_{ED}^{*} and Q_{ED}^{*}. Both the interfaces at GV-to-RV and RV-to-DT are selected as transient rotor-stator. The simulation

time-step is selected as 4e-4 seconds (equal to 1.752˚ runner rotation) which results in an RMS Courant number equal to 3.9. To obtain an accurate estimation of the amplitudes of pressure fluctuations in the draft-tube, the flow field is computed for ≈120 revolutions of the runner (equal to ≈39 PVC rotation). The computation time for the unsteady-state simulation is 5.404e+8 CPU-seconds using 40 CPU cores.

4.5.2. Validation of unsteady CFD results

Pressure fluctuations in the draft-tube are recorded using 36 monitoring points at all the sections in Figure 4.3. The monitoring points at each section are spaced by 90 degrees. This enables the decomposition of pressure fluctuations into convective and synchronous components, as described in the next sub-section. The monitoring points in sections B, D, E, and G are located at the same places as in model tests. To compare the results of CFD with experiments, an FFT analysis of pressure fluctuations simulated at each monitoring point is performed. Figure 4.16 shows the comparison of FFT of pressure pulsations between CFD and model test results at two sections in the draft-tube; section A which is located below the runner, and section E which is just upstream the elbow. As expected, three pressure peaks are identified in Figure 4.16. Peaks I and III correspond to the fundamental frequency of the precessing vortex and the low-frequency fluctuations appearing at deep part-load, respectively, whose correlations with the swirl number are presented in Figure 4.14. Peak II in Figure 4.16 corresponds to the first harmonic of the precessing vortex frequency.

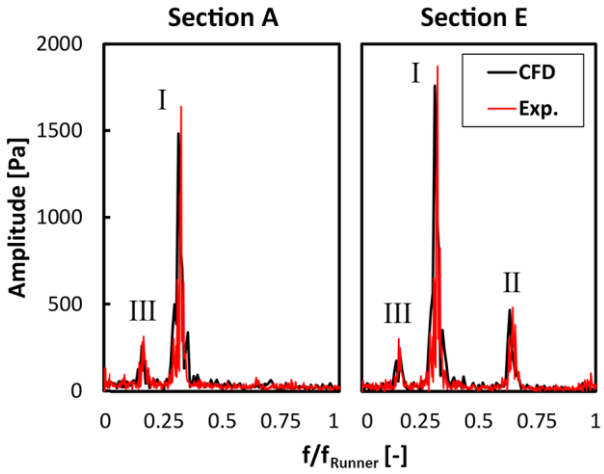

Figure 4.16. FFT of pressure pulsations at sections A and E: comparison of CFD with experimental results

Table 4.6, based on Figure 4.16, shows the deviation between frequencies and amplitudes of pressure pulsations obtained by CFD and experiments. CFD overestimates the frequencies by

3.6% and 4.4% for peaks I and III, respectively. The comparison of the amplitudes also shows an over-estimation in CFD results by 9.5% and 26.1% for peaks I and III. Considering the deviations presented in Table 4.6 and its comparison with similar studies in literature [62, 129-134], it can be concluded that the CFD results in the current study are in fair agreement with experiments except for the prediction of the amplitude of peak III. The reason for this deviation in the estimation of the amplitude of peak III can be due to inherently stochastic nature of this phenomenon which results in unstable pressure fluctuations in the draft-tube.

Table 4.6. Deviation between CFD and experiments

	Deviation in frequency [%]	Deviation in amplitude [%]
Peak I	3.6	9.5
Peak III	4.4	26.1

Moreover, the time-averaged efficiency is calculated over the whole simulation time to compare the unsteady CFD and the model tests results in manner of turbine performance. It is seen that CFD overestimates the efficiency by 3.8%, which is acceptable in the context of the current research.

4.5.3. Nature of pressure pulsations at deep part-load

Pressure fluctuations induced by a PVC can be decomposed in the time domain into two components: synchronous and convective (or asynchronous) [12, 15, 20]. The convective component is induced by the local rotation of the inhomogeneous pressure fields with the PVC; while the synchronous component, which features equal phase and amplitude in the same cross-section, is generated by the precession of the vortex in an asymmetric geometry and propagates upstream in the complete hydraulic circuit [64]. To understand the nature of type III low-frequency fluctuations, the raw pressure signals from CFD monitoring points are decomposed into the two above-mentioned components. Using four pressure monitoring points at each section in the draft-tube, the synchronous and convective components can be calculated through Equations 4.5 and 4.6, respectively:

$$P^{synch.}(t) = \frac{1}{4}\sum_{i=1}^{4} P_i(t) \quad \textbf{4.5}$$

$$P_i^{conv.}(t) = P_i(t) - P^{synch.}(t) \quad \textbf{4.6}$$

where P_i and $P_i^{conv.}$ (with i=1…4 in this case) are the raw and convective pressure signals corresponding to the sensor i, respectively, while the synchronous pressure $P_i^{synch.}$ is common to all pressure sensors in the same section.

The FFT of each synchronous and convective component is calculated at different sections along the draft-tube. Figure 4.17 and Figure 4.18 show the FFT of the synchronous and convective components at four selected sections: sections A (below the runner), C (after the draft-tube cone), E (before the elbow), and G (after the elbow). The strong stochastic nature of the flow downstream of the elbow makes it difficult to identify periodic fluctuations, so the results in sections G, H and I are not presented. However, it is of importance to mention that the synchronous component of both types I and III pressure fluctuations can be identified everywhere in the draft-tube.

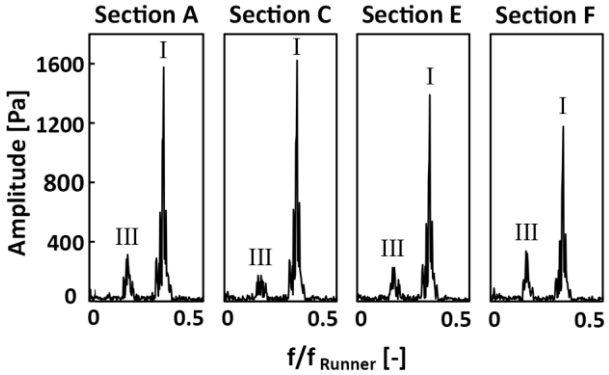

Figure 4.17. Synchronous component of the pressure pulsations identified at four sections in the draft-tube

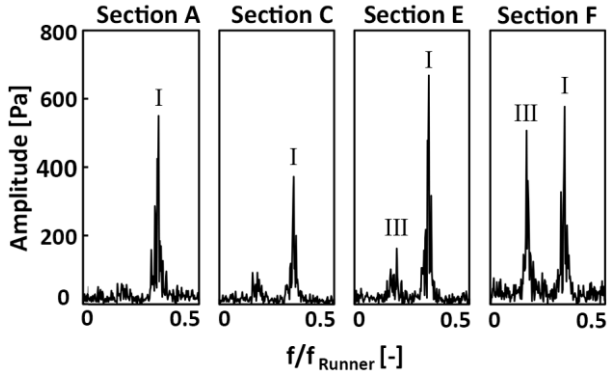

Figure 4.18. Convective component of the pressure pulsations identified at four sections in the draft-tube

Figure 4.17 and Figure 4.18 show that types I and III pressure fluctuations feature both convective and synchronous components, with however different amplitudes depending on the section in the draft-tube. Type I has convective and synchronous components in all sections below the runner. On the contrary, type III is synchronous in the sections very close to the runner outlet, whereas a convective component starts appearing from section D and reaches its maximum amplitude in sections E and F. Since the convective component is directly related to the local vortex behavior, it can be inferred that the phenomenon responsible for type III fluctuations occurs

in the elbow, which supports the conclusion in section 4.4.1. Moreover, Figure 4.17 shows that this phenomenon induces synchronous pressure pulsations at all sections in the draft-tube and can therefore lead to the occurrence of resonance with the hydraulic system if the low-frequency of type III matches with one of the hydraulic circuits eigenfrequencies.

4.5.4. Dominance regions of two types pressure fluctuations

The dominance region for each type of pressure fluctuation in the draft-tube is investigated to understand the dynamics of the phenomenon generating type III pressure fluctuations. Using the results of unsteady CFD simulations, FFT of the pressure fluctuations obtained at all the nodes on the draft-tube wall (135,000 nodes) is computed. The ratio between the amplitudes of the FFT at the frequencies corresponding to the peaks type I and III ($Amp_{type-III} / Amp_{type-I}$) over the complete draft-tube wall is calculated and shown in Figure 4.19. Values near 0% indicates that the pulsations of type I (precessing vortex frequency) are dominant whereas type III pulsations are dominant in regions with the ratios over 100%. It is interpreted from Figure 4.19 that the pressure fluctuations caused by the precessing vortex are dominant mainly in the draft-tube cone and in the straight pipe before the elbow (blue zone). In the elbow, the amplitude of the pressure fluctuations associated with the low-frequency phenomenon (type III) increases and are dominant in the diffuser (red zones); with its inception occurring at the inlet of the elbow, as indicated in Figure 4.19. Accordingly, it is confirmed that the phenomenon responsible for the generation of type III pressure pulsation occurs in the elbow.

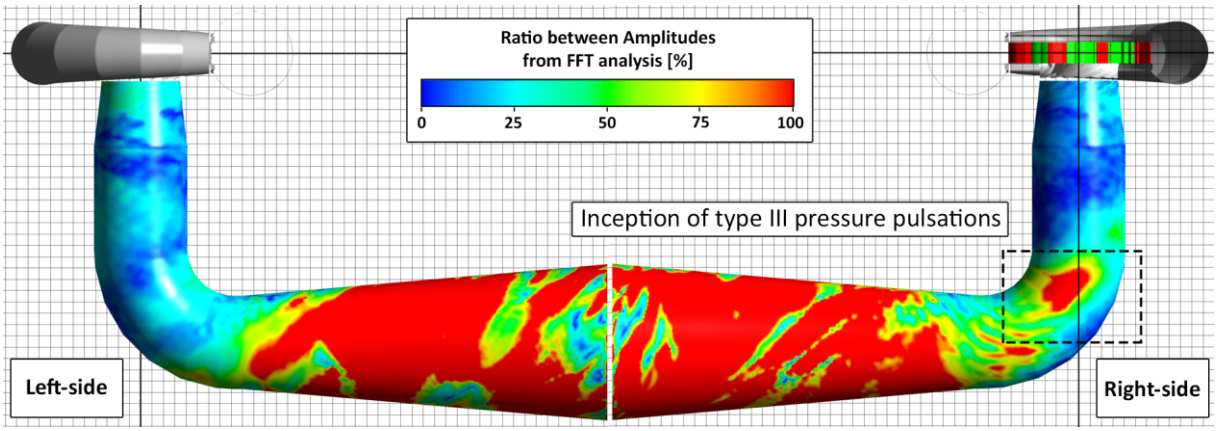

Figure 4.19. Ratio between amplitudes of types III and I pressure fluctuations on the draft-tube wall

4.5.5. Vortex center tracking method and results

This section is dedicated to the investigation of the dynamics of the phenomenon that causes type III pressure fluctuations in the draft-tube. The center position of the vortical structures in the draft-tube cone and elbow is first estimated by applying the methodology based on the calculation of Γ_1 function to the flow velocity fields obtained from CFD at different sections from A to G.

In highly turbulent swirling flows, such as the flow field in the draft-tube of a hydraulic turbine at deep part-load operation, the Proper Orthogonal Decomposition (POD) can be used to separate the contributions of turbulent fluctuations and unsteady swirling motion to the total energy. Graftieaux et al. [93] combined POD with a new non-Galilean invariant vortex identification function (Γ_1) to accurately identify the center of the vortex based only on the topology of the velocity field, Equation 4.7. The Γ_1 dimensionless scaler describes the rotation rate of the flow around a given point by representing the sine of the angle (θ_M) between the velocity vector $\overrightarrow{U_M}$ and the radius vector $\overrightarrow{PM}$ [135]; using Γ_1 enables to identify the vortex core without computing velocity gradients.

$$\Gamma_1(P) = \frac{1}{N}\sum_S \frac{\left(\overrightarrow{PM} \times \overrightarrow{U_M}\right)\cdot \vec{z}}{\left\|\overrightarrow{PM}\right\| \cdot \left\|\overrightarrow{U_M}\right\|} = \frac{1}{N}\sum_S \sin(\theta_M) \qquad \textbf{4.7}$$

The Γ_1 function is defined on point P as in Equation 4.7, where S is a fixed size two-dimensional rectangular zone surrounding the point P, in which N points of M lie. Vectors $\overrightarrow{PM}$, $\overrightarrow{U_M}$, and $\vec{z}$ represent the spatial vector between points P and M (radius), the velocity vector at point M, and the unit vector normal to the measurement plane, respectively. The dimensionless $|\Gamma_1|$ is bounded by 1 and this bound can be reached at the location of the vortex center.

Figure 4.20 presents an example of distribution of $|\Gamma_1|$ calculated for an arbitrary time t in section A, below the runner. The center of the PVC can be clearly identified at the red point on this figure.

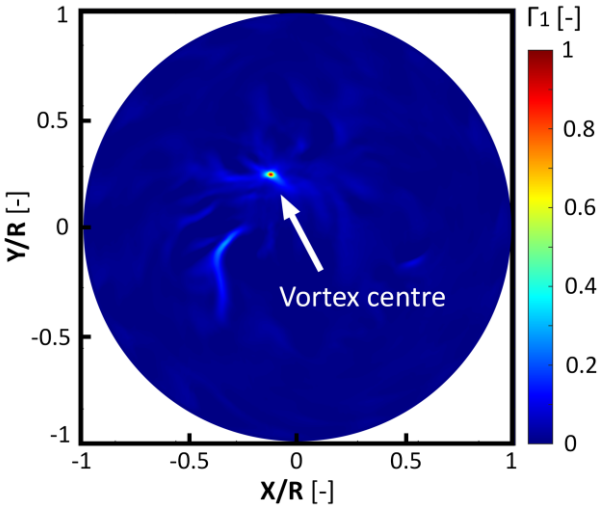

Figure 4.20. | Γ1| function calculated at section A for an arbitrary time t

The evolution of the vortex position over time is tracked in a given section by identifying its center at each time step. The paths of the vortical structures are determined in sections A, C, E, F, and G. Figure 4.21 shows the center of a PVC rotating on a quasi-circular path near the center of the draft-tube at section E during two periods (T) of rotation. Similar trajectories are found in other sections upstream the draft-tube elbow and are not presented.

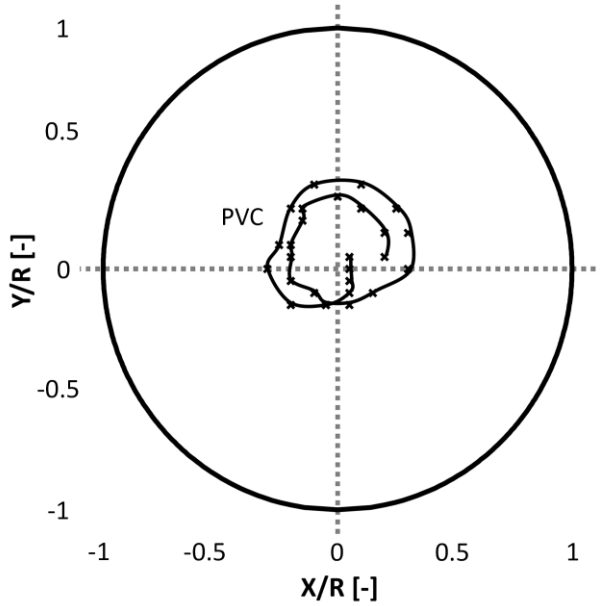

Figure 4.21. PVC path at section E

The evolution of the corresponding angular location of the PVC center over time in section E is shown in Figure 4.22. The data can be fitted by a linear regression curve whose slope corresponds to the angular velocity of the PVC ($\omega \approx 24.165$ $rad.s^{-1}$, which is equivalent to the frequency of type I pressure fluctuations).

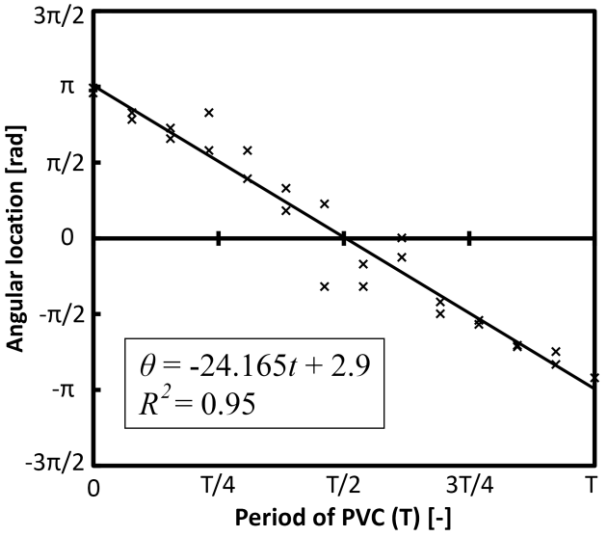

Figure 4.22. Angular locations of the PVC center at section E

Figure 4.23 and Figure 4.24 schematically represent the path of the PVC at sections A (below the runner) and E (before the elbow). It is noticed that center of the PVC trajectory is gradually inclined toward the draft-tube wall while moving from section A to E, and it has its closest location to the draft-tube wall at section E. The rotating low-pressure region generated by the PVC at deep part-load operating condition is particularly large. Therefore, when PVC approaches the draft-tube wall in section E, this low-pressure region hits the wall (within the quarter 4, see Figure 4.24) and holds to it until it separates from the wall either at quarters 1 or 2. When the vortex core hits the draft-tube wall, while entering the elbow, it breaks into three smaller vortices downstream in the elbow, named in the following vortices V0, V1, and V2.

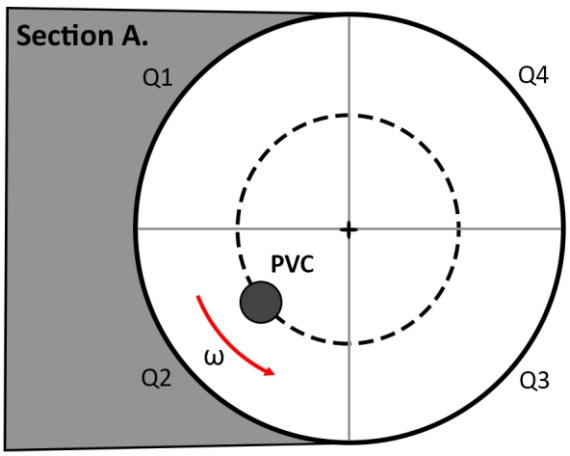

Figure 4.23. Schematic path of the PVC center at section A (below the runner)

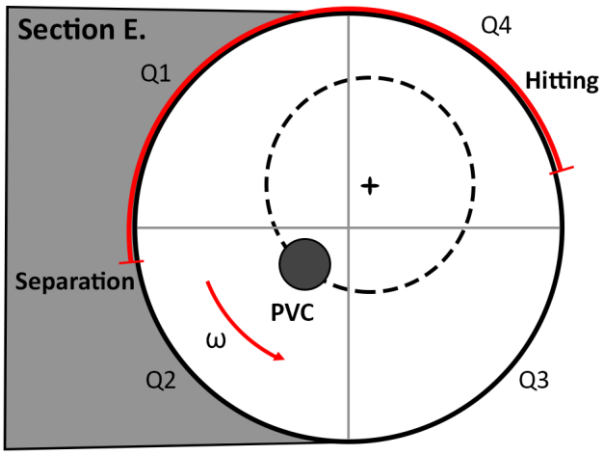

Figure 4.24. Schematic path of the PVC center at section E (before the elbow)

The paths of the center of these smaller vortices in the elbow are identified using $|\Gamma_1|$ function to determine if they follow any periodical motion explaining the occurrence of type III pressure fluctuations. The trajectories of the vortices V0, V1 and V2 resulting from the main PVC breakdown over two periods of PVC rotation (T) at section F are shown in Figure 4.25. It is noticed in Figure 4.25 that V0 rotates on a small circular path, while the other two vortices V1 and V2 rotate on larger paths around V0.

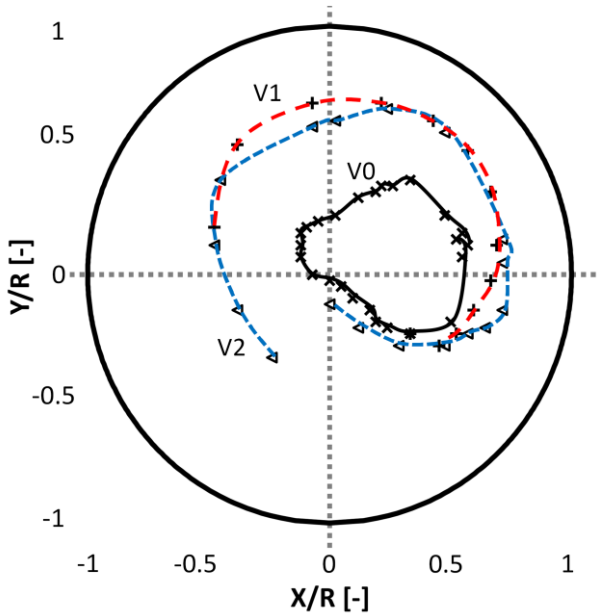

Figure 4.25. Vortices' paths at section F

The evolution of the angular locations of these vortices over two periods (T) of the PVC are presented in Figure 4.26. For each vortex, the evolution of the vortex center angular position are fitted by a linear regression curve. The value of the corresponding slopes is similar for all vortices and equal to approximately $\omega/2$, with ω the angular velocity of the main vortex (PVC) upstream the elbow. Accordingly, the rotation of V0 with an angular velocity of ω/2 induces type III pressure fluctuations. Moreover, it is noted in Figure 4.26 that V1 and V2 rotate with the same

angular velocity but with however their position at a given instant spaced by an angle of π, which corresponds to the behavior of a twin vortex generating pressure pulsations at a frequency equal to the double of the rotational frequency of each single vortex. Consequently, the simultaneous rotation of V1 and V2 generates type I pressure fluctuations in the elbow. Periodic rotation of V0, V1, and V2 vortices explains the presence of both types of pressure fluctuations (I and III) in the elbow. Similar to the pressure fluctuations at f_{PVC}, pressure fluctuations in the elbow exhibit both convective and synchronous components. The rotation of V0, V1 and V2 vortices induces local convective components, while the interaction of the precession of these vortices with the asymmetrical geometry of the elbow generates synchronous components propagating upstream.

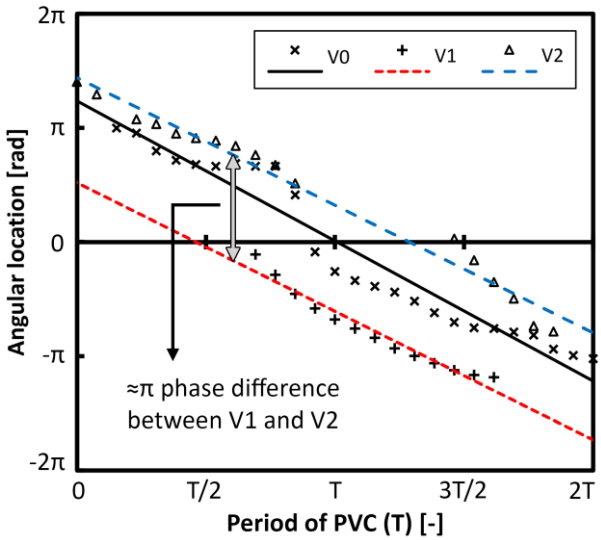

Figure 4.26. Angular locations of the vortices' centers at section F

Figure 4.27 schematically presents the paths of three small vortices in section F. The paths of the main PVC (Figure 4.21) and V0 (Figure 4.25) describes quasi-circles; while V1 and V2 rotate on incomplete quasi-circles. It is observed that V0 rotates on a path close to the center of the draft-tube, while the two other vortices (V1 and V2) move on larger paths around V0. It is also of interest to mention that V1 and V2 vortices preserve appearing and disappearing through time. It is seen that they mostly appear near the quarters 2 or 3 after separation of the main PVC from the draft-tube wall; and then disappear mainly in quarter 1.

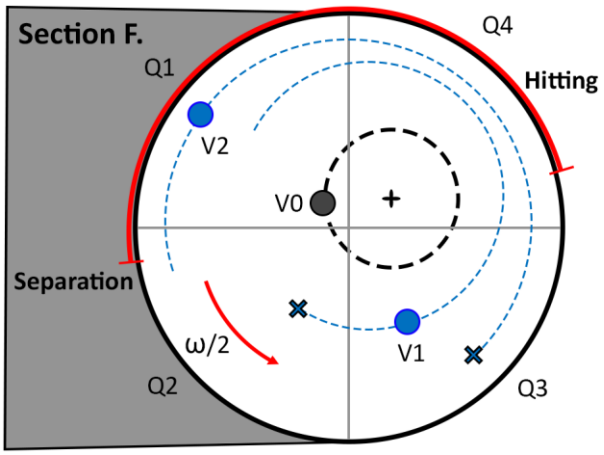

Figure 4.27. Schematic paths of vortices' centers at section F (middle of the elbow)

Although a periodic motion of the flow field in the elbow can be observed, resulting in two types of pressure fluctuations, no clear convective motion of the vortical structures can be highlighted after the elbow region in the draft-tube diffuser; whilst the synchronous components of types I and III pressure fluctuations can be observed everywhere in the draft-tube. The flow field after the elbow is strongly chaotic: the existing vortices break into many smaller vortices downstream the elbow. This chaotic condition persists until the outlet of the draft-tube.

According to the above-mentioned observations, it is confirmed that the main vortex breaks down into smaller vortices in the elbow. However, both the elbow and the downstream diffuser may have an influence on this phenomenon, since it is known that diffusers have a great impact on PVC dynamics, including their trajectory. Therefore, changing the diffuser angle of the downstream diffuser may influence the observed phenomenon. However, proving this statement would require further investigations.

4.6. Discussion and perspectives

In the context of promoting the development of renewable energy sources, it is necessary to extend the operating range of hydro-power plants from very low to high loads to contribute to balancing the electricity production with the consumption for the sake of the electrical grid flexibility. The present research, within this context, is conducted to promote the understanding of the flow instabilities in the draft-tube of a Francis turbine during deep part-load operations, which may be increasingly required in the future. By analysing the results of model tests along with CFD simulations for a medium specific speed Francis turbine, it is highlighted that during the deep part-load regime, the PVC losses coherence after hitting the draft-tube wall in the elbow

and breaks down into smaller vortices in the present test-case. Harmonic rotation of the smaller vortices in the elbow, generates low-frequency pressure fluctuations featuring both convective and synchronous components, which shows the importance of further study on draft-tube flow field during deep part-load operation of Francis turbines. However, according to the literature, this type of flow behaviour and low-frequency pressure fluctuations are not observed in all Francis turbines at deep part load [32] and further investigations are necessary to determine the particular conditions promoting this flow behaviour.

In addition to the mentioned scientific outcomes of this chapter, the following industrial applications may be envisioned:

- A novel method for the determination of the no-swirl zone and other iso-swirl lines by using CFD is presented. The iso-swirl lines along with the swirl number definition are adopted to characterize the pressure pulsations' frequency all over the operating range of the turbine. The observed empirical relations between the swirl number and the Strouhal number corresponding to the draft-tube pressure pulsations can be directly transposed to the prototype scale to predict the draft-tube flow behavior on the complete part-load operating range on the full-size machine [24].
- A new type of low-frequency pressure pulsations during deep part-load operation of a Francis turbine is highlighted. A linear correlation between the frequency of these pressure fluctuations and the swirl number is also established. The latter can be transposed from the reduced scale model to the corresponding prototype, as well, to predict the value of this low frequency on the full-size machine.
- Since the dynamic phenomenon responsible for the low-frequency pulsations occurs in the elbow, both convective and synchronous pressure components are observed. The latter is observed in the draft tube cone, upstream of the elbow, and may propagate in the entire hydraulic system. Therefore, hydro-acoustic resonances may occur in deep part load conditions if the low frequency matches with one of the hydraulic circuits eigenfrequencies. This can happen during with operation of the machine of presence of cavitation. Predicting such resonance conditions on the prototype machine will however requires the implementation of 1D simulation models [4, 51, 113] to estimate the eigenfrequencies of the system, as proposed in [24, 136].

4.7. Summary

This chapter focuses on the behavior of the draft tube flow of a medium specific-speed Francis turbine during its deep part-load operation. In particular, the appearance of pressure

fluctuations at a frequency lower than the precession frequency of the main vortex rope (PVC) beyond a given swirl number is highlighted and their generation mechanisms are investigated in detail by analysing unsteady-state CFD results.

The vortex rope behavior is first investigated over the complete part load range by performing pressure measurements during model tests of the corresponding machine. The frequencies of the pressure fluctuations observed in the draft tube are identified by cross spectral analysis of the pressure data at each tested operating point and are then correlated to the swirl number S. The latter is estimated at each operating point by using a simplified analytical expression and the no-swirl conditions estimated by a method based on steady-state simulations around the Best Efficiency Point.

The Strouhal number of the precession frequency of the main PVC shows a linear correlation with the swirl number beyond $S>0.4$ that is valid for all values of speed factor. Beyond a swirl number of $S=1.7$, corresponding to the transition from part-load to deep part-load conditions, a second type of pressure fluctuations occurring at about half of the main precession frequency appears in all the sections of the draft tube. The Strouhal number of this frequency also shows a linear correlation with the Strouhal number beyond $S>1.7$ that is valid for all values of speed factor. The co-existence of these two types of pressure fluctuations at deep part load for swirl numbers higher than $S=1.7$ indicates that another phenomenon occurs beyond the transition from part load to deep part load, generating low-frequency pressure fluctuations alongside the PVC.

Unsteady CFD simulations at one deep part-load operating point are then performed to investigate the source of the low-frequency pressure fluctuations in the draft-tube during deep part-load conditions. By performing FFT analysis of the pressure fluctuations on the complete draft-tube wall and pressure decomposition into convective and synchronous components, it is demonstrated that the low-frequency pressure fluctuations are generated in the draft tube elbow, while its synchronous component can be observed in the complete draft-tube. The evolution of the vortical structure position over time at different sections in the draft-tube is then traced by using the $|\Gamma 1|$ function. By utilizing the vortex center tracking, the trajectory of the main PVC in the draft tube is reconstructed. It is observed that the main PVC loses its coherence after hitting the draft-tube wall in the elbow. As a result, the PVC breaks down into three smaller vortices which rotate with almost half the speed of the PVC. One of these vortices rotates around the draft tube center and induces the low-frequency pressure fluctuations in the elbow. In parallel, the two other vortices rotate with the same rotational speed but with however their position at a given instant spaced by an angle of π, which corresponds to the behavior of a twin vortex generating

pressure pulsations at a frequency equal to the double of the rotational frequency of each single vortex. Therefore, they generate pressure fluctuations with the same frequency as the one of the PVC. The periodic rotation of these three small vortices in the elbow is responsible for the generation of two types of pressure fluctuations in the draft-tube of Francis turbine during deep part-load operation. In addition, the rotation of these vortices in the asymmetrical geometry of the draft tube elbow induces the generation of a synchronous pressure pulsation, which may potentially induce hydro-acoustic resonance if its frequency matches with one of the hydraulic circuits eigenfrequencies.

5. Conclusions and perspectives

5.1. Conclusions

This thesis is devoted to study the physical mechanisms of three phenomena that induce synchronous pressure pulsations in the draft-tube of a hydraulic turbine. In the first part of the thesis (chapter 2) an oscillatory behavior of the vortex breakdown is identified using the results of pressure measurements in the draft-tube. It is observed that the oscillatory behavior of the vortex breakdown generates low-frequency synchronous pressure pulsations that propagates in the entire hydraulic system. Numerical simulations are carried out to understand the flow field behavior near the breakdown location. It is confirmed that a shear layer forms around the vortex center at the location of breakdown which stretches the vortex center in a circumferential direction.

Cavitation surge characteristics under different swirl intensities are studied within the second part of the thesis (chapter 3). Pressure measurements along with high-speed visualization of cavity volume are conducted for a wide range of operating conditions (for a variety of swirl intensities, flowrates, and cavitation numbers). The 1st natural frequency of the draft-tube is identified by using the results of pressure measurements and high-speed visualizations; and it is observed that the 1st natural frequency of the draft-tube decreases with decreasing the cavitation number. The low-frequency synchronous pressure pulsations due to oscillatory behavior of the vortex breakdown (which is introduced in chapter 2) are identified for all operating conditions. It is observed that cavitation surge starts when the 1st natural frequency of the draft-tube coincides with the frequency of the abovementioned synchronous pressure pulsations. A transition between the stable and unstable modes of the draft-tube is identified. Several correlations between the 1st natural frequency of the draft-tube and cavitation number and cavity void fraction are established. A 1D model is employed to predict the wave speed and the 1st natural frequency of the draft-tube. The results of 1D modelling are compared with the results of pressure measurements and high-speed visualizations of the cavity volume.

In the third part of the thesis (chapter 4), results of model tests of a Francis turbine are used to find the no-swirl operating conditions. A novel methodology based on definition of swirl number is established to divide the part-load operating points of the turbine into a. upper part-load, b. part-load, and c. deep part-load. Low-frequency synchronous pressure pulsations are identified in the draft-tube of the machine during its deep part-load operation which can propagate in the entire hydraulic system and induce cavitation surge in presence of cavitation. By using the results of unsteady-state CFD simulations, it is confirmed that generation of a twin vortex rope in the elbow is responsible for generation of the low-frequency pressure pulsations.

5.2. Perspectives

Study of the following topics would help to strengthen the conclusions expressed for each of the investigated phenomena in the current thesis:

- Low-frequency synchronous pressure pulsations in a simplified draft-tube
  a. Identifying fluctuations of the breakdown location in cavitating flow.
  b. Performing LDV measurements in different sections of the draft-tube to capture the velocity profiles' fluctuations near the breakdown location.
- Cavitation surge characteristics under different swirl intensities
  a. Performing high-speed visualizations of the cavity volume by using two cameras.
  b. Computing a local cavitation compliance for several nodes in the draft-tube and calculate the 1st natural frequency of the system by using the cavitation compliances corresponding to several nodes.
- Generation of twin vortex rope in the draft-tube elbow of a Francis turbine during deep part-load operation
  a. Understanding the influence of draft-tube geometry on the limits of the part-load regimes.
  b. Identifying the part-load regimes for several Francis turbines with different specific speeds to generalize the expressed conclusions within this thesis for a wide range of turbines.
  c. Studying the low-frequency pressure pulsations in presence of cavitation and investigating occurrence of resonance.

References

[1] Rheingans, W. J., 1940, "Power swings in hydroelectric power plants," Trans. ASME, 62(3), pp. 171-184.

[2] Yonezawa, K., Konishi, D., Miyagawa, K., Avellan, F., Dörfler, P., Tsujimoto, Y., 2012, "Cavitation surge in a small model test facility simulating a hydraulic power plant," International Journal of Fluid Machinery and Systems, 5(4), pp. 152-160.

[3] Nishi, M., Liu, S., 2013, "An Outlook on the Draft-Tube-Surge Study," International Journal of Fluid Machinery and Systems, 6(1).

[4] Alligné, S., Nicolet, C., Tsujimoto, Y., Avellan, F., 2014, "Cavitation surge modelling in Francis turbine draft tube," Journal of Hydraulic Research, 52(3), pp. 399-411.

[5] Müller, A., 2014, "Physical Mechanisms governing Self-Excited Pressure Oscillations in Francis Turbines," PhD, EPFL.

[6] Müller, A., Yamamoto, K., Alligne, S., Yonezawa, K. Tsujimoto, Y., Avellan, F., 2016, "Measurement of the Self-Oscillating Vortex Rope Dynamics for Hydroacoustic Stability Analysis," J. Fluids Engineering, 138(2).

[7] Yonezawa, K., 2019, "An experimental investigation of cavitation surge in draft tube of Francis turbine," 29th IAHR Symposium on Hydraulic Machinery and System, IOP Conf. Series: Earth and Environmental Science, Kyoto.

[8] Susan-Resiga, R., Ciocan, G., Anton, I., Avellan, F., 2006, "Analysis of the swirling flow downstream a Francis turbine runner," J. Fluids Engineering, 128(1), pp. 177-189.

[9] Arpe, J., Nicolet, C., Avellan, F., 2009, "Experimental evidence of hydroacoustic pressure waves in a Francis turbine elbow draft tube for low discharge conditions," J. Fluids Engineering, 131(8).

[10] Bosioc, A. I., Susan-Resiga, R., Muntean, S., Tanasa, C., 2012, "Unsteady Pressure Analysis of a Swirling Flow With Vortex Rope and Axial Water Injection in a Discharge Cone," J. Fluids Engineering, 134(2).

[11] Lowys, P., Andre, F., Ferreira da Silva, A., Duarte, F., Payre, P, 2014, "Hydro plant operating range extension transverse approach for increasing turbine flexibility," Proceedings of Hydrovision USA.

[12] Favrel, A. T., 2016, "Dynamics of the cavitation precessing vortex rope for Francis turbines at part load operating conditions," PhD, EPFL.

[13] Goyal, R., Cervantes, M. J., Gandhi, B. K., 2017, "Vortex Rope Formation in a High Head Model Francis Turbine," J. Fluids Engineering, 139.

[14] Iliescu, M. S., Ciocan, G. D., Avellan, F., 2008, "Analysis of the Cavitating Draft Tube Vortex in a Francis Turbine Using Particle Image Velocimetry Measurements in Two-Phase Flow," Journal of Fluids Engineering, ASME, 130.

[15] Nishi, M., Matsunaga, S., Senoo, Y., Kubota, T., 1984, "Surging characteristics of conical and elbow-type draft tubes," 12th IAHR Symposium on Hydraulic Machinery and SystemStirling, Scotland.

[16] Foroutan, H., Yavuzkurt, S., 2014, "Flow in the Simplified Draft Tube of a Francis Turbine Operating at Partial Load—Part I: Simulation of the Vortex Rope," J. Fluids Engineering, 81(2).

[17] Duparchy, A., Guillozet, J., De Colombel, T., Bornard, L., "Spatial harmonic decomposition as a tool for unsteady flow phenomena analysis," IOP Conference Series: Earth and Environmental Science.

[18] Trivedi, C., Cervantes, M. J., Gandhi, B. K., Dahlhaug, O. G., 2014, "Pressure Measurements on a High Head Francis Turbine During Load Acceptance and Rejection," Journal of Hydraulic Research, 52(2), pp. 283-297.

[19] Goyal, R., Cervantes, M. J., Gandhi, B. K., 2017, "Characteristics of Synchronous and Asynchronous modes of fluctuations in Francis turbine draft tube during load variation," International Journal of Fluid Machinery and Systems, 10(2).

[20] Dörfler, P., 1982, "System dynamics of the Francis turbine half load surge," 11th IAHR Symposium on Operating Problem of Pump Stations and PowerplantsAmsterdam, Netherlands.

[21] Fritsch, A., Maria, D., 1988, "Dynamic behaviour of a partial load Francis water turbine: model/prototype comparison," La Houille Blanche 3.

[22] Favrel, A., Landry, C., Müller, A., Yamamoto, K., Avellan, F., "Hydro-acoustic resonance behaviour in presence of a precessing vortex rope: Observation of a lock-in phenomenon at part-load Francis turbine operation," Proc. IOP Conference Series: Earth and Environmental Science.

[23] Favrel, A., Müller, A., Landry, C., Yamamoto, K., Avellan, F., 2016, "LDV survey of cavitation and resonance effect on the precessing vortex rope dynamics in the draft tube of Francis turbines," Experiments in Fluids, 57(168).

[24] Favrel, A., Gomes Pereira, J. J., Landry, C., Alligné, S., Andolfatto, L., Nicolet, C., Avellan, F., 2019, "Prediction of hydro-acoustic resonances in hydropower plants by a new approach based on the concept of swirl number," Journal of Hydraulic Research, 58(1), pp. 87-104.

[25] Magnoli, M. V., Maiwald, M., 2014, "Influence of Hydraulic Design on Stability and on Pressure Pulsations in Francis Turbines at Overload, Part Load and Deep Part Load based on

Numerical Simulations and Experimental Model Test Results," 27th IAHR Symposium on Hydraulic Machinery and Systems.

[26] Favrel, A., Gomes Pereira Junior, J., Landry, C., Müller, A., Nicolet, C., Avellan, F., 2018, "New insight in Francis turbine cavitation vortex rope: role of the runner outlet flow swirl number," Journal of Hydraulic Research, 56(3).

[27] Avellan, F., "Introduction to cavitation in hydraulic machinery," Proc. Proceedings of the 6th international conference on hydraulic machinery and hydrodynamics.

[28] Valentin, D., Presas, A., Equsquiza, E., Valero, C., Equsquiza, M., Bossio, M., 2017, "Power Swing Generated in Francis Turbines by Part Load and Overload Instabilities," Energies 10(12).

[29] Farhat, M., Natal, S., Avellan, F., Paquet, F., Couston, M., "Onboard Measurements of Pressure and Strain Fluctuations in a Model of Low Head Francis Turbine - Part 1: Instruction," Proc. 21th IAHR Symposium on Hydraulic Machinery and Systems.

[30] Wack, J., Riedelbauch, S., "Numerical simulations of the cavitation phenomena in a Francis turbine at deep part load conditions," Proc. 9th International Symposium on Cavitation, Journal of Physics: Conference Series

[31] Conrad, P., Weber, W., Jung, A., "Deep Part Load Flow Analysis in a Francis Model turbine by means of two-phase unsteady flow simulations," Proc. Hyperbole, IOP Conf. Series: Journal of Physics: Conf. Series.

[32] Yamamoto, K., 2017, "Hydrodynamics of Francis turbine operation at deep part load condition," PhD, EPFL.

[33] Yamamoto, K., Müller, A., Favrel, A., Avellan, F., 2017, "Experimental evidence of inter-blade cavitation vortex development in Francis turbines at deep part load condition," Experiments in Fluids, 58(142).

[34] Yamamoto, K., Müller, A., Favrel, A., Avellan, F., 2019, "Physical Mechanism of Interblade Vortex Development at Deep Part Load Operation of a Francis Turbine," J. Fluids Engineering, 141(2).

[35] Escudier, M. P., Keller, J. J., , 1983, "Vortex breakdown: a two-stage transition," AGARD CP no. 342: aerodynamics of vortical type flows in three dimesions, 25.

[36] Escudier, M. P., 1984, "Observation of the flow produced in a cylindrical container by a rotating endwall," Experiments in Fluids, 2, pp. 189-196.

[37] Shtern, V., 2018, "5 - Swirl Decay Mechanism," Cellular Flows: Topological Metamorphoses in Fluid Mechanics, Cambridge University Press, pp. 244-318.

[38] Shtern, V., Torregrosa, M., Herrada, A., 2012, "Effect of swirl decay on vortex breakdown in a confined steady axisymmetric flow," Physics of Fluids, 24(043601).

[39] Shtern, V., Naumov, I., 2021, "Swirl-decay mechanism generating counterflows and dells in vortex motion," Journal of Engineering Thermophysics, 30(1), pp. 19-39.

[40] Lucca-Negro, O., O'Doherty, T., 2001, "Vortex breakdown: a review," Progress in Energy and Combustion Science, 27, pp. 431-481.

[41] Litvinov, I., Shtork, S., Gorelikov, E., Mitryakov, A., Hanjalic, K., 2018, "Unsteady regimes and pressure pulsations in draft tube of a model hydro turbine in a range of off-design conditions," Experimental Thermal and Fluid Science, 91, pp. 410-422.

[42] Stefan, D., Rudolf, P., Muntean, S., Susan-Resiga, R., 2013, "Structure of flow fields downstream of two different swirl generators," Engineering Mechanics, 20(5), pp. 339-353.

[43] Stefan, D., 2015, "Study of the dissipation in spiraling vortical structures," PhD, Brno University of Technology.

[44] Muntean, S., Tănasă, C., Bosioc, A. I., Moş, D. C., "Investigation of the Plunging Pressure Pulsation in a Swirling Flow with Precessing Vortex Rope in a Straight Diffuser," Proc. 28th IAHR symposium on Hydraulic Machinery and Systems (IAHR2016), IOP Conf. Series: Earth and Environmental Science.

[45] Stuparu, A., Susan-Resiga, R., 2016, "The Complex Dynamics of the Precessing Vortex Rope in a Straight Diffuser," IOP Conf. Series: Earth and Environmental Science, 49(082013).

[46] Foroutan, H., Yavuzkurt, S., 2014, "A partially-averaged Navier–Stokes model for the simulation of turbulent swirling flow with vortex breakdown," International Journal of Heat and Fluid Flow, 50, pp. 402-416.

[47] Javadi, A., Bosioc, A., Nilsson, H., Muntean, S., Susan-Resiga, R., 2016, "Experimental and Numerical Investigation of the Precessing Helical Vortex in a Conical Diffuser, With Rotor–Stator Interaction," Journal of Fluids Engineering, ASME, 138.

[48] Javadi, A., Nilsson, H., 2017, "Active flow control of the vortex rope and pressure pulsations in a swirl generator," Engineering Application of Computational Fluids Mechanics, 11(1), pp. 30-41.

[49] Ji, B., Wang, J., Luo, X., Miyagawa, K., Xiao, L. Z., Long, X., Tsujimoto, Y., 2016, "Numerical simulation of cavitation surge and vortical flows in a diffuser with swirling flow," Journal of Mechanical Science and Technology, 30(6).

[50] Stuparu, A., Susan-Resiga, R., "The origin of the plunging pressure fluctuation for a swirling flow with precessing vortex rope in a straight diffuser," Proc. 6th IAHR International Meeting of the Workgroup on Cavitation and Dynamic Problems in Hydraulic Machinery and Systems.

[51] Landry, C., Favrel, A., Müller, A., Nicolet, C., Avellan, F., 2016, "Local wave speed and bulk flow viscosity in Francis turbines at part load operation," Journal of Hydraulic Research, 54(2), pp. 185-196.

[52] Nishi, M., Kubota, T., Matsunaga, S., Senoo, Y., 1980, "Study on swirl flow and surge in an elbow tyoe draft-tube," IAHR SymposiumTokyo, Japan.

[53] Tsujimoto, Y., Yoshida, Y., Maekawa, Y., Watanabe, S., Hashimoto, T., 1997, "Observations of oscillating cavitation of an inducer," Journal of Fluids Engineering, ASME, 119.

[54] Chen, C., Nicolet, C., Yonezawa, K., Farhat, M., Avellan, F., Tsujimoto, Y., 2008, "One-dimensional analysis of full load draft-tube surge," Journal of Fluids Engineering, ASME, 130.

[55] Brennen, C. E., Acosta, A. J., 1973, "Theoretical, quasi-static analysis of cavitation compliance in turbopumps," Journal Spacecraft and Rockets, 10(3).

[56] Brennen, C., Acosta, A. J., 1976, "The dynamic transfer function for a cavitating inducer," Journal of Fluids Engineering, ASME, 98.

[57] Dörfler, P., 1982, "System dynamics of the Francis turbine half load surge " Proceedings of the 11th IAHR Symposium on Operating Problem of Pump Stations and PowerplantsNetherlands.

[58] Couston, M., Philibert, R., 1998, "Partial load modelling of gaseous francis turbine rope," The international journal on Hydropower and Dams, 1, pp. 525-533.

[59] Philibert, R., and Couston, M., "Francis Turbine at Part Load: Matrix Simulating the Gaseous Rope," Proc. Proceedings of the 19th IAHR Symposium on Hydraulic Machinery and Systems.

[60] Koutnik, J., Pulpitel, L., 1996, "Modeling of the francis turbine full-load surge modeling," Testing and Monitoring for Hydro Power Plants.

[61] Tsujimoto, Y., Kamijo, K., Yoshida, Y., 1993, "A theoretical analysis of rotating cavitation in inducers," Journal of Fluids Engineering, ASME, 115.

[62] Ciocan, G. D., Iliescu, M. S., Vu, T. C., Nennemann, B., Avellan, F., 2007, "Experimental Study and Numerical Simulation of the FLINDT Draft Tube Rotating Vortex," J. Fluids Engineering, 129.

[63] Khozaei, M. H., Favrel, A., Masuko, T., Yamaguchi, N., Miyagawa, K., 2021, "Generation of Twin Vortex Rope in the Draft-Tube Elbow of a Francis Turbine During Deep Part-Load Operation," J. Fluids Engineering, 143(10): 101206.

[64] Pasche, S., Gallaire, F., Avellan, F., 2019, "Origin of the synchronous pressure fluctuations in the draft tube of Francis turbines operating at part load conditions," Journal of Fluids and Structures, 86, pp. 13-33.

[65] Gupta, A. K., Lilley, D. G., Syred, N., 1984, Swirl Flows Tunbridge Wells, Kent : Abacus Press.

[66] Dörfler, P., Sick, M., Coutu, A., 2013, Flow-Induced Pulsation and Vibration in Hydroelectric Machinery, Springer.

[67] Jacob, T., 1993, "Evaluation sur modèle réduit et prédiction de la stabilité de fonctionnement des turbines Francis," PhD, EPFL.

[68] Jacob, T., Prenat, J-E., 1996, "Francis turbine surge: Discussion and data base," 18th Symposium on Hydraulic Machinery and Systems (IAHR)Valencia, Spain, pp. 855-864.

[69] Khozaei, M. H., Favrel, A., Masuko, T., Yamaguchi, N., Miyagawa, K., 2021, "Numerical and experimental analysis of pressure fluctuations in the draft-tube of a Francis turbine using the swirl number," The 30th symposium on Hydraulic Machinery and Systems (IAHR2020), IOP conference series Earth and Environmental Science, Online conference.

[70] Nishi, M., Okamoto, M., Wang, X., 1993, "Evaluation of pressure fluctuations caused by cavitated spiral vortex core in the swirling flow of elbow draft-tube," Work group on: the behavior of hydraulic machinery under steady oscillatory conditions, 6th international IAHR meetingLausanne, Switzerland.

[71] Chen, C., Nicolet, C., Yonezawa, K., Farhat, M., Avellan, F., Miyagawa, K., Tsujimoto, Y., 2010, "Experimental Study and Numerical Simulation of Cavity Oscillation in a Diffuser with Swirling Flow," International Journal of Fluid Machinery and Systems, 3(1).

[72] Speziale, C. G., Sarkar, S., Gatski, T. B., 1991, "Modeling the Pressure-Strain Correlation of Turbulence: an Invariant Dynamical Systems Approach," Journal of Fluid Mechanics, 277, pp. 245-272.

[73] Fokeer, S., Lowndes, I. S., Hargreaves, D. M., 2010, "Numerical modelling of swirl flow induced by a three-lobed helical pipe," Chemical Engineering and Processing: Process Intensification, 49, pp. 536-546.

[74] Jochmann, P., Sinigersky, A., Hehle, M., Schafer, O., Koch, R., Bauer, H. -J., 2006, "Numerical simulation of a precessing vortex breakdown," International Journal of Heat and Fluid Flow, 27, pp. 192-203.

[75] Zhang, Y., Vanierschot, M., 2021, "Modeling capabilities of unsteady RANS for the simulation of turbulent swirling flow in an annular bluff-body combustor geometry," Applied Mathematical Modelling, 89, pp. 1140-1154.

[76] Ramirez, J., Cortes, C., 2010, "Comparison of different URANS schemes for the simulation of complex swirling flows," Numerical Heat Transfer, Part B, 58, pp. 98-120.

[77] Rukes, L., Paschereit, C. O., Oberleithner, K., 2016, "An assessment of turbulence models for linear hydrodynamic stability analysis of strongly swirling jets," European Journal of Mechanics B/Fluids, 59, pp. 205-218.

[78] Wegner, B., Maltsev, A., Schneider, C., Sadiki, A., Dreizler, A., Janicka, J., 2004, "Assessment of unsteady RANS in predicting swirl flow instability based on LES and experiments," International Journal of Heat and Fluid Flow, 25, pp. 528-536.

[79] Muntean, S., Ruprecht, A., Susan-Resiga, R., 2005, "A numerical investigation of the 3d swirling flow in a pipe with constant diameter. Part 1: Inviscid computation," Workshop on Vortex Dominated Flows - Achievements and Open ProblemsTimisoara, Romania, pp. 77-86.

[80] Muntean, S., Buntic, I., Ruprecht, A., Susan-resiga, R., 2005, "A numerical investigation of the 3d swirling flow in a pipe with constant diameter. Part 2: Turbulent computation," Workshop on Vortex Dominated Flows - Achievements and Open ProblemsTimisoara, Romania, pp. 87-96.

[81] Sarpkaya, T., 1971, "On stationary and travelling vortex breakdowns," Journal of Fluid Mechanics, 45(3), pp. 545-559.

[82] Squire, H. B., 1960, "Analysis of the vortex breakdown phenomenon, Part 1," Imperial College of Science and Technology Aeronautics.

[83] Benjamin, T. B., 1962, "Theory of the vortex breakdown phenomenon," Journal of Fluid Mechanics, 14, pp. 593-629.

[84] Gartshore, I. S., 1962, "Recent work in swirling incompressible flow. N.R.C. (Canada)," Aero. Rep. LR-343.

[85] Shi, X., Shan, X., 1987, "Relation between the quasi-cylindrical approximation and the critical classification for swirling flow," Acta Mechanica Sinica, 3, pp. 304-314.

[86] Jeong, J., Hussain, F., 1995, "On the identification of a vortex," Journal of Fluid Mechanics, 285, pp. 69-94.

[87] Dong, Y., Yan, Y., Liu, C., 2016, "New visualization method for vortex structure in turbulence by lambda2 and vortex filaments," Applied Mathematical Modelling, 40, pp. 500-509.

[88] Jiang, M., Machiraju, R., Thompson, D., 2005, "14 - Detection and Visualization of Vortices," Visualization Handbook, C. D. Hansen, Johnson, C. R., ed., Butterworth-Heinemann, pp. 295-309.

[89] Gelfgat, A. Y., Bar-Yoseph, P. Z., Solan, A., 1996, "Stability of confined swirling flow with and without vortex breakdown," Journal of Fluid Mechanics, 311, pp. 1-36.

[90] Pasche, S., Avellan, F., Gallaire, F., 2017, "Part load vortex rope as a global unstable mode," Journal of Fluids Engineering, ASME, 139.

[91] Pasche, S., Gallaire, F., Avellan, F., 2018, "Predictive control of spiral vortex breakdown," Journal of Fluid Mechanics, 842, pp. 58-86.

[92] Pasche, S., Avellan, F., Gallaire, F., 2019, "Optimal control of part load vortex rope in Francis turbines," Journal of Fluids Engineering, ASME, 141.

[93] Graftieaux, L., Michard, M., Grosjean, N., 2001, "Combining PIV, POD and vortex identification algorithms for the study of unsteady turbulent swirling flows," Measurement Science and Technology, 12.

[94] Burr, K. P., 2005, "Marine Hydrodynamics," MIT lectures.

[95] Wu, J.-Z., Ma, H. -Y., Zhou, M. -D., 2006, Vorticity and Vortex Dynamics, Springer Berlin Heidelberg, Germany.

[96] Tian, S., Gao, Y., Dong, X., Liu, C., 2018, "Definitions of vortex vector and vortex," Journal of Fluid Mechanics, 849, pp. 312-339.

[97] Nishi, M., Matsunaga, S., Kubota, T., Senoo, Y., 1982, "Flow Regimes in an Elbow-Type Draft Tube," 11th Symposium on Hydraulic Machinery and Systems (IAHR)Amsterdam, Netherlands, pp. 1-13.

[98] Nishi, M., Matsunaga, S., Okamoto, M., Uno, M., Nishitani, K., 1988, "Measurement of three-dimensional periodic flow on a conical draft tube at surging condition," Winter Annual Meeting of the American Society of Mechanical Engineers, FED (Series), Chicago, Illinois, pp. 81-88.

[99] Brennen, C. E., 1995, Cavitation and bubble dynamics, Oxford University Press, Oxford, UK.

[100] Yanagida, H., 2008, "The effect of dissolve gas concentration in the initial growth stage of multi cavitation bubbles Differences between vacuum degassing and ultrasound degassing," Ultrasonics Sonochemistry, 15.

[101] Kikuta, K., Yoshida, Y., Watanabe, M., Hashimoto, T., Nagaura, K., Ohira, K., 2008, "Thermodynamic effect on cavitation performances and cavitation instabilities in an inducer," Journal of Fluids Engineering, ASME, 130.

[102] Watanabe, S., Enomoto, K., Yamamoto, Y., Hara, Y., 2014, "Thermal and Dissolved Gas Effects on Cavitation in a 2-D Convergent-Divergent Nozzle Flow," ASME 2014 4th Joint US-European Fluids Engineering Division Summer Meeting, Journal of Fluids Engineering, ASME, Chicago, Illinois, USA.

[103] Kobayashi, K., Katayama, Y., Watanabe, S., Tsuda, S., 2021, "Experimental investigation on cavity pressure inside sheet cavitation," Journal of fluids engineering, ASME, 143.

[104] Brennen, C. E., "The unsteady, dynamic characterization of hydraulic systems with emphasis on cavitation and turbomachines," Proc. Joint Symposium on design and operation of fluid machinery, ASME/ASCE/IAHR.

[105] Dörfler, P. K., 2017, "Cavitation Compliance in 1D Part-load Vortex Models," International Journal of Fluid Machinery and Systems, 10(3).

[106] Ng, S., Brennen, C., 1978, "Experiments on the Dynamic Behavior of Cavitating Pumps," Journal of Fluids Engineering, ASME, 100(2).

[107] Brennen, C. E., Meissner, C., Lo, E., Hoffman, G., 1982, "Scale Effects in the Dynamic Transfer Functions for Cavitating Inducers," Journal of Fluids Engineering, ASME, 104(4).

[108] Jacob, T., and Prenat, J., "Identification of a Hydraulic Turbomachine's Hydro-Acoustic Transmission Parameters," Proc. Proceedings of the IAHR Fifth International Meeting of Work Group on the Behaviour of Hydraulic Machinery Under Steady Oscillatory Conditions.

[109] Otsuka, S., Tsujimoto, Y., Kamijo, K., Furuya, O., 1996, "Frequency Dependence of Mass Flow Gain Factor and Cavitation Compliance of Cavitating Inducers," Journal of Fluids Engineering, ASME, 118.

[110] Rubin, S., 2004, "An Interpretation of Transfer Function Data for a Cavitating Pump," AIAA/ASME/SAE/ASEE joint propulsion conference and exhibitfort lauderdale, Florida, USA.

[111] Yonezawa, K., Aono, J., Kang, D., Horiguchi, H., Kawata, Y., and Tsujimoto, Y., 2012, "Numerical Evaluation of Dynamic Transfer Matrix and Unsteady Cavitation Characteristics of an Inducer," International Journal of Fluid Machinery and Systems, 5(3).

[112] Ashida, T., Yamamoto, K., Yonezawa, K., Horiguchi, H., Kawata, Y., Tsujimoto, Y., 2017, "Measurement of Dynamic Characteristics of an Inducer in Cavitating Conditions," International Journal of Fluid Machinery and Systems, 10(3).

[113] Nicolet, C., 2007, "Hydroacoustic modelling and numerical simulation of unsteady operation of hydroelectric systems," PhD, EPFL.

[114] Alligne, S., 2011, "Forced and Self Oscillations of Hydraulic Systems Induced by Cavitation Vortex Rope of Francis Turbines," PhD, EPFL.

[115] Landry, C., 2015, "Hydroacoustic Modeling of a Cavitation Vortex Rope for a Francis Turbine," PhD, EPFL.

[116] Gomez, L., Mohan. R., Shoham O., 2004, "Swirling Gas–Liquid Two-Phase Flow—Experiment and Modeling Part I: Swirling Flow Field," J. Fluids Engineering, 126.

[117] Khozaei, M. H., Yamaguchi, N., Miyagawa, K., 2019, "Numerical analysis of hydraulic loss in a medium specific-speed Francis turbine," The 2nd IAHR-Asia Symposium on Hydraulic Machinery and SystemsBusan, South Korea.

[118] IEC, 1999, "IEC 60193: Hydraulic turbines, storage pumps and pump-turbines – model acceptance tests,"Geneva: Intrenational Commision.

[119] Cassidy, J. J., Falvey, H. T., 1970, "Observations of unsteady flow arising after vortex breakdown " Journal of Fluid Mechanics 41(4).

[120] Cala, C. E., Fernandes, E. C., Heitor, M. V., Shtork, S. I., 2006, "Coherent structures in unsteady swirling jet flow " Experiments in Fluids 40(2).

[121] Thakare, H. R., Monde, A., Parekh, A. D., 2015, "Experimental, computational and optimization studies of temperature separation and flow physics of vortex tube: A review," Renewable and Sustainable Energy Reviews, 52, pp. 1043-1071.

[122] Mitrofanova, O. V., Podzorov, G. D., Pozdeeva, I. G., 2013, "Vortex structure of swirl flows," International Journal of Heat and Mass Transfer, 65, pp. 225-234.

[123] Menter, F., 1996, "A comparison of some recent eddy-viscosity turbulence models. Journal of fluids engineering," J. Fluids Engineering, 118.

[124] Menter, F., Kuntz, M., Langtry, R., 2003, "Ten years of industrial experience with the SST turbulence model," Turbulence, heat and mass transfer, 4.

[125] Stoica, P., Moses, R., 2005, Spectral Analysis of Signals Upper Saddle River, N.J. : Pearson/Prentice Hall.

[126] Menter, F., Kuntz, M., Bender, R., "A Scale-Adaptive Simulation Model for Turbulent Flow Predictions," Proc. 41st Aerospace Sciences Meeting and Exhibit, American Institute of Aeronautics and Astronautics.

[127] Menter, F., Egorov, Y., "A Scale Adaptive Simulation Model using Two-Equation Models," Proc. 43rd AIAA Aerospace Sciences Meeting and Exhibit, American Institute of Aeronautics and Astronautics.

[128] Minakov, A. V., Platonov, D. V., Dekterev, A. A., 2015, "The numerical simulation of low frequency pressure pulsations in the high-head Francis turbine," Computers and Fluids, 111.

[129] Jost, D., Skerlavaj, A., Morgut, M., Meznar, P., Nobile, E., 2015, "Numerical simulation of flow in a high head Francis turbine with prediction of efficiency, rotor stator interaction and vortex structures in the draft tube," Journal of Physics: Conference Series, 579(1).

[130] Goyal, R., Trivedi, C., Gandhi, B. K., Cervantes, M. J., 2017, "Numerical Simulation and Validation of a High Head Model Francis Turbine at Part Load Operating Condition," Journal of The Institution of Engineers (India): Series C, 99, pp. 557–570.

[131] Buntic Ogor, I., Dietze, S., Ruprecht, A., "Numerical Simulation of the Flow in Turbine-99 Draft Tube," Proc. Third IAHR/ERCOFTAC workshop on draft tube flow.

[132] Wu, J., Shimmei, K., Tani, K., Niikura, K., Sato, J., 2007, "CFD-Based Design Optimization for Hydro Turbines," J. Fluids Engineering, 129.

[133] Wallimann, H., Neubauer, R., "Numerical Study of a High Head Francis Turbine with Measurements from the Francis-99 Project," Proc. Francis-99 Workshop 1: steady operation of Francis turbines, IOP Publishing, Journal of Physics.

[134] Mossinger, P., Jester-Zurker, R., Jung, A., "Investigation of different simulation approaches on a high-head Francis turbine and comparison with model test data: Francis-99," Proc. Francis-99 Workshop 1: steady operation of Francis turbines IOP Publishing, Journal of Physics.
[135] Bucker, I., Karhoff, D.-C., Klass, M., Schroder, W., 2012, "Stereoscopic multi-planar PIV measurements of in-cylinder tumbling flow," Experiments in Fluids, 53, pp. 1993-2009.
[136] Gomes Pereira Jr., J., Favrel, A., Andolfatto, L., Landry, C., Alligné, S., Nicolet, N., Avellan, F., 2019, "Procedure for predicting part load resonance in Francis turbine hydropower units based on swirl number and local cavitation coefficient similitude," Mechanical Systems and Signal Processing, 132, pp. 84-101.

Research achievements

Journal papers

* **M. H. Khozaei**, A. Favrel, K. Miyagawa, "On the generation mechanisms of low-frequency synchronous pressure pulsations in a simplified draft-tube cone", accepted for publication in the International Journal of Heat and Fluid Flow, Elsevier.
* **M. H. Khozaei**, A. Favrel, T. Masuko, N. Yamaguchi, K. Miyagawa, "Generation of twin vortex rope in the draft-tube elbow of a Francis turbine during deep part-load operation", ASME Journal of Fluids Engineering, May 2021, paper No. FE-21-1022.
* **M. H. Khozaei**, A. Favrel, T. Masuko, N. Yamaguchi, K. Miyagawa, "Numerical and experimental analysis of pressure fluctuations in the draft-tube of a Francis turbine using the swirl number", IOP Conference Series Earth and Environmental Science, 774(1):012088, proceeding of the 30th Symposium on Hydraulic Machinery and Systems (IAHR2020), March 2021.
* R. Watanabe, K. Miyagawa, **M. H. Khozaei**, N. Yamaguchi, T. Masuko, "Optimization procedure to design a Francis turbine runner using 2D Through-flow analysis", Journal of Physics Conference Series, 1909(1):012031, proceeding of the 18th International Symposium on Transport Phenomena and Dynamics of Rotating Machinery, November 2020.
* **M. H. Khozaei**, S. A. Nourbakhsh, "Analytical study of fluid flow in propeller-type current-meter", International Journal of Fluid Machinery and Systems, July 2019, Vol. 13, No. 2.
* **M. H. Khozaei**, S. A. Nourbakhsh, "Influence of the geometrical parameters of propeller-type current-meter on its performance," International Journal of Mechanical and Production Engineering, vol. 4-2, Feb. 2016.
* M. Rahnama, M. Ameri, R. Panahi, **M. H. Khozaei**, M. H. Saffaripour, "Investigation of thermal performance integrated collector-storage solar water heater with different reflectors", AJSR-ME, vol. 45-1, 2013.

Conference papers

* A. Favrel, Z. Liu, **M. H. Khozaei**, T. Irie, K. Miyagawa, "Transition of a cavitation vortex rope from cylindrical to elliptical mode in Francis turbine draft tube", 11th International Symposium on Cavitation (CAV2021), May 2021.
* **M. H. Khozaei**, N. Yamaguchi, K. Miyagawa, "Numerical analysis of hydraulic loss in a medium specific-speed Francis turbine", Proceeding of the 2nd IAHR-Asia Symposium oh Hydraulic Machinery and Systems, 24th-25th September 2019, Busan, Korea.
* **M. H. Khozaei**, S. A. Nourbakhsh, "Influence of the geometrical parameters of propeller-type current-meter on its performance", 50th IIER International Conference, Zurich, Switzerland, 26th Dec. 2015.
* **M. H. Khozaei**, A. Zade kafi, "Design and numerical study of Kaplan turbine: Parametric study", 23rd ISME2015, Amirkabir University of Technology, Tehran, Iran, 12-14th May 2015.
* H. Kasraei, **M. H. Khozaei**, M. Salmanzadeh, "Experimental study of solar floor heating system in Kerman with 24-hour application case", 1st International conference and exhibition on solar energy, Tehran, Iran, 19-20th, May 2014.

Scholarships

* Granted for Japanese Government Monbukagakusho (MEXT) scholarship for PhD studies, since Sept. 2018.

Awards

* Selected for "Best Paper Award", 2nd IAHR-Asia Symposium on Hydraulic Machinery and Systems, 2019, Busan, Korea.
* Graduated with 1st top GPA in cohort of 2013 (M.Sc.), University of Tehran.
* Selected for "Best Oral Presentation", 50th IIER International Conference, Zurich, Switzerland, Dec. 2015.